UNIVERSITY OF CALIFORNIA
SANTA CRUZ

MAXIMIZING STRONG MAGNON-PHONON COUPLING IN SINGLE NANOMAGNETS

A dissertation submitted in partial satisfaction
of the requirements for the degree of

DOCTOR OF PHILOSOPHY

In

Electrical and Computer Engineering

by

Sujung Kim

September 2024

The Dissertation of Sujung Kim
is approved by:

_____
Professor Holger Schmidt, chair

_____
Professor Nobuhiko Kobayashi

_____
Professor Marco Rolandi

_____
Peter F. Biehl
Vice Provost and Dean of Graduate Studies

Table of Contents

1. Introduction 1

2. Magnetization Dynamics

2.1. Introduction 4

2.2. Microscopic Magnetization Dynamics 7

2.2.1. Magnetic Dipoles 8

2.2.2. Larmor Precession 16

2.3. Competing Energies 17

2.3.1. Zeeman Energy 19

2.3.2. Exchange Energy 19

2.3.3. Crystal Anisotropy Energy (Magnetocrystalline Anisotropy Energy) 23

2.3.4. Uniaxial Anisotropy Energy 25

2.3.5. Shape Anisotropy Energy (Demagnetization Energy) 26

2.4. Macroscopic Magnetization Dynamics 28

3. Detection Methods

3.1. FMR Technique 39

3.2. Optical Methods 43

3.2.1. Weiss Mean Field Theory (Molecular Field Theory) and Laser Pulses 44

3.2.2. Magnetization Dynamics upon Femtosecond Laser Pulse Excitation 46

3.2.3. Magneto-Optic Kerr Effect (MOKE) 48

3.2.4. Detection Mechanism with Balanced Photodetector (BPD) 53

3.3. Time-Resolve MOKE Setup for Simultaneous Detection of Magnon and Phonon Dynamics 54

4. Magnetoelastics in Nanomagnets

4.1. Magnetoelastic Effect (Villari effect) and Magnetostrictive Materials.....60

4.1.1. Magnetostriction and Magnetoelastic Effect (Villari Effect).....60

4.1.2. Magnetostrictive Materials – Building Blocks for Magnetoelastic Coupling.....64

4.1.2.1. 3d Transition Metals 65

4.1.2.2. Terfenol-D Alloy ($Tb_{0.3}Dy_{0.7}Fe_2$) 65

4.1.2.3. Co-Fe Alloys 67

4.1.2.4. Galfenol Alloys (Fe-Ga) 68

4.2. Surface-Acoustic Wave (SAW)-Driven Magnetoelastic Coupling 68

4.2.1. Theoretical Overview of Magnetoelastically Coupled Dynamics 70

4.2.2. Electrically Excited Magnetoelastic Coupling.....78

4.2.3. All-Optical Thermally Excited Magnetoelastic Coupling 83

4.2.4. Controlling the Magnetoelastic Coupling.....87

4.2.4.1. Control via Dielectric Coating Layer.....88

4.2.4.2. Control via Random Array.....91

4.2.5. Magnetoelastic Coupling as a Measure of Intrinsic Damping.....93

4.3. Strong Magnon-Phonon Coupling 100

4.3.1. Phononic Dynamics in the Absence of Magnon-Phonon Coupling.....102

4.3.2. Coupled Magnon-Phonon Dynamics via Magnetoelastic Coupling....104

4.3.3. Controlling Strong coupling: Geometric perspective 108

5. Hybrid Magnon-Phonon Dynamics in a Poly-crystalline CoFe Nanomagnet

5.1. Introduction.....109

5.2. Coupled Dynamics in a Single Nanomagnet 109

5.3. Materials Engineering Perspective (Ni vs. CoFe).....114

6. Magnetization Dynamics in Single-crystalline CoFe and CoFe/CMS Thin Film

6.1. Introduction.....118

6.2. Sample Preparation and X-ray Characterization.....122

6.3. Results and Discussion 128

6.4. Conclusion 141

7. Hybrid Magnon-Phonon Dynamics in a Single-crystalline CoFe Nanomagnet

7.1. Introduction.....143

7.2. Fabrication Methods 145

7.2.1 Corner Shaping for Square Nanomagnets.....149

7.2.2 Wet Etching Test 151

7.2.3. Challenges and Improvements on Fabrication to Note.....154

7.2.4. Fabrication Process for s-CoFe NM 156

7.2.5. Validation of Compatibility of Fabrication Process for s-CoFe NM ...157

7.3. Coupled Dynamics in a Single Nanomagnet 159

8. Outlook and Future Works 166

Bibliography 170

List of Figures

Figure 2.1. Magnetic dipoles placed inside a uniform magnetic field. 9

Figure 2.2. Illustration showing the L-S coupling in hydrogen atom. The argument in the main text views in electron's perspective. 10

Figure 2.3. Two contributions to the magnetic moment, (a) orbital magnetic moment and (b) spin magnetic moment.....12

Figure 2.4. Schematics showing exchange energy between two neighboring spins, i and j. 20

Figure 2.5. Magnetocrystalline energy for (a) BCC crystal and (b) FCC crystal. $G_{Crystal,i}$, $(i = x, y, z)$ represents the normalized energy calculated from equation (2.34) or equation (2.35). Action of having $K_1 > 0$ ($K_1 < 0$) for BCC (FCC) crystal increases (lowers) the total energy, providing lower energy for the magnetization to preferably align along the magnetic easy-axis in <100> (<111>) direction. K_2 was ignored in this calculation as $K_1 \gg K_2$. 23

Figure 2.6. Schematics of spin wave traveling across the wavelength of spin wave, λ, for (a) the finite spin wavelength ($\vec{\boldsymbol{k}}_{\boldsymbol{SW}} \neq 0$) and (b) the infinitely long spin wavelength ($\vec{\boldsymbol{k}}_{\boldsymbol{SW}} = 0$). The top row shows m_y over the spin wavelength, the middle row shows m

in $x - y$ plane, and the bottom row shows magnetization rotation as spin wave propagate over the length of λ. 29

Figure 2.7. Schematics of coordinate transfer from the Cartesian (x, y, z) system to $(1, 2, 3)$ coordinate system.....31

Figure 3.1. Schematics of SAW-driven FMR measurement showing the coordinate system. SAWs interact with a Ni thin film located between the two IDTs as they travel along the $LiNbO_3$ piezoelectric film. SAWs are detected at the IDT on the opposite side of the device. The magnetization of the Ni film is denoted as $\boldsymbol{M}$, and the externally applied magnetic field is denoted as $\boldsymbol{H}$. The figure on the right shows the strain applied to the Ni thin film due to interaction with SAWs. [30].....39

Figure 3.2. (a) Transmission spectra $|S_{21}|$ of higher harmonics of SAW frequencies. (b) Reflection spectra at $H_{app} = 1\ kOe$ at $\alpha = 60°$. [61] 41

Figure 3.3. (a) Normalized transmission spectra ($|S_{21}|_{norm}{}^2$) and (b) their signal phase spectra ($arg(|S_{21}|^2)$) at various magnetic field (H_{app}) and in-plane orientation α of applied external magnetic field – see the system in figure 3.1 [30]. 42

Figure 3.4. Spontaneous magnetization response at different temperatures. (a) Spontaneous magnetization over the maximum magnetization calculated using the Weiss mean field introduced in equation (3.6). The circles corresponds to the 3 different temperatures at $T = 0,\ 0 \ll T < T_C$, and $T_C < T$. (b) Schematics of spontaneous magnetization response upon introduction of heat in the ferromagnetic system. As the

temperature increases, randomization in the spin orientation is introduced, leading to a lower magnetization in the system. At the critical temperature, the magnetization vanishes as more random orientation of spin is introduced, which averages out to zero magnetization. The blue arrows are the net spontaneous magnetization in the ferromagnet, and the pink arrows are the spins at each electron cites. 45

Figure 3.5. Schematics of magnetization dynamics upon excitation of femtosecond laser pulses. (a) Magnetization before the application of external magnetic field, $\overrightarrow{\boldsymbol{H}}_{\boldsymbol{app}}$. The magnetization direction lies along the magnetic easy-axis, which is in the in-plane direction for an arbitrary poly-crystalline thin film in this example. (b) Magnetization points along the $\overrightarrow{\boldsymbol{H}}_{\boldsymbol{eff}}$ with the presence of $\overrightarrow{\boldsymbol{H}}_{\boldsymbol{app}}$ before the irradiation of laser pulses. (c) Upon excitation of laser pulses, the heat is introduced in the spin system resulting in the reduced magnetization. Consequently, the magnetization precess about the new effective magnetic field $\overrightarrow{\boldsymbol{H}}'_{\boldsymbol{eff}}$. (d) After the spin system cools down, the magnetization recovers its original states, thus the effective magnetic field points at the initial orientation as shown in (b). $\overrightarrow{\boldsymbol{H}}_{\boldsymbol{eff}}$ acts as a torque to the magnetization, resulting in the precession about the axis of $\overrightarrow{\boldsymbol{H}}_{\boldsymbol{eff}}$. 46

Figure 3.6. Schematics of (a) Polar, (b) longitudinal, and (c) transverse MOKE configurations. 50

Figure 3.7. Schematics showing the magneto-optic Kerr effect upon reflection on the magnetic specimen, demonstrating the Kerr rotation and Kerr ellipticity. 51

Figure 3.8. Schematics of TR-MOKE setup with BPD configuration.[32] The pump beam path is highlighted with blue line and the probe beam path is highlighted with red line. See main text for detail. BS: beam splitter, SHG: second-harmonic generator, MCW: mechanical chopper wheel, DF: dichroic filter, DS: delay stage, L(α_P): linear polarizer, WM: WiTec microscope, PM: permanent magnets, CF: color filter, PBS: polarized beam splitter, BPD: balanced photodetector. 55

Figure 3.9. Time-dependent Kerr rotation of z-component of magnetization of a Ni thin film. (a) Voltage data taken in the time domain from the difference channel and (b) its Fourier transformed data, showing a single resonance frequency. (c) Accumulated Fourier transformed data of (b) after sweeping over various H_{app}. 57

Figure 4.1. Schematics of mechanism of magnetostriction below T_C (a) without applied magnetic field and (b) with applied magnetic field. The ellipses represent the electron clouds belonging to each atom, the dark area at the center of the ellipses represents atomic nuclei, the arrows at the center of the electron clouds indicate the vector of the net magnetic moment per atom.....62

Figure 4.2. Magnetostriction coefficient of Terfenol-D at 0.5 kOe under 10 MPa from multiple lots, where x-axis shows the individual lot identification number. The dashed line indicates their averaged magnetostriction coefficient.[79] 66

Figure 4.3. Magnetostriction coefficient of $Co_{1-x}Fe_x$ at three different post deposition treatments; as deposited (black dots), annealed and slow-cooled (blue dots), annealed and water quenched (red dots).[75] 67

Figure 4.4. Magnetostriction of $Fe_{1-x}Ga_x$ alloys at different thermal treatments as a function of Ga composition.[76] 68

Figure 4.5. (a) Schematics of the sample construction considered in SAW excited magnetization dynamics. (b) Cross-section of the sample set up.[31] 70

Figure 4.6. Dispersion plot using the solution obtained from equation 4.13. [31] The k represents k_x, and H represents H_{app} in the main text. 75

Figure 4.7. (a-c) Experimental geometries for three different configurations of applied external magnetic field ($\mu_0 \boldsymbol{H}$) and its angle (ψ) away from the major axis**.** (a) in-plane (IP) where $\mu_0 \boldsymbol{H}$ lies within the xy film plane, (b) out-of-plane 1 (OOP1) where $\mu_0 \boldsymbol{H}$ lies within the xz plane, (c) out-of-plane 2 (OOP2) where $\mu_0 \boldsymbol{H}$ is rotated from OOP1 configuration by $\pi/4$ with respect to the $\hat{z}$ axis. (d-f) Side-by-side comparison of measurement and simulation data of P_{abs}, $|S_{21}^{norm}|$, and $arg(S_{21}^{norm})$ for various applied magnetic fields and angles. 81

Figure 4.8. (a) SEM image of an array of polycrystalline Ni nanomagnets. (b) Schematics showing the thermal excitation method. Ni nanomagnet arrays (periodicity = p) patterned on an AR-coated on Si substrate. The red circle on top of the nanomagnets represents the probe beam and the blue circle represents the pump beam. [85] 83

Figure 4.9. (a) displacement of nanomagnet at different timing of thermal excitation in a periodic unit cell. The amplitude of nanomagnet is exaggerated for better display. (b) Effective magnetoelastic field induced at magnetic element.[86] 84

Figure 4.10. TR-MOKE spectra taken from the magnonic channel measured for (a) Ni film and (b) array of Ni nanomagnets presented in figure 4.8, and (c) the spectra taken from the phononic channel for Ni nanomagnets (white arrows: SAW frequencies).[85]86

Figure 4.11. (a) Schematics and SEM image of an array of nanomagnet capped with SiN dielectric layer. (b-d) Fourier spectra taken from the magnonic channel for (b) Ni film, (c) uncoated array (without SiN layer), and (d) coated array (with SiN layer).[89] 88

Figure 4.12. (a) Effective damping parameter for Ni film (unfilled square), uncoated array (red diamond), and coated array (blue dots). (b) OOMMF simulation of Δm_z for a single nanomagnet and an array of nanomagnet (Ensemble).[89] 89

Figure 4.13. (a) SEM images of periodic array (left) and randomized array (right). (b) Fourier spectra at $H_{app} = 4.5\ kOe$ and $6\ kOe$ for periodic (left) and randomized (right) array.[91] 91

Figure 4.14. Effective damping parameter of Kittel mode or magnetoelastically coupled mode for (a) periodic array and (b) randomized array – see figure 4.13.[91] 93

Figure 4.15. (a) Schematics of cold excitation method using SAW grating bars and the Ni nanomagnet. (b) SEM image of SAW gratings and the Ni nanomagnet.[92].....94

Figure 4.16. (a-b) Time traces and (c-d) corresponding Fourier spectra of magnetization precession taken with TR-MOKE using the hot excitation method for (a, c) Ni film and (b, d) a single Ni nanomagnet (NM). (e-f) Time trace and (g-h) corresponding Fourier spectra of a single Ni nanomagnet using the cold excitation method. (e-g) Data taken from magnonic channel. (f-h) Data taken from phononic channel.[92] 95

Figure 4.17. (a) Effective damping parameter at various magnetic field taken for Ni film with hot excitation method (black circles), a single Ni nanomagnet with hot excitation method (pink square), a single Ni nanomagnet with cold excitation method (MEL driven NM, blue triangle). (b) Pinning width (ΔH_P) taken with 4 different SAW frequencies.[92] 98

Figure 4.18. (a) SEM image of a single nanoelement considered in the theoretical and experimental calculation. (b) The coordinate system defined in this section.[32] 101

Figure 4.19. Fourier spectra of time traces taken from TR-MOKE measurement of a single Ni nanomagnet displayed in figure 4.18a showing avoided crossing for phononic mode (a) (1,1) and (b) (2,0).[32] 106

Figure 4.20. (a) The weighted coupling energy calculated for $0 < \phi_{mp} < 2\pi$ and $0 < H_{app} < 5.0\ kOe$. (b) ϕ_{mp} dependent calculated minimum frequency separation Δf_{min}. (c-d) Fourier spectra measured with TR-MOKE technique for phononic mode (2,0) for (c) $\phi_{mp} = 0°$ and (d) $\phi_{mp} = 45°$.[32] 107

Figure 5.1. Illustration of fabrication process for poly-crystalline CoFe nanomagnet. The process starts from left to right. 109

Figure 5.2. (a) SEM image of a nanomagnet ($208 \times 208 \times 30\ nm^3$) fabricated using the process mentioned in figure 5.1(a). (b) Geometry of H_{app} and $k_{(1,1)}$ with respect to x, y, z coordinate on an SEM image of an arbitrary p-CoFe nanomagnet. (c, d) Fourier-transformed TR-MOKE data presented in the frequency domain initially taken in the time domain by sweeping the externally applied magnetic field ($3\ kOe \leq H_{app} \leq 6\ kOe$). (c) The frequency response of magnonic dynamics of the CoFe thin film. Black circles represent the experimentally taken data points and the red line is the fit to the Kittel mode for poly-crystalline thin film. (d) The frequency response of magnonic (left) and phononic (right) response of the CoFe NM. The pink (blue) dotted line demonstrates the magnonic (phononic) frequency without the presence of magnon-phonon coupling, and he black solid line represents the fit to the coupled magnon-phonon dynamics showing great agreement with the experimentally obtained data.110

Figure 5.3. (a) Mode splitting of two frequencies at $(1,1)$ crossing, marked with arrows. The Lorentzian was done with three frequencies responsible for $(1,0)$ and $(1,1)$ crossings. Two frequencies fitted for the $(1,1)$ crossing are shown with blue and pink lines with their peaks are marked with arrows. The minimum splitting of two peaks was found at $H_{app} = 4.75\ kOe$ (highlighted). (b) The mode splitting of the CoFe NM at the phononic $(1,1)$ crossing. The red dots are the frequency splitting taken experimentally,

and the red solid line represents the fit of frequency splitting. The error bar represents the standard deviation. 113

Figure 6.1. Sample geometry. (a) Top-down view of CoFe and CMS films with respect to the MgO film and the azimuthal angles. The CoFe and CMS ⟨110⟩ directions are parallel to the MgO ⟨001⟩ direction and the x-axis. Inset shows the geometry of the applied magnetic field with respect to the cartesian coordinate and the corresponding polar coordinate. (b) The unit cell of magnetic single layer CoFe film on MgO substrate. The magnetic easy-axis (green arrow) of the CoFe film corresponds to the ⟨110⟩ direction and $\phi_H = 0^\circ$, and the magnetic hard-axis (red arrow) of the CoFe film corresponds to the ⟨100⟩ direction and $\phi_H = 45^\circ$. (c) The unit cell of CMS film grown on top of the CoFe film and the MgO substrate. The magnetic easy-axis (green arrow) of the CMS film corresponds to the ⟨110⟩ direction and $\phi_H = 0^\circ$, and the magnetic hard-axis (red arrow) of the CMS film corresponds to the ⟨100⟩ direction and $\phi_H = 45^\circ$.[138] 121

Figure 6.2. X-ray analysis of CoFe/CMS magnetic bilayer film. (a) X-ray reflectivity to measure the thickness of the CoFe/CMS layers. The red curve represents the measured data while the black curve is a fit to an optical scattering model with 1.69 nm of CoFe, 6.95 nm of CMS, and 0.3 nm of interface roughness at each interface. The gray curve is the residual [$\log_{10}$ (measured data) – $\log_{10}$ (model calculation)]. (b) Pole figure of the CMS {202} peaks and the MgO substrate {202} peaks about the surface normal, corresponding to the MgO [001] direction, showing the alignment of the in-

plane CMS [100] and the MgO [110] crystallographic directions. (c) Top: X-ray diffraction $\theta - 2\theta$ scan data (red) obtained with the scattering vector $\vec{q}$ along the direction perpendicular to the film's plane. Bottom: $\theta - 2\theta$ scan obtained with $\vec{q}$ along the CMS [022] direction with Gaussian lineshape fits. Gaussian peaks were fit to the data (green, blue), with the black curve being the sum of the two peaks. [138] 123

Figure 6.3. X-ray analysis of CoFe reference magnetic film. (a) X-ray reflectivity to measure the thickness of the CoFe layer. The red curve represents the measured data while the black curve is a fit to an optical scattering model with 10.8 nm of CoFe and 1.4 nm of MgO capping layer, and 0.5 nm of interface roughness at each interface. The gray curve is the residual [$\log_{10}$ (measured data) – $\log_{10}$ (model calculation)]. (b) Pole figure of the CoFe {101} peaks and the MgO substrate {202} peaks about the surface normal, corresponding to the MgO [001] direction, showing the alignment of the in-plane CoFe [100] and the MgO [110] crystallographic directions. (c) Top: X-ray diffraction $\theta - 2\theta$ scan data (red) obtained with the scattering vector $\vec{q}$ along the direction perpendicular to the film's plane. Bottom: $\theta - 2\theta$ scan obtained with $\vec{q}$ along the CoFe [101] direction with Gaussian lineshape fits. Gaussian peaks were fit to the data (green, blue), with the black curve being the sum of the two peaks.[138]. 126

Figure 6.4. (a) Time trace and (b) its Fourier transformed data of a magnetic single layer CoFe thin film to illustrate the data analysis. The time trace data was taken at $H_{app} = 5\ kOe, \theta_H = 55^{\circ}, \phi_H = 5^{\circ}$. 129

Figure 6.5. (a, c) Precession frequency of a single magnetic CoFe film at various applied magnetic fields. The scatter plots are TR-MOKE experimental data and the line plots show Kittel fitting. (b) Experimentally taken effective damping parameter of the corresponding single magnetic CoFe film at various applied magnetic fields. The TR-MOKE data in (a) and (b) were taken at a constant magnetic field ($5\ kOe$) applied at three polar angles ($\theta_H = 30^{\circ}, 45^{\circ}$ and 55° from left to right), while sweeping the azimuthal angles from $\phi_H = -5^{\circ}$ to $85^{\circ}$to probe the fourfold symmetry of the cubic crystal. The red dashed (green dotted) lines are guides to the eye to denote when the in-plane component of the applied magnetic field is along the magnetic hard (easy)-axis. The TR-MOKE data in (c) was taken at $H_{app} = 5\ kOe$ and $\theta_H = 30^{\circ}$, while the azimuthal angles were wept from $\phi_H = -5^{\circ}$ to 175°. 130

Figure 6.6. (a) Schematics of azimuthal angles of applied magnetic field and magnetization. $\phi_M = 0°$ is defined along one of the principal axes of cubic crystals ($\langle 100 \rangle$ in this work), whereas $\phi_H = 0°$ is defined diagonal to the cubic crystals ($\langle 110 \rangle$ in this work) along the $\langle 100 \rangle$ of MgO substrate. The polar angles of applied magnetic field and magnetization are defined at $\theta_{H,M} = 0°$ aligning with the z-axis. In this example in figure 6.6, the applied magnetic field is fixed at $\theta_H = 30°$ and $\phi_H = 0°$, while the amplitude of the magnetic field was swept from $1\ kOe \leq H_{app} \leq 5\ kOe$. (b-e) (b) Zeeman free energy, (c) Shape anisotropy free energy, (d) Magnetocrystalline anisotropy free energy, and (e) Uniaxial anisotropy free energy at various magnetization directions. (f) Total free energy at various magnetization directions. The

local minimum free energy was found at $\theta_M = 80.43°$ and $\phi_M = 45.00°$ at $H_{app} = 5\ kOe$. Note that the free energies in (b-f) are not normalized to M_S. (g) θ_M and (h) ϕ_M at various applied magnetic fields. (i) The corresponding Kittel mode at various applied magnetic field.....134

Figure 6.7. (a-c) Frequency response of CoFe/CMS magnetic bilayer at various applied magnetic fields. The magnetic field was applied at three polar angles $\theta_H =$ (a) 30°, (b) 45° and (c) 55°, and various azimuthal angles from $\phi_H = 0^{\circ}$ to 90°(left to right) while sweeping the intensity of applied magnetic field from $1\ kOe$ to $5\ kOe$. (d) Frequency response of (a-c) taken at $H_{app} = 1\ kOe$ (triangles), $3\ kOe$ (squares) and $5\ kOe$ (circles). The scatter plots are taken from TR-MOKE experimental data and the line plots are taken from the Kittel fitting. The green (red) dashed lines are guides to the eye to denote where the in-plane component of applied magnetic field is along the magnetic easy (hard) axis. [138].....137

Figure 6.8. Effective magnetic damping parameter of CoFe/CMS magnetic bilayer film taken from the same data set as in figure 5. (a) The data were taken when the magnetic field was applied from $1\ kOe$ to $5\ kOe$, at three polar angles ($\theta_H = 30^{\circ}$, 45° and 55°, from left to right) and various azimuthal angles from $\phi_H = 0^{\circ}$ to 90°. Again, the green dotted (red dashed) lines are guides to the eye to denote when the in-plane component of the applied magnetic field is along the magnetic easy (hard) axis. (b) Effective damping parameter as a function of azimuthal angle at representive three applied fields for comparision, showing a strong orientational dependence at low fields and

convergence to the intrinsic Gilbert damping at high fields due to the elimination of inhomegeneous broadening. [138].....139

Figure 7.1. Comparison between the polycrystalline CoFe (p-CoFe) thin film and the single-crystalline CoFe (s-CoFe) thin film depicting the lower effective magnetic damping in s-CoFe thin film. (a, b) Illustration of magnetization precession out-of-phase in p-CoFe (a) and in-phase in s-CoFe (b). (c-f) TR-MOKE data collected in time domain for p-CoFe (c) and for s-CoFe (d), and their Fourier transformed data in frequency domain for p-CoFe (e) and s-CoFe (f). The data were taken at $H_{app} = 5\ kOe$, $\theta_H = 30°$, and $\phi_H \parallel < 110 >_{CoFe}$. 144

Figure 7.2. Three major patterning processes considered in this chapter for patterning a single-crystalline CoFe nanomagnet using Ar^+ IBE. (a) Metal sacrificial layer with HSQ mask. 147

Figure 7.3. (a) Screen capture of an NPGS drawing file for a positive-tone EBL using PMMA with corner shaping. The size of the corner shape is marked with yellow arrows. (b) SEM images of square nanomagnets with and without corner shapes. The scale bar is $100\ nm$.....149

Figure 7.4. Wet etchant tolerance test on p-CoFe film and MgO film. (a, d) Optical microscope images showing before etching test (As prepared), after wet etching but before removal of photoresist, and after wet etching after removal of photoresist (PR) to compare the protected (covered by PR) and exposed area. (a) Tolerance test using the gold etchant. The photoresist covers the left top of the p-CoFe sample and bottom

of the MgO sample in the figure. The exposed area shows damages caused by etching from gold etchant. (b) SEM image of protected area covered by PR on p-CoFe sample. (c) SEM image of exposed area on p-CoFe sample. (d) Tolerance test using the copper etchant. The photoresist covers the right side of the p-CoFe and the MgO samples in the figure. The exposed area shows no damages caused by etching from copper etchant. 151

Figure 7.5. (a-e) SEM images of (a) PMMA soft mask on Ni test sample before IBE process, (b) HSQ hard mask on p-CoFe /Al_2O_3/Cu layer before IBE process, (c) PMMA soft mask on Ni test sample after ion-beam etched after fallen, (d) Ni test nanomagnet showing large area of redeposition (white circularly sputtered area around the square nanomagnet) of PMMA occurred during IBE process, and (e) PMMA protection layer (brighter area around the 4 etched squares) over the large area of the film after IBE process with beam voltage at $800\,V$. (f) Dimensions of the nanomagnet versus electron-beam dose for EBL process. 153

Figure 7.6. (a) Sequence of patterning process steps. (b) SEM images of the single-crystalline CoFe nanomagnets fabricated using the process described in (a). The size of square NM was fabricated between $185 \sim 337\ nm$ in length. (c) The tilted SEM image of the right-most NM in (b). The scale bar is $300\ nm$. 156

Figure 7.7. Fourier transformed TR-MOKE data in the frequency domain for the identical s-CoFe thin film measured (a) fresh after growth, (b) before patterning, and (c) after patterning process. The scatter plots show TR-MOKE data, and the solid lines

are the Kittel mode. The data were taken at $1\ kOe \leq H_{app} \leq 5\ kOe$, $\theta_H = 30°$, and $\phi_H = 0°$ or $\phi_H = 45°$. 158

Figure 7.8. (a) SEM image of multiple isolated s-CoFe NMs. Red circled area represents the probe beam. The H_{app} is applied along the $\hat{x}$-axis parallel to the edge of the nanomagnet. (b) SEM image of an arbitrary nanomagnet and H_{app} and $k_{(1,0)}$ with respect to the geometry of the nanomagnet. (c) Crystalline orientation of s-CoFe (represented by pink spheres) with respect to the shape of the nanomagnet (outlining grey square) (d, e) Fourier transformed TR-MOKE data in frequency domain. (d) Magnonic dynamics of s-CoFe thin film and (e) Magnonic (left) and Phononic (right) dynamics of s-CoFe NM. 160

Figure 7.9. (a) Fourier transformed TR-MOKE data in frequency domain with $0.75\ kOe \leq H_{app} \leq 3.5\ kOe$. The Lorentzian distribution of two main frequencies responsible for magnon-phonon coupling are plotted with blue and pink lines. (b) The Δf of two corresponding peaks vs. H_{app}. The TR-MOKE data are plotted with scatter plot and the fitting is plotted with red solid line. Error bars represent the uncertainties calculated using covariance function. 162

List of Tables

Table 2.1. List of magnetic unit conversion between Gaussian unit system to SI unit system. 5

Table 2.2. List of select textbooks for studying the field of Magnetism. 7

Table 2.3. Table of demagnetization tensor for different shapes of magnetic specimen. 27

Table 4.1. Magnetostriction coefficients for selected magnetostrictive materials. 65

Table 5.1. Summary of coupling strength, loss rate, cooperativity between Ni NM and poly-crystalline CoFe NM. 115

Table 5.2. Summary of coupling strength, volume, number of spins, cooperativity, coupling strength for a single Bohr magneton, and cooperativity per unit volume between YIG sphere, Ni NM and poly-crystalline CoFe NM. * Note that the parameters for YIG sphere were taken from magnon-photon coupling. 116

Table 6.1. The summary of fitted magnetic parameter of CoFe and CoFe/CMS bilayer from this work and the references.....139

Table 7.1. Summary of magnetic parameters of γ, M_S, K_1, and K_{Uni} measured and fitted for three different times. 159

Table 7.2. Summary of coupling strength, loss rate, cooperativity between Ni NM, p-CoFe NM, and s-CoFe NM.....163

Table 7.3. Summary of coupling strength, volume, number of spins, cooperativity, coupling strength for a single Bohr magneton, and cooperativity per unit volume between YIG sphere, Ni NM, p-CoFe NM, and s-CoFe NM. * Note that the parameters for YIG sphere were taken from magnon-photon coupling. 164

Abstract

MAXIMIZING STRONG MAGNON-PHONON COUPLING IN SINGLE NANOMAGNETS

by

Sujung Kim

Recent advances in quantum technologies have garnered significant attention due to their promising applications in future computing, sensing, and various other fields. At the core of these advancements lies the hybrid quantum system, which leverages the advantages of two quanta through their coherent coupling. The key figure of merit for quantifying the strength of the coherent coupling is cooperativity, C, where $C > 1$ indicates strong coupling. Among the various hybrid systems, spin waves (magnons) stand out due to their tunability in high-frequency applications up to the THz range. However, magnons suffer from a short lifetime. In this context, collective lattice vibrations (phonons) can significantly enhance magnons when coherently coupled to magnons due to their longer lifetime. Recently, Strong coupling in a magnon-phonon hybrid system was experimentally demonstrated using a single polycrystalline nickel (Ni) nanomagnet, showcasing the potential of magnonic hybrid quantum systems coupled to phonons.

In this thesis, an engineering strategy to improve hybrid magnon-phonon quantum systems in the technologically relevant cobalt iron (CoFe) material system is presented,

achieving a 23 times enhancement compared to a single Ni nanomagnet. First, the materials engineering perspective will be presented by introducing CoFe, a material readily available and commercially used in spintronics applications, such as data storage devices. CoFe possesses a high magnetostriction coefficient, which benefits the strength of magnon-phonon coupling. In order to minimize damping and maximize coherent coupling, epitaxially grown, single-crystal CoFe is chosen. First, optical characterization of the magnetic dynamics in an epitaxially-grown CoFe thin film is presented, showing significantly improved performance compared to polycrystalline films. Next, the development of a nanofabrication process to define high-quality single crystal CoFe nanomagnets is discussed. Using this process, we achieved a cooperativity of $C = 38$ in a single CoFe nanomagnet, representing a 23-fold improvement in cooperativity compared to systems using poly-crystalline Ni. This work identifies CoFe as a promising candidate for rare-earth-free magnon-phonon hybrid quantum systems.

Acknowledgement

First and foremost, I would like to thank my advisor, Professor Holger Schmidt for his patience and guidance throughout my journey to the Ph.D. program and for being an inspiring role model. I admire his wisdom and care for his students. One of my favorites out of many of his famous sayings is “Don’t try it. Just do it.”. This deeply helped me push through my hardships to finish the program. I send my appreciation to Dr. Tom Yuzvinsky in our group, for his expertise and creativity to excel my research. I would also like to thank to my academic uncle, Professor David Ledermann. I enjoyed the hours-long discussion in the lab, and I felt grateful to work as part of his group. I would also like to express my appreciation to my committee members, Professor Nobuhiko Kobayashi and Professor Marco Rolandi.

To all my friends from Santa Cruz, it is a rejoicing to have them both in the lab and my life, from the first hi to the last bye of the day, it makes my day. We began our journey together not knowing this area too well, getting to know the place together. We saw each other growing up from kidults (kid-adult, often used in Korean slang) to adults, meeting their significant others, and sharing the most important events in their lives. Each one of the members of the Applied Optics Group I met was amazing and inspiring. I learned something from them every day, every inch of the moment I interacted with them. It was the most special and fun time in my life. To my favorite neighbors, the

ladies in the quad in Nobel Drive (not Noble, it is Nobel as in the scholar's name because it is located near the university), let's go for dinner.

Not to mention my friends from childhood, 유정, 현주, 효진, 수완, and all my friends for being always there for me and endlessly trusting and supporting my decisions in my life.

The most important part of my life is my tutti family. To my parents, and sister and brother, 제가 박사과정을 마칠 수 있도록 믿어주고 응원해 주셔서 감사합니다. 사랑해요. To my Dutch parents, Tanja and Arjan, ik ben ontzettend dankbaar om deel uit te maken van de gezellige Nederlandse familie. To 꼬순이 (A.K.A. Koko), my kitty cat, your cheerful meow always lifts my soul. I sincerely hope you can read this. Finally, yet most importantly, to my best friend and my fiancé, Jan, you showed unconditional love and support. I am excited to enter the new chapter together, as you said, our dreams are bigger than our tacos.

할머니께 바칩니다.

To my grandmother.

Chapter 1. Introduction

The characteristics of spin waves (magnons) provide opportunity to couple the magnonic system to multiple systems to take advantage of their superior tunability at microwave frequencies. One of the most intriguing options is coupling between magnetic and mechanical oscillations, either traveling (acoustic) waves or localized vibrations whose frequencies are determined by the sample geometry. Indeed, controlling magnonic dynamics using phonons or vice versa has long been studied since the early theoretical work by C. Kittel and B. A. Auld.[1,2] Kittel suggested that magnetoelastic coupling can influence magnetization dynamics in the microwave range. This was experimentally validated by Bömmel and Dransfeld using Ni and yttrium iron garnet (YIG) in 1959.[3] These initial works spurred numerous theoretical and experimental studies since then.[4–10]

On the other hand, nanoscale structures are the basic building blocks for magnetic and spintronic devices, e.g. for applications in data storage, memory or sensors[13,14]. Particularly, the frequencies of elastic standing modes in nanoelements can overlap with those of magnetization precession in the range of GHz. As for the traveling surface acoustic waves (SAWs), their fundamental frequencies often lie in the MHz range. In that case, higher harmonics are used to match the frequency of SAWs and magnons to

realize coherent magnetoelastic coupling. This has recently led to the exploration of magnon-phonon coupling in nanostructures, both dense arrays and individual nanomagnets, and a rich playing field for investigation of the impact of magnetoelastic coupling has emerged. There are excellent opportunities in this field, including strain-induced magnetic switching in nanostructures towards energy-efficient and nonvolatile straintronic logic and memory technologies[11–18], spectral control up to 400 GHz opening the pathway towards the THz novel thermal devices[19], magnetoelastic metamaterials as a new generation of metamaterials[20], strain-mediated domain wall motion as an alternative approach for thermal management[21,22], low power spin-wave computing[23–28], and ground-breaking hybrid quantum systems for quantum information technology[29–48].

A thorough understanding of the dynamics of magnetoelastically coupled systems is a necessary foundation for unlocking the potential of straintronics, magnonics, and quantum information technology. The goal of this dissertation was to demonstrate maximization of strong magnon-phonon coupling by careful choice of the magnetic material and nanofabrication process. We first review recent work on ultrafast magnetization dynamics in nanomagnets in the presence of magnetoelastic coupling. We will then show how magnetoelastic effects can perturb and mask the intrinsic magnetization dynamics, how we can control these effects by way of sample geometry and experimental design, and how we can maximize magnetoelastic effects to enter the new physical regime of strong magnon-phonon coupling. Specifically, the thesis is organized as follows: We begin with the review of magnetization dynamics in a thin

film. Before delving into the recent studies of coupled magnon-phonon systems, detection methods for investigating the hybrid quantum system will be explored. The fundamentals of magnetostriction and its inverse effect, magnetoelastic effect (Villari effect) will be reviewed in the following chapter. Strong coupling of magnon-phonon system will be explored in a polycrystalline CoFe single nanomagnet. Then, epitaxially grown CoFe thin films are investigated as a foundation work to improve the coupling strength in a CoFe nanomagnet. We then describe the development of a new fabrication method for single-crystalline CoFe nanomagnets and demonstration of maximized Strong coupling in a single-crystalline CoFe nanomagnet. Finally, we will present future work and outlook for emerging applications and technologies that can benefit from these optimized quantum phenomena.

Chapter 2. Magnetization Dynamics

2.1. Introduction

In magnetic unit systems, there are two equally used unit systems. One is $Gaussian$ system or $CGS-EMU$ (centimeters, grams, seconds - electromagnetic unit) system, and the other is SI (Système International d'unités) system or MKS (meters, kilograms, seconds) system. The conversion between the two systems is very often required as researchers choose to use different types of unit systems.

Symbols	**Quantity**	**Gaussian Units**	**Conversion Factor (cgs → × mks)**	**SI Units**
l	Length	cm	10^{-2}	m
m	Mass	g	10^{-3}	kg
t	Time	s	1	s
E, U, W, F	Energy	erg	10^{-7}	J
Φ	Magnetic Flux	Mx	10^{-8}	Wb
			10^{-8}	V · s

$\vec{\boldsymbol{H}}$	Magnetic Field	Oe	$\frac{1}{4\pi}\times 10^3$	$\mathrm{A/m}$
$\vec{\boldsymbol{B}}$	Magnetic Induction	G	10^{-4}	T $\mathrm{Wb/m^2}$
$\vec{\boldsymbol{\mu}}$	Magnetic Dipole Moment	emu $\mathrm{erg/G}$	$4\pi\times 10^{-10}$	$\mathrm{Wb\cdot m}$
$\vec{\boldsymbol{M}}$	Magnetization	$\mathrm{emu/cm^3}$ $\mathrm{erg/(G\cdot cm^3)}$	10^3	$\mathrm{A/m}$
$4\pi\vec{\boldsymbol{M}}$	Magnetization	G	$\frac{1}{4\pi}\times 10^3$	$\mathrm{A/m}$
D	Demagnetization Factor	1	$\frac{1}{4\pi}$	1
χ	Susceptibility	1	4π	1
μ	Permeability	1	$4\pi\times 10^{-7}$	$\mathrm{H/m}$ $\mathrm{Wb/(A\cdot m)}$
μ_r	Relative Permeability	μ	1	μ_r
ϕ	Magnetic Scalar Potential	Gb	$\frac{1}{4\pi}\times 10^{-3}$	A

Table 2.4. List of magnetic unit conversion between Gaussian unit system to SI unit system.

Some of the textbooks that I found very helpful to read to understand the fundamental physics of magnetism are listed below. Even though the same concepts are introduced, different authors explain them in their unique ways. I hope this list of textbooks provide you a good start point of your journey to Magnetism.

Author	Title	Publisher	Edition	Year
Steven H. Simon	The Oxford Solid State Basics	Oxford University Press	1st	2013
Allan H. Morrish	The Physical Principles of Magnetism	IEEE Press		
Sóshin Chikazumi	Physics of Ferromagnetism	Oxford Science Publications	2nd	1997
B. D. Cullity and C. D. Graham	Introduction to Magnetic Materials	IEEE Press Wiley	2nd	2009
J. M. D. Coey	Magnetism and Magnetic Materials	Cambridge		2010
A. G. Gurevich and G. A. Melkov	Magnetization Oscillation and Waves	CRC Press		1996
Mathias Getzlaff	Fundamentals of Magnetism	Springer		2008

David J. Griffiths	Introduction to Quantum Mechanics	Pearson	2nd	2005

Table 2.5. List of select textbooks for studying the field of Magnetism.

2.2. Microscopic Magnetization Dynamics

The use of magnetic materials goes back in time around B.C. 2500 in China where they used compass, and the Greek used magnetite to attract iron in B.C. 600. More scientific knowledge using modern mathematical language was only discovered by Coulomb when he designed an experiment to quantify the magnetic force between magnetic poles of steel rods. The two poles attract or repulse each other and their strength of such force is described in Coulomb's law as

$$\vec{\boldsymbol{F}} = k\frac{m_1 m_2}{r^2}\vec{\boldsymbol{r}}_{\boldsymbol{0}}, \tag{2.1}$$

where $\vec{\boldsymbol{F}}$ refers to force, k is the Coulomb constant, m_1 and m_2 are the magnetic poles, r is the distance between the two magnetic poles, and $\vec{r}_0$ is the unit vector directing along r. One way to understand this force better is to split the force into two terms, with the test pole, m_2, and the source that depends on the other pole and the location with respect to it, which is called magnetic field $\vec{\boldsymbol{H}}$. The magnetic field is defined as

$$\vec{\boldsymbol{H}} = \frac{m}{r^2}\vec{\boldsymbol{r}}_{\mathbf{0}}. \tag{2.2}$$

The magnetic field is related to a scalar potential ϕ, which is defined as

$$\vec{\boldsymbol{H}} = -\vec{\boldsymbol{\nabla}}\phi, \tag{2.3}$$

Where $\vec{\boldsymbol{\nabla}} = \hat{\boldsymbol{\imath}}\frac{\partial}{\partial x} + \hat{\boldsymbol{\jmath}}\frac{\partial}{\partial y} + \hat{\boldsymbol{k}}\frac{\partial}{\partial z}$ is the vector differential operator, often called as 'del' or 'nabla', and $\hat{\boldsymbol{\imath}}$, $\hat{\boldsymbol{\jmath}}$, $\hat{\boldsymbol{k}}$ are the unit vectors in a coordinate system – (x, y, z) for the Cartesian coordinate system or $(1, 2, 3)$ coordinate system for the transformed coordinate system adopted to describe the magnetization dynamics in the upcoming chapters.

2.2.1. Magnetic Dipoles

Despite the fact that an isolated magnetic monopole is theoretically anticipated, the observation of such monopole has never been successful. Instead, the magnetic dipoles occur as a pair of negative and positive poles, and its magnetic moment is defined as

$$\vec{\boldsymbol{\mu}} = m\vec{\boldsymbol{d}}, \tag{2.4}$$

where $\vec{\boldsymbol{d}}$ has a magnitude of the distance between the two magnetic poles denotes a vector pointing from negative magnetic pole to positive magnetic pole.

Now, if we place magnetic dipoles in a uniform magnetic field as shown in figure 2.1, the magnetic dipole moment will experience the torque L, described as

$$L = -\frac{\partial W}{\partial \theta} = -\left|\vec{\boldsymbol{\mu}}\right| H \sin\theta\,, \tag{2.5}$$

where W is the potential energy of a dipole in a magnetic field defined as $W = m(\phi_{+m} - \phi_{-m}) = \vec{\boldsymbol{\mu}} \cdot \vec{\nabla}\phi = -\vec{\boldsymbol{\mu}} \cdot \vec{\boldsymbol{H}}$, and θ is the angle between the uniform magnetic field and the magnetic dipole moment. This relation provides a rigid body rotation due to a torque provided by a uniformly applied magnetic field on a magnetic moment, given by

$$\vec{\boldsymbol{L}} = \vec{\boldsymbol{\mu}} \times \vec{\boldsymbol{H}}\,. \tag{2.6}$$

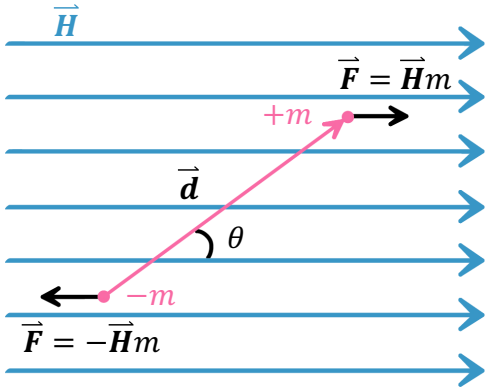

Figure 2.8. Magnetic dipoles placed inside a uniform magnetic field.

Thus, the uniformly applied magnetic field exerts a torque on the magnetic dipole. The reason why we learned this example is because it is closely related to the origin of magnetic dipole.

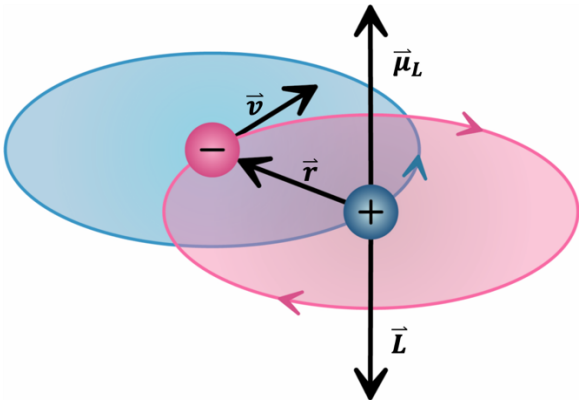

Figure 2.9. Illustration showing the L-S coupling in hydrogen atom. The argument in the main text views in electron's perspective.

Orbital angular momentum can be explained by introducing rather simple classical picture of a hydrogen atom composed of one proton and one electron in terms of Bohr's atomic model. From the proton's perspective, the electron is circularly orbiting around the proton. The moving electrons in a continuous loop can be viewed as a current

flowing in a wire centered around the proton. Then the electron *orbital angular momentum* $\vec{\boldsymbol{L}}$ is given by,

$$\vec{\boldsymbol{L}} = m_{\mathrm{e}}(\vec{\boldsymbol{r}} \times \vec{\boldsymbol{v}}), \tag{2.7}$$

where m_{e} is the electron mass, $\vec{\boldsymbol{r}}$ is the radius of orbit pointing from the proton to the electron, and $\vec{\boldsymbol{v}}$ is the electron's velocity. According to Ampère, the corresponding magnetic moment of the current loop is generally written as $\mu_{\mathrm{L}} = iA$, where the current $i = \frac{q}{T} = -\frac{e}{(2\pi r/v)}$, and the area $A = \pi r^2$, and the vector of μ_{L} follows the right-hand

rule. Thus, *the orbital magnetic moment* of an electron orbiting is $\vec{\boldsymbol{\mu}}_{\mathrm{L}} = -\frac{e}{2}\vec{\boldsymbol{r}} \times \vec{\boldsymbol{v}}$, and also expressed in terms of orbital angular momentum $\vec{\boldsymbol{L}}$,

$$\vec{\boldsymbol{\mu}}_{\mathrm{L}} = -\frac{e}{2m_{\mathrm{e}}c}\vec{\boldsymbol{L}}. \tag{2.8}$$

Notice that the orbital magnetic moment is antiparallel to the orbital angular momentum.

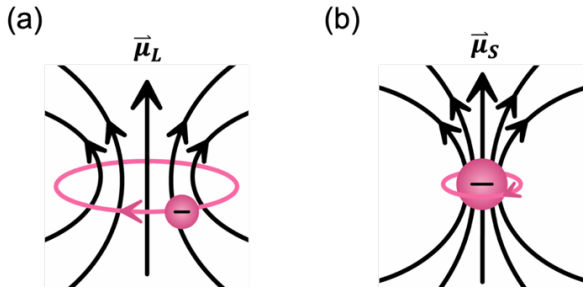

Figure 2.10. Two contributions to the magnetic moment, (a) orbital magnetic moment and (b) spin magnetic moment.

The electrons intrinsically possess another type of angular momentum, called *spin angular momentum*, $\vec{\boldsymbol{S}}$. As it turned out, the electron's *spin magnetic moment* was twice the orbital magnetic moment,

$$\vec{\boldsymbol{\mu}}_{\mathrm{S}} = -\frac{e}{m_{\mathrm{e}}c}\vec{\boldsymbol{S}}, \tag{2.9}$$

The ratio between the orbital magnetic moment and the orbital angular momentum is called *gyromagnetic ratio,* γ, given by

$$\vec{\boldsymbol{\mu}}_{\mathrm{L}} = -\gamma_{\mathrm{L}}\vec{\boldsymbol{L}},$$

$$\vec{\boldsymbol{\mu}}_{\mathrm{S}} = -\gamma_{\mathrm{S}}\vec{\boldsymbol{S}}, \tag{2.10}$$

where $\gamma_{\mathrm{L}} = \frac{e}{2m_{\mathrm{e}}c}$ for an orbital motion of electron, and $\gamma_{\mathrm{S}} = \frac{e}{m_{\mathrm{e}}c}$ for an electron spin.

Alternatively, the g-factor is also used to describe the relationship of orbital magnetic momentum and orbital angular momentum. The gyromagnetic ratio is related to the

fundamental units of Planck constant $\hbar$, and the Bohr magneton μ_{B}, which is described by

$$\gamma_{\mathrm{L}} = g_{\mathrm{L}} \frac{|\mu_{\mathrm{B}}|}{\hbar},$$

$$\gamma_{\mathrm{S}} = g_{\mathrm{S}} \frac{|\mu_{\mathrm{B}}|}{\hbar},$$

$$|\mu_{\mathrm{B}}| = \frac{|e|\hbar}{2m_{\mathrm{e}}c} = 0.9274 \times 10^{-20}\ \mathrm{erg/Oe}\,. \tag{2.11}$$

Using this relationship, the orbital magnetic moment is written by

$$\vec{\boldsymbol{\mu}}_{\mathrm{L}} = -\frac{g_{\mathrm{L}}|\mu_{\mathrm{B}}|}{\hbar}\vec{\boldsymbol{L}},$$

$$\vec{\boldsymbol{\mu}}_{\mathrm{S}} = -\frac{g_{\mathrm{S}}|\mu_{\mathrm{B}}|}{\hbar}\vec{\boldsymbol{S}}, \tag{2.12}$$

where $g_{\mathrm{L,S}}$ is the particle specific gyromagnetic splitting factors, also known as the Landé g-factor, which is $g_{\mathrm{L}} = 1.0 \times 1.00116$ for orbital motion, and $g_{\mathrm{S}} = 2.0 \times 1.00116$ for an electron spin.

In the presence of spin-orbit coupling, the *total angular momentum* $\vec{\boldsymbol{J}}$ becomes more insightful value, defined as

$$\vec{\boldsymbol{J}} = \vec{\boldsymbol{L}} + \vec{\boldsymbol{S}}. \tag{2.13}$$

The *total magnetic moment* is therefore written as,

$$\vec{\boldsymbol{\mu}}_{\mathrm{J}} = \vec{\boldsymbol{\mu}}_{\mathrm{L}} + \vec{\boldsymbol{\mu}}_{\mathrm{S}},$$

$$\vec{\boldsymbol{\mu}}_{\mathrm{J}} = -\gamma_{\mathrm{J}}\vec{\boldsymbol{J}},$$

$$\vec{\boldsymbol{\mu}}_{\mathrm{J}} = -g\vec{\boldsymbol{J}}|\mu_{\mathrm{B}}|, \tag{2.14}$$

where the generalized Landé g-factor for a free atom is approximated by

$$g = 1 + \frac{j(j+1) + s(s+1) - l(l+1)}{2j(j+1)}, \tag{2.15}$$

where $j, s,$ and l are the quantum numbers for the total angular momentum, spin angular momentum, and orbital angular momentum.

It is important to note that the $\vec{\boldsymbol{J}} = \vec{\boldsymbol{L}} + \vec{\boldsymbol{S}}$ does not always hold in multi-atomic structures. In solids, the periodically displaced neighboring atoms produce additional energy, which is considered as an electric field called, crystal field. Due to symmetry of the crystals, an electron orbit can couple to the crystal lattice more strongly than the spin-orbit coupling via orbit-lattice coupling, when external magnetic field is applied. In this case, the contribution of orbital angular momentum to the magnetic moment is quenched, resulting in the total angular momentum of $\vec{\boldsymbol{J}} = \vec{\boldsymbol{S}}$. This phenomenon is known as *quenching of angular momentum*.

2.2.2. Larmor Precession

Now, we locate this electron inside a uniform magnetic field, $\overrightarrow{\boldsymbol{H}}$. The equation of motion of the electron spin dynamics can be described by Heisenberg equation

$$i\hbar \frac{d}{dt}\langle \widehat{\boldsymbol{S}} \rangle(t) = \langle \big[\widehat{\boldsymbol{S}}, \mathcal{H}\big](t) \rangle, \tag{2.16}$$

where $\widehat{\boldsymbol{S}}$ is the spin operator, and $\mathcal{H} = -\overrightarrow{\boldsymbol{\mu}_{\mathbf{S}}} \cdot \overrightarrow{\boldsymbol{H}} = -\frac{g|\mu_B|}{\hbar}\vec{\boldsymbol{S}} \cdot \overrightarrow{\boldsymbol{H}}$ is the Hamiltonian of a spin in a spatially uniform magnetic field, called *Zeeman energy*. The x component of the right-hand side of the Heisenberg equation becomes

$$[S_x, \mathcal{H}] = -\frac{g|\mu_{\mathrm{B}}|}{\hbar}\big(H_y(t)\big[S_x, S_y\big] + H_z(t)\big[S_x, S_y\big]\big),$$

$$= -\frac{g|\mu_B|}{\hbar} i\hbar\big(H_y(t)S_z - H_z(t)S_y\big). \tag{2.17}$$

Applying the similar approach for the S_y, and S_z gives

$$\frac{d}{dt}\langle \widehat{\boldsymbol{S}} \rangle(t) = -\gamma_{\mathrm{S}}\left(\langle \widehat{\boldsymbol{S}} \rangle(t) \times \overrightarrow{\boldsymbol{H}}(t)\right). \tag{1.18}$$

Substituting the spin operator to the total magnetic momentum from the equation (2.16) is given by

$$\frac{d}{dt}\vec{\boldsymbol{\mu}}_{\mathbf{J}}(t) = -\gamma_{\mathrm{J}}\left(\vec{\boldsymbol{\mu}}_{\mathbf{J}}(t) \times \overrightarrow{\boldsymbol{H}}(t)\right). \tag{2.19}$$

This equation of motion describes a precession of the total magnetic moment about the axis of an externally applied magnetic field at an angle (see the Example 4.3 of Introduction to Quantum Mechanics by David Griffiths). It implies that the electron experiences torque $\vec{\boldsymbol{\tau}} = \vec{\boldsymbol{\mu}}_{\mathbf{J}} \times \overrightarrow{\boldsymbol{H}}$, due to the dipole rotating to parallelly align with the applied magnetic field. Solving this differential equation provides the Larmor frequency ω_L given by

$$\omega_L = \gamma_{\mathrm{J}} H. \tag{2.20}$$

In this very simple case considering applied magnetic field, the precession frequency linearly depends on the applied magnetic field. However, as we learn to include more energy terms in the magnetic system, the precession frequency should be carefully derived.

2.3. Competing Energies

According to the first law of thermodynamics, the free energy in the magnetic system at the constant temperature is given by

$$dU = TdS - dW, \tag{2.21}$$

where U is the internal energy of the system, T is the temperature of the system S is the entropy of the system, and $-dW$ is the work done *on* the system ($+dW$ is the work done *by* the system). The Helmholtz free energy is expressed by

$$F = U - TS. \tag{2.22}$$

At constant temperature the change in free energy is written by,

$$dF = -dW. \tag{2.23}$$

The magnetization dynamics in solids is more complicated than the dynamics of a single spin we learned by only considering the Zeeman energy term. Instead, there are energy terms associated with interactions of neighboring spins and long-range interaction. This include exchange energy, shape anisotropy (demagnetizing) energy, crystalline anisotropy energy, uniaxial anisotropy energy, and more. All the energy terms added to the magnetic system acting as an effective magnetic field, thus changing the magnetization dynamics. In the experimental settings, we can detect the precession frequency and deduce their dynamics.

$$G_{\text{total}} = G_{\text{Zeeman}} + G_{\text{Ex}} + G_{\text{Demag}} + G_{\text{Crystal}} \tag{2.24}$$

2.3.1. Zeeman Energy

Zeeman energy, E_{Zeeman} is associated with the externally applied magnetic field $\vec{\boldsymbol{H}}_{\text{app}}$ described by

$$E_{Zeeman} = -\int \vec{\boldsymbol{M}} \cdot \vec{\boldsymbol{H}}_{\text{app}} dV \,. \tag{2.25}$$

where $\vec{\boldsymbol{H}}_{\text{app}}$ is the externally applied magnetic field. This energy term is minimized by aligning the magnetization inside the magnetic specimen in parallel with the applied magnetic field.

2.3.2. Exchange Energy

The exchange energy has electrostatic origin describing the interaction between the neighboring spins. The exchange energy is given by

$$E_{\text{ex}} = -2\sum_{i,j} J_{ij} \vec{\boldsymbol{s}}_i \cdot \vec{\boldsymbol{s}}_j \,, \tag{2.26}$$

where $\vec{\boldsymbol{S}}_{i,j} = \sum_{i,j} \vec{\boldsymbol{s}}_{i,j}$ are the spins of neighboring electrons i and j, J_{ij} is the exchange integral of the electrons i and j, which is assumed to be a constant. Assuming that the exchange energy due to nearest neighboring atoms dominates the energy, and the exchange integral is isotropic, $J_{ij} = J_{\text{e}}$, the equation (2.26) is simplified to

$$E_{\text{ex}} = -2\sum_j J_e \vec{s}_i \cdot \vec{s}_j \,. \tag{2.27}$$

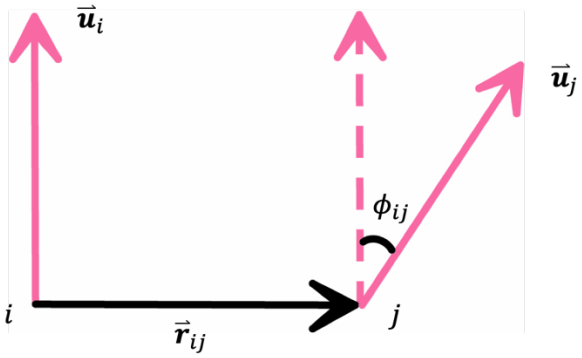

Figure 2.11. Schematics showing exchange energy between two neighboring spins, i and j.

In discussing the domain theory, the spin rotation between the neighboring spins is often approximated to be small angles, ϕ_{ij}. The equation (2.27) then is given by,

$$E_{\text{ex}} = -2J_e S^2 \sum_j \cos\phi_{ij} \,. \tag{2.28}$$

We assume that the angle between the neighboring spins is very small, thus taking the Taylor expansion of $\cos\phi_{ij}$ to the order of 2 gives $\cos\phi_{ij} \approx 1 - \frac{1}{2}\phi_{ij}^2$. The exchange energy contributing to the dynamics is then given by

$$E_{\text{ex}} = J_e S^2 \sum_j \phi_{ij}^2 \,. \tag{2.29}$$

Another method to approximate the equation (2.27) is more intuitive because it involves crystal symmetry. By introducing direction cosines, α_1, α_2, and α_3, with respect to $x-, y-$, and $z-$ axes and the unit vectors pointing parallel to the spin vectors of spin i and j are $\vec{\boldsymbol{u}}_i$ and $\vec{\boldsymbol{u}}_j$, respectively, and the $\vec{\boldsymbol{r}}_{ij}$ is the displacement vector between the two adjacent spins. As we assumed, ϕ_{ij} is very small, then the direction cosines of $\vec{\boldsymbol{u}}_j$ are Taylor expanded in terms of direction cosines of $\vec{\boldsymbol{u}}_i$,

$$\cos\phi_{ij} = \vec{\boldsymbol{u}}_i \cdot \vec{\boldsymbol{u}}_j$$

$$= \alpha_{1i}\alpha_{1j} + \alpha_{2i}\alpha_{2j} + \alpha_{3i}\alpha_{3j},$$

$$\alpha_{xi}\alpha_{xj} = \alpha_{xi}\left(\alpha_{xi} + \vec{\boldsymbol{r}}_{ij} \cdot \vec{\boldsymbol{\nabla}}\alpha_{xi} + \frac{1}{2}\left(\vec{\boldsymbol{r}}_{ij} \cdot \vec{\boldsymbol{\nabla}}\right)^2 \alpha_{xi} + \cdots\right), \qquad x = [x, y, z]. \quad (2.30)$$

Then we take the summation for the nearest spin, j. Simplifying the equation by using the property of $\sum_j x_{ij}^2 = \frac{1}{3}\sum_j r_{ij}^2$, $x = [x, y, z]$, and the symmetry in cubic crystal, for example, cross terms in $\frac{1}{2}\sum_j\left(\vec{\boldsymbol{r}}_{ij} \cdot \vec{\boldsymbol{\nabla}}\right)^2 \alpha_{xj}$ become 0. Then the equation (2.30) becomes,

$$E_{\text{ex}} = -2J_{\text{e}}S^2\left[z + \frac{1}{6}\sum_j r_{ij}^2\, \vec{\boldsymbol{u}}_i \cdot \vec{\boldsymbol{\nabla}}^2\vec{\boldsymbol{u}}_i\right]. \quad (2.31)$$

Finally, using the property of the vector identity $\vec{\boldsymbol{\nabla}}^2(\vec{\boldsymbol{u}}_i \cdot \vec{\boldsymbol{u}}_i) = 0$, and considering only the terms that contribute to the dynamics, we have

$$E_{\mathrm{ex}} = \frac{J_{\mathrm{e}} S^2}{3}\left[\sum_j r_{ij}^2 \left[\left(\vec{\nabla}\alpha_1\right)^2 + \left(\vec{\nabla}\alpha_2\right)^2 + \left(\vec{\nabla}\alpha_3\right)^2\right]\right]. \quad (2.32)$$

For cubic crystals, including simple cubic, body-centered cubic, and face-centered cubic structures, $\sum_j r_{ij}^2$ can be expressed by the lattice constant, a, $\sum_j r_{ij}^2 = 6a^2$. In this case, the equation rewrites

$$E_{\mathrm{ex}} = 2J_{\mathrm{e}} S^2 a^2 \left[\left(\vec{\nabla}\alpha_1\right)^2 + \left(\vec{\nabla}\alpha_2\right)^2 + \left(\vec{\nabla}\alpha_3\right)^2\right]. \quad (2.33)$$

Experimentally revealed $J_{\mathrm{e}}$was found be $J_{\mathrm{e}} = 205$ K for iron and $J_{\mathrm{e}} = 230$ K for nickel [49,50].

2.3.3. Crystal Anisotropy Energy (Magnetocrystalline Anisotropy Energy)

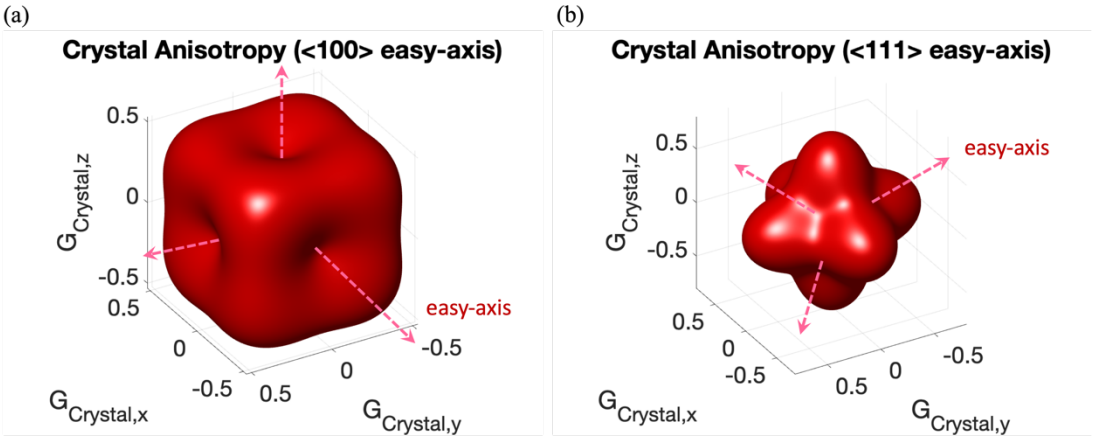

Figure 2.12. Magnetocrystalline energy for (a) BCC crystal and (b) FCC crystal. $G_{Crystal,i}$, $(i = x, y, z)$ represents the normalized energy calculated from equation (2.34) or equation (2.35). Action of having $K_1 > 0$ ($K_1 < 0$) for BCC (FCC) crystal increases (lowers) the total energy, providing lower energy for the magnetization to preferably align along the magnetic easy-axis in <100> (<111>) direction. K_2 was ignored in this calculation as $K_1 \gg K_2$.

Due to the spin-orbit interaction, the lattice structure influences the magnetic moments. Therefore, the crystal anisotropy energy depends on the crystal symmetry, which provides a preferable low-energy path for the magnetic moments to align. These directions are called magnetic easy-axis.

The crystal anisotropy energy in the cubic crystals, such as irons (Fe) and nickel (Ni), is expressed

$$E_{\text{Crystal}} = K_1\left(m_x^2 m_y^2 + m_y^2 m_z^2 + m_z^2 m_x^2\right), \tag{2.34}$$

where the K_1 is the crystal anisotropy constant, where $K_1 > 0$ for BCC crystals (Fe-like) and $K_1 < 0$ for FCC crystals (Ni-like). More generally, the direction cosines are used to describe the crystal anisotropy energy, given by

$$E_{\text{Crystal}} = K_1(\alpha_1^2\alpha_2^2 + \alpha_2^2\alpha_3^2 + \alpha_3^2\alpha_1^2), \tag{2.35}$$

where $\alpha_1 = \sin\theta_M \cos\phi_M$, $\alpha_2 = \sin\theta_M \sin\phi_M$, and $\alpha_3 = \cos\theta_M$ for cubic symmetry where θ_{M} is a polar angle of the magnetization vector and ϕ_{M} is an azimuthal angle of the magnetization vector. The crystal anisotropy energy possesses the 4-fold symmetry due to the 4-fold symmetry observed in cubic crystal system.

The anisotropy energy is often expressed in anisotropy magnetic field, H_{K_i} , which is related by

$$H_{\text{K}_\text{i}} = \frac{2K_i}{M_{\text{S}}}. \tag{2.36}$$

2.3.4. Uniaxial Anisotropy Energy

Uniaxial anisotropy energy can also depend on the crystal symmetry, similar to the crystal anisotropy energy, observed in hexagonal crystal system such as cobalt (Co). The uniaxial crystal anisotropy $E_{\mathrm{Uni,K}}$ is expressed,

$$E_{\mathrm{Uni,K}} = K_{\mathrm{u}1}(\sin\theta_M)^2 + K_{\mathrm{u}2}(\sin\theta_M)^4 + K_{\mathrm{u}3}(\sin\theta_M)^6 + \cdots, \qquad (2.37)$$

Where the coefficients $K_{\mathrm{u}n}$ $(n = 1, 2, 3, \ldots)$ are the uniaxial anisotropy constants. The $K_{\mathrm{u}1} > 0$ for Co crystals, therefore the uniaxial anisotropy energy is found to be minimum at $\theta_M = 0$, leaving the c-axis as an easy-axis for Co crystals.

Additionally, the uniaxial anisotropy is characterized by its 2-fold symmetry. Any significant perturbation in the order of anisotropy constants ($\sim 10^6$ [erg/cm^3]) can be expressed in terms of uniaxial anisotropy energy. One example is the perpendicular uniaxial anisotropy which is induced by biaxial strain due to lattice mismatch in epitaxially grown films, as it can introduce tetragonal distortion in cubic crystals. The uniaxial perpendicular anisotropy E_{Uni} is generally expressed to reflect the 2-fold symmetry using the uniaxial anisotropy constants similar to the equation (2.37),

$$E_{\mathrm{Uni}} = K_{\mathrm{u}}(\cos\theta_M)^2. \qquad (2.38)$$

2.3.5. Shape Anisotropy Energy (Demagnetization Energy)

In magnetic spheres without crystalline anisotropy, i.e. polycrystalline magnetic specimen, a preferred magnetic orientation does not exist. Instead, the energy concerning magnetization is isotropic due to its spherical shape. If the shape is not spherical, then a preferred magnetization axis occurs, which is the magnetic easy axis associated with the shape of the magnetic specimen. This anisotropy energy that arises due to the geometrical shape of the magnetic specimen is called *shape anisotropy energy*. The origin of it lies in the stray field and demagnetizing field, as the non-infinitely large magnetic sample possess magnetic poles on the surface, the stray field then mutually interacts with the magnetization inside the magnetic specimen as a demagnetization field.

The energy associated with the stray field of the sample is given by

$$E_{\text{demag}} = -\frac{1}{2}\int \vec{\boldsymbol{M}} \cdot \vec{\boldsymbol{H}}_{\text{demag}} dV\,, \tag{2.39}$$

where $\vec{\boldsymbol{H}}_{\text{demag}}$ is the demagnetizing field inside the magnetic specimen, and the $\frac{1}{2}$ was introduced to remove the counting of the same interaction between the two dipoles. $\vec{\boldsymbol{H}}_{\text{demag}}$ can be expressed using a demagnetizing tensor $\overleftrightarrow{\boldsymbol{N}}$ which depends on the shape of the magnetic specimen,

$$\vec{\boldsymbol{H}}_{\text{demag}} = -\overleftrightarrow{\boldsymbol{N}}\vec{\boldsymbol{M}}, \tag{2.40}$$

The equation (2.39) can then be written as

$$E_{\text{demag}} = \frac{V}{2}\overrightarrow{\boldsymbol{M}} \cdot \overleftrightarrow{\boldsymbol{N}}\overrightarrow{\boldsymbol{M}}. \tag{2.41}$$

The demagnetizing tensor has a property of only having diagonal tensor elements, $\overleftrightarrow{\boldsymbol{N}} = \begin{pmatrix} N_1 & 0 & 0 \\ 0 & N_2 & 0 \\ 0 & 0 & N_3 \end{pmatrix}$, and $\text{tr}\left(\overleftrightarrow{\boldsymbol{N}}\right) = 4\pi$. Using these relations and introducing the direction cosine α_1, α_2, and α_3, the stray field energy is now written by

$$E_{\text{demag}} = \frac{V}{2}M^2(N_1\alpha_1^2 + N_2\alpha_2^2 + N_3\alpha_3^2). \tag{2.42}$$

Shape	**Sphere**	**Cylinder**	**Plate**
Geometrical Symmetry Axis	Isotropic	3-axis	3-axis
$\overleftrightarrow{\boldsymbol{N}}$	$\begin{pmatrix} 4\pi/3 & 0 & 0 \\ 0 & 4\pi/3 & 0 \\ 0 & 0 & 4\pi/3 \end{pmatrix}$	$\begin{pmatrix} 2\pi & 0 & 0 \\ 0 & 2\pi & 0 \\ 0 & 0 & 0 \end{pmatrix}$	$\begin{pmatrix} 0 & 0 & 0 \\ 0 & 0 & 0 \\ 0 & 0 & 4\pi \end{pmatrix}$

Table 2.6. Table of demagnetization tensor for different shapes of magnetic specimen.

Let's take an infinitely large magnetic film as an example. The magnetization inside the magnetic film can either lie along the lateral direction (in-plane), or perpendicular to the surface (out-of-plane). The magnetization orientation prefers to align in-plane, because the effect of demagnetizing field vanishes as the magnetic surface charges on the edge of the magnetic film are infinitely separated. On the other hand, the demagnetizing field is not neglected when the magnetization inside the film points out-of-plane, as the distance between the surface magnetic charges are close to each other. Thus, the infinitely large magnetic film geometry provides $N_1, N_2 = 0$, and $N_3 = 4\pi$. In this case, the demagnetizing energy becomes,

$$E_{\text{demag}} = \frac{V}{2} M^2 (N_1 \alpha_1^2 + N_2 \alpha_2^2 + N_3 \alpha_3^2)$$

$$= \frac{V}{2} M^2 (N_3 \alpha_3^2)$$

$$= 2\pi V M^2 (\cos\theta)^2. \qquad (2.42)$$

The demagnetizing field acts inside the film, resulting in creating magnetic domains to compensate the surface and volume magnetic charges.

2.4. Macroscopic Magnetization Dynamics

In this section, we discuss the magnetization dynamics from an ensemble macro-spin point of view. The spin waves are the propagation of collective spins traveling at phase ϕ_{SW} and amplitude at a small angle θ_{SW}, as shown in figure 2.6.

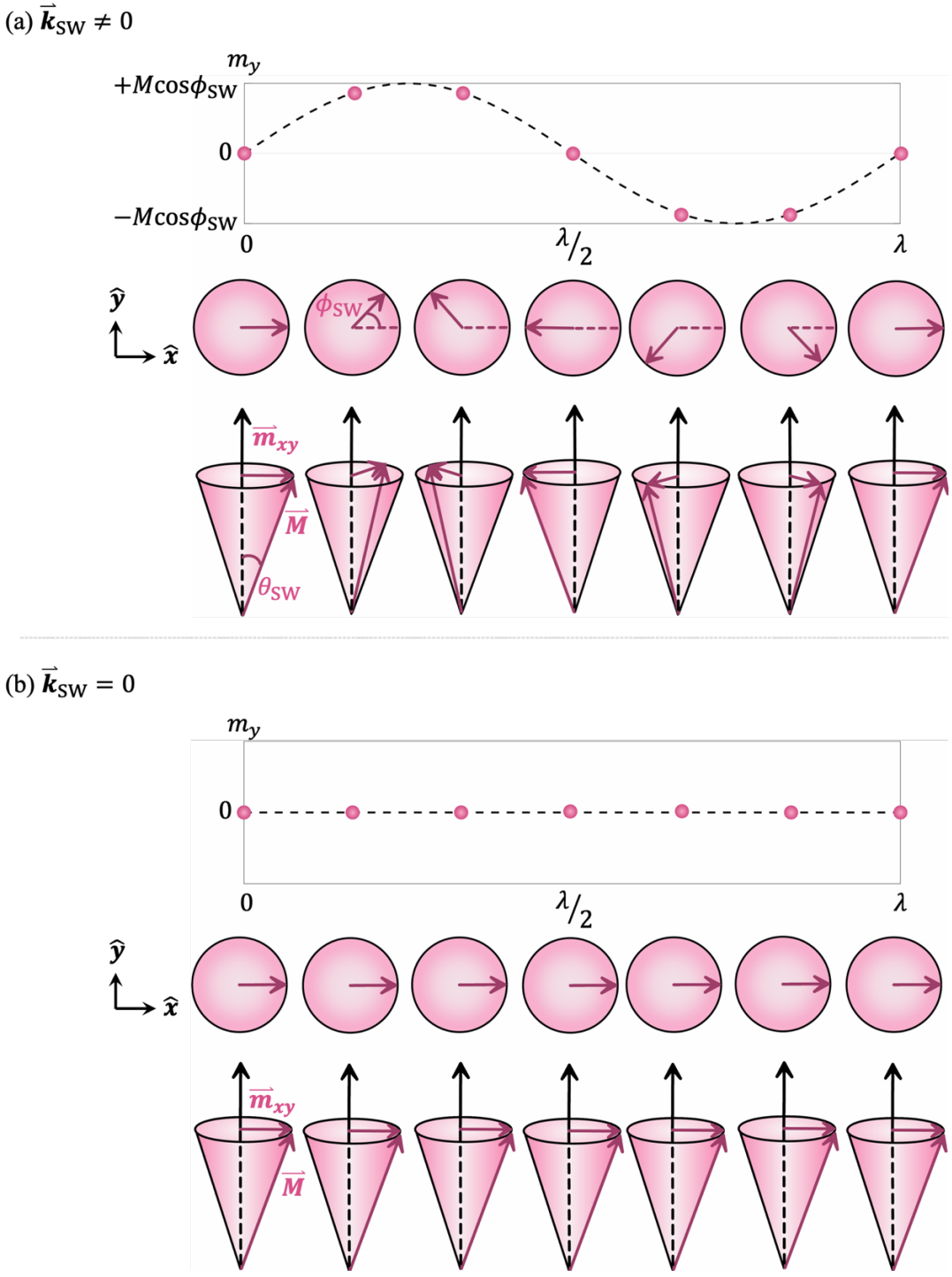

Figure 2.13. Schematics of spin wave traveling across the wavelength of spin wave, λ, for (a) the finite spin wavelength ($\vec{k}_{SW} \neq 0$) and (b) the infinitely long spin wavelength

($\vec{\boldsymbol{k}}_{\boldsymbol{SW}} = 0$). The top row shows m_y over the spin wavelength, the middle row shows m in $x - y$ plane, and the bottom row shows magnetization rotation as spin wave propagate over the length of λ.

In this thesis, the wavelength of spin waves is taken to be infinite, i.e. the dephasing between neighboring spins is neglected. In this infinitely long wavelength limit, all magnetic moments homogeneously precess in-phase at the same frequency. Hence, the long wavelength limit (spin wave vector $\vec{\boldsymbol{k}}_{\mathbf{SW}} = 0$) is often referred to as '*uniform mode*' or '*ferromagnetic resonance (FMR) mode*'. In this macro-spin approach, the magnetization dynamics is generally described by the Landau-Lifshitz-Gilbert (LLG) equation, which resembles the equation (1.19). The angular frequency of magnetization precession, ω_{M}, can be found by solving the LLG equation [51,52] given by

$$\frac{d}{dt}\vec{\boldsymbol{m}}(t) = -\gamma\left[\vec{\boldsymbol{m}}(t) \times \vec{\boldsymbol{H}}_{\mathbf{eff}}(t)\right] + \frac{\alpha}{M_{\mathrm{S}}}\left(\vec{\boldsymbol{m}}(t) \times \frac{d}{dt}\vec{\boldsymbol{m}}(t)\right), \tag{2.43}$$

where the magnetization $\vec{\boldsymbol{m}}(t) = \frac{\vec{\boldsymbol{M}}}{M}$, γ is the gyromagnetic ratio, and α is the Gilbert damping parameter. $\vec{\boldsymbol{H}}_{\mathbf{eff}}$ is the effective magnetic field which consists of a sum of all the magnetic field that affects the magnetization dynamics. Therefore, this term is closely related to the Gibbs free energy, G, in which it is expressed [53]

$$\vec{\boldsymbol{H}}_{\mathbf{eff}} = -\frac{\delta G}{\delta \vec{\boldsymbol{m}}} \equiv -\frac{\partial G}{\partial \vec{\boldsymbol{m}}} + \sum_{i}^{3} \frac{\partial}{\partial x_i}\left[\frac{\partial G}{\partial(\partial \vec{\boldsymbol{m}}/\partial x_i)}\right]. \tag{2.44}$$

Assuming that the magnetization distribution is spatially uniform, the above relationship can be written as

$$\mu_0 \vec{\boldsymbol{H}}_{\mathbf{eff}} = -\vec{\nabla}_{\mathbf{m}} G\,, \tag{2.45}$$

where ∇_{m} is the vector differential operator, where $-\vec{\nabla}_{\mathbf{m}} G = -\begin{pmatrix} \frac{\partial}{\partial m_1} G \\ \frac{\partial}{\partial m_2} G \\ \frac{\partial}{\partial m_3} G \end{pmatrix}$.

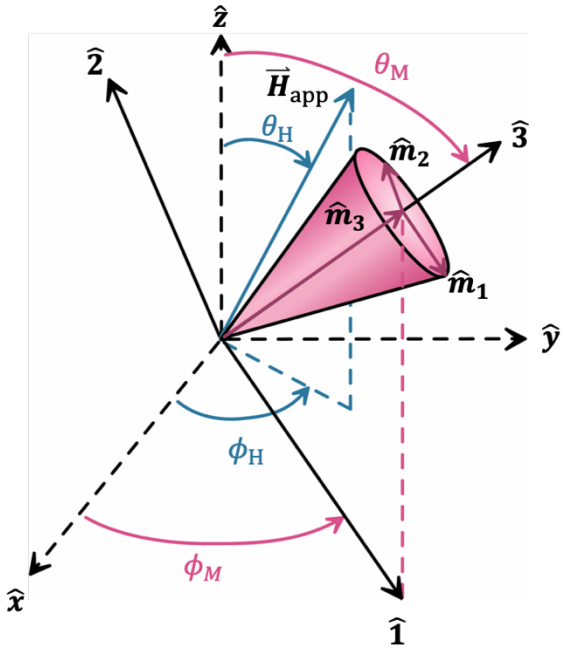

Figure 2.14. Schematics of coordinate transfer from the Cartesian (x, y, z) system to $(1, 2, 3)$ coordinate system.

In order to analyze the magnetization dynamics, it is more insightful to transform the coordinate system from the Cartesian system associated with the physical structure to the $(1, 2, 3)$ coordinate system as described in the figure 2.7 as this makes the mathematical calculation more convenient. In this newly defined $(1, 2, 3)$ coordinate system, $\widehat{\mathbf{3}}$ is defined to align with the direction of magnetization, $\vec{\mathbf{1}}$ and $\widehat{\mathbf{2}}$ lies in the $x - y$ plane, accordingly, the $\widehat{\mathbf{1}}$ points to the direction orthonormal to $\widehat{\mathbf{2}}$ and $\widehat{\mathbf{3}}$ axes. Adopting the coordinate transformation from cartesian coordinate system (x, y, z) to a coordinate system composed of $(1, 2, 3)$, where the cartesian coordinate rotates twice by azimuthal angle ϕ_{M} with respect to $\hat{z}$ axis, and polar angle θ_{M} with respect to $\hat{y}$ axis, the following transformation between the two coordinate systems applies.

$$\begin{pmatrix} x \\ y \\ z \end{pmatrix} = \widehat{\boldsymbol{U}} \begin{pmatrix} 1 \\ 2 \\ 3 \end{pmatrix},$$

$$\widehat{\boldsymbol{U}} = \begin{pmatrix} \cos\theta_{\mathrm{M}} \cos\phi_{\mathrm{M}} & -\sin\phi_{\mathrm{M}} & \sin\theta_{\mathrm{M}} \cos\phi_{\mathrm{M}} \\ \cos\theta_{\mathrm{M}} \sin\phi_{\mathrm{M}} & \cos\phi_{\mathrm{M}} & \sin\theta_{\mathrm{M}} \sin\phi_{\mathrm{M}} \\ -\sin\theta_{\mathrm{M}} & 0 & \cos\theta_{\mathrm{M}} \end{pmatrix}, \tag{2.46}$$

where θ_{M} is the azimuthal angle of magnetization measured from the surface normal to the plane of a film, and ϕ_{M} is the polar angle of magnetization measured anticlockwise from x-axis.

In the case of a poly-crystalline thin film, the exchange energy term associated with spin wavevector $(D_{\mathrm{S}} k_{\mathrm{SW}}^2)$ approaches zero because the film is approximated to be infinite along the in-plane direction and the spin wave vector k_{SW} vanishes. In this case,

the free energy is expressed by Zeeman energy and shape anisotropy energy. The Zeeman energy is generalized in the form of

$$G_{\text{Zeeman}} = -\overrightarrow{\boldsymbol{H}}_{\mathbf{app}} \cdot \overrightarrow{\boldsymbol{M}} = -M_{\text{S}}(H_1 m_1 + H_2 m_2 + H_3 m_3). \tag{2.47}$$

$\overrightarrow{\boldsymbol{H}}_{\mathbf{app}}$ in the (x, y, z) and $(1, 2, 3)$ coordinate system is related by

$$\overrightarrow{\boldsymbol{H}}_{\mathbf{app}}(x, y, z) = \begin{pmatrix} H_{\text{app}} \sin\theta_H \cos\phi_M \\ H_{\text{app}} \sin\theta_H \sin\phi_M \\ H_{\text{app}} \cos\theta_H \end{pmatrix},$$

$$\overrightarrow{\boldsymbol{H}}_{\mathbf{app}}(1, 2, 3) = \text{inv}\left(\widehat{\boldsymbol{U}}\right) \cdot \overrightarrow{\boldsymbol{H}}_{\mathbf{app}}(x, y, z). \tag{2.48}$$

Note that $\phi_M = \phi_H$ was approximated in poly-crystalline thin film because of the lack of in-plane symmetry.

$$G_{\text{Shape}} = \frac{1}{2} N_{\text{z}} (M_{\text{S}} m_{\text{z}})^2 = 2\pi M_{\text{S}}^2 (-\sin\theta_{\text{M}}\ m_1 + \cos\theta_{\text{M}}\, m_3)^2, \tag{2.49}$$

where $N_{\text{z}} = 4\pi$ is the demagnetization constant for thin film. Therefore, the total free energy of the thin film is generalized by

$$G = G_{\text{Zeeman}} + G_{\text{Shape}}$$
$$= -M_{\text{S}}(H_1 m_1 + H_2 m_2 + H_3 m_3) + 2\pi M_{\text{S}}^2 (-\sin\theta_{\text{M}}\ m_1 + \cos\theta_{\text{M}}\, m_3)^2. \tag{2.50}$$

where $\overrightarrow{\boldsymbol{H}}_{\mathbf{app}}$ is the externally applied magnetic field, and M_{s} is expressed in $[\text{emu/cm}^3]$, is the demagnetization associated with the shape anisotropy in a thin film.

Please note that in confined structures, such as magnetic nanoelements, non-uniform modes can be introduced, which requires inclusion of additional energy terms[54,55].

For the convenience of calculation, we can decompose the magnetization into two components as seen in the following expression.

$$\overrightarrow{\boldsymbol{m}}(t) = \overrightarrow{\boldsymbol{m}}_0 + \overrightarrow{\boldsymbol{m}}'(t) = \begin{pmatrix} 0 \\ 0 \\ 1 \end{pmatrix} + \begin{pmatrix} m_1(t) \\ m_2(t) \\ 0 \end{pmatrix}, \tag{2.51}$$

where $\overrightarrow{\boldsymbol{m}}_0$ denotes the magnetization at equilibrium position and $\overrightarrow{\boldsymbol{m}}'(t)$ denotes the small deviation around the equilibrium position to the first order. Note that m_3 is chosen to align with the direction of $\widehat{\mathbf{3}}$ axis, and $m_1(t)$ and $m_2(t)$ are chosen to be $m_i \ll 1$. In this new coordinate system, the equilibrium magnetization lies along the $\widehat{\mathbf{3}}$ axis, leaving the magnetization along the $\widehat{\mathbf{1}}$ and $\widehat{\mathbf{2}}$ axes precessing about the $\widehat{\mathbf{3}}$ axis.

This condition allows taking the Taylor expansion to the first order of $\overrightarrow{\boldsymbol{m}} \times \overrightarrow{\boldsymbol{H}}_{\mathbf{eff}}$ for small-angle precession of $m_1(t)$ and $m_2(t)$. The Taylor expansion is generalized in the form of

$$f(x) \cong f(x_0) + \left.\frac{df(x)}{dx}\right|_{x=x_0} (x - x_0) + \cdots . \tag{2.52}$$

The magnetization dynamics is simplified by taking the damping parameter to $\alpha = 0$ as we are interested in the resonance condition. The Landau-Lifshitz equation then becomes

$$\frac{1}{\gamma}\frac{d\overrightarrow{\boldsymbol{m}}}{dt} = -\overrightarrow{\boldsymbol{m}} \times \overrightarrow{\boldsymbol{H}}_{\mathbf{eff}}. \tag{2.53}$$

Substituting the generalized Taylor expansion with $f(x) \equiv -\vec{\boldsymbol{m}} \times \vec{\boldsymbol{H}}_{\mathbf{eff}}$, and $x \equiv \vec{\boldsymbol{m}}$,

$$-\left(\vec{\boldsymbol{m}} \times \vec{\boldsymbol{H}}_{\mathbf{eff}}\right) \cong -\vec{\boldsymbol{m}} \times \vec{\boldsymbol{H}}_{\mathbf{eff}}\big|_{\vec{\boldsymbol{m}}=\vec{\boldsymbol{m}}_0} - \frac{\partial}{\partial \vec{\boldsymbol{m}}}\left(\vec{\boldsymbol{m}} \times \vec{\boldsymbol{H}}_{\mathbf{eff}}\right)\Big|_{\vec{\boldsymbol{m}}=\vec{\boldsymbol{m}}_0} (\vec{\boldsymbol{m}} - \vec{\boldsymbol{m}}_0) + \cdots . \quad (2.54)$$

The 0^{th} order term vanishes by definition of equilibrium state because the magnetization resonates at a frequency to minimize the free energy and to compensate the $\vec{\boldsymbol{H}}_{\mathbf{eff}}$,

$$-\vec{\boldsymbol{m}} \times \vec{\boldsymbol{H}}_{\mathbf{eff}}\big|_{\mathrm{eq}} = \vec{\boldsymbol{m}} \times \left(\vec{\boldsymbol{\nabla}}_{\boldsymbol{m}} G\right)\big|_{\mathrm{eq}} = 0. \quad (2.55)$$

Therefore, the equation (2.54) simplifies to the 1^{st} order, written by

$$\left(\vec{\boldsymbol{m}} \times \vec{\boldsymbol{H}}_{\mathbf{eff}}\right) \cong \frac{\partial}{\partial \vec{\boldsymbol{m}}}\left(\vec{\boldsymbol{m}} \times \vec{\boldsymbol{H}}_{\mathbf{eff}}\right)\Big|_{\vec{\boldsymbol{m}}=\vec{\boldsymbol{m}}_0} \vec{\boldsymbol{m}}'. \quad (2.56)$$

where $\vec{\boldsymbol{m}}'$ is the small-angle deviation about the $\widehat{\mathbf{3}}$ axis, defined in equation (2.51), which has only $m_1(t) \cdot \widehat{\mathbf{1}}$ and $m_2(t) \cdot \widehat{\mathbf{2}}$ components, and $m_3 = 0$. Considering these two components, the first component of the torque term is approximated to

$$\left(\vec{\boldsymbol{m}} \times \vec{\boldsymbol{H}}_{\mathbf{eff}}\right) \cdot \widehat{\mathbf{1}}$$

$$\cong \left\{\frac{\partial}{\partial m_1}\left[\left(\vec{\boldsymbol{m}} \times \vec{\boldsymbol{H}}_{\mathbf{eff}}\right) \cdot \widehat{\mathbf{1}}\right]\right\}\Big|_{\vec{\boldsymbol{m}}=\vec{\boldsymbol{m}}_0} \cdot m_1(t) + \left\{\frac{\partial}{\partial m_2}\left[\left(\vec{\boldsymbol{m}} \times \vec{\boldsymbol{H}}_{\mathbf{eff}}\right) \cdot \widehat{\mathbf{1}}\right]\right\}\Big|_{\vec{\boldsymbol{m}}=\vec{\boldsymbol{m}}_0} \cdot m_2(t),$$

$$= \left\{\frac{\partial}{\partial m_1}\left[-m_2 \frac{\partial G}{\partial m_3} + m_3 \frac{\partial G}{\partial m_2}\right]\right\}\Big|_{\vec{\boldsymbol{m}}=\vec{\boldsymbol{m}}_0} \cdot m_1(t)$$

$$+ \left\{\frac{\partial}{\partial m_2}\left[-m_2 \frac{\partial G}{\partial m_3} + m_3 \frac{\partial G}{\partial m_2}\right]\right\}\Big|_{\vec{\boldsymbol{m}}=\vec{\boldsymbol{m}}_0} \cdot m_2(t),$$

$$= \left[-m_2 \frac{\partial^2 G}{\partial m_1 \partial m_3} + m_3 \frac{\partial^2 G}{\partial m_1 \partial m_2}\right]\Big|_{\vec{\boldsymbol{m}}=\vec{\boldsymbol{m}}_0} \cdot m_1(t)$$

$$+\left[-\frac{\partial G}{\partial m_3}-m_2\frac{\partial^2 G}{\partial m_2\partial m_3}+m_3\frac{\partial^2 G}{\partial m_2\partial m_2}\right]\Bigg|_{\vec{\boldsymbol{m}}=\vec{\boldsymbol{m}}_0}\cdot m_2(t),$$

$$=\frac{\partial^2 G}{\partial m_1\partial m_2}\cdot m_1(t)-\frac{\partial G}{\partial m_3}\cdot m_2(t)+\frac{\partial^2 G}{\partial m_2\partial m_2}\cdot m_2(t),$$

$$=G_{12}m_1(t)-G_3m_2(t)+G_{22}m_2(t). \tag{2.57}$$

For convenience in notation, we define $G_{ij}=\frac{\partial^2 G}{\partial m_i\partial m_j}\Big|_{\vec{\boldsymbol{m}}=\vec{\boldsymbol{m}}_0}$. Note that $\vec{\boldsymbol{H}}_{\mathbf{eff}}=-\vec{\boldsymbol{\nabla}}_{\mathbf{m}}G$ was taken and $m_{1,2}=0$ and $m_3=1$ at the equilibrium state was applied in the above equation. Likewise, the second component is approximated to

$$\left(\vec{\boldsymbol{m}}\times\vec{\boldsymbol{H}}_{\mathbf{eff}}\right)\cdot\hat{\mathbf{2}}$$

$$\cong\left\{\frac{\partial}{\partial m_1}\left[\left(\vec{\boldsymbol{m}}\times\vec{\boldsymbol{H}}_{\mathbf{eff}}\right)\cdot\hat{\mathbf{2}}\right]\right\}\Big|_{\vec{\boldsymbol{m}}=\vec{\boldsymbol{m}}_0}\cdot m_1(t)+\left\{\frac{\partial}{\partial m_2}\left[\left(\vec{\boldsymbol{m}}\times\vec{\boldsymbol{H}}_{\mathbf{eff}}\right)\cdot\hat{\mathbf{2}}\right]\right\}\Big|_{\vec{\boldsymbol{m}}=\vec{\boldsymbol{m}}_0}\cdot m_2(t),$$

$$=-\frac{\partial^2 G}{\partial m_1\partial m_1}\cdot m_1(t)+\frac{\partial G}{\partial m_3}\cdot m_1(t)-\frac{\partial^2 G}{\partial m_2\partial m_1}\cdot m_2(t),$$

$$=-G_{11}m_1(t)+G_3m_1(t)-G_{21}m_2(t). \tag{2.58}$$

Using this notation, the equation (2.57) and (2.58) becomes

$$\left(\vec{\boldsymbol{m}}\times\vec{\boldsymbol{H}}_{\mathbf{eff}}\right)=\begin{pmatrix}G_{12} & G_{22}-G_3\\ -G_{11}+G_3 & -G_{21}\end{pmatrix}\begin{pmatrix}m_1(t)\\ m_2(t)\end{pmatrix}. \tag{2.59}$$

For a small angle deviation near equilibrium, the magnetization behaves like a harmonic oscillation[56]. Now, we take an ansatz for a small oscillation near equilibrium, $\vec{\boldsymbol{m}}'(t)=\begin{pmatrix}m_1(t)\\ m_2(t)\end{pmatrix}\equiv\begin{pmatrix}m_1e^{i(-\omega_{\mathrm{M}}t)}\\ m_2e^{i(-\omega_{\mathrm{M}}t)}\end{pmatrix}$, and plugging the equation (2.59) into the LL equation (2.53) gives,

$$LHS) = -\frac{i\omega_{\mathrm{M}}}{\gamma}\begin{pmatrix} m_1(t) \\ m_2(t) \end{pmatrix},$$

$$RHS) = -\begin{pmatrix} G_{12} & G_{22} - G_3 \\ -G_{11} + G_3 & -G_{21} \end{pmatrix}\begin{pmatrix} m_1(t) \\ m_2(t) \end{pmatrix}. \tag{2.60}$$

Finally, organizing with the like-terms,

$$\begin{pmatrix} G_{12} - \frac{i\omega_{\mathrm{M}}}{\gamma} & G_{22} - G_3 \\ G_{11} - G_3 & G_{21} + \frac{i\omega_{\mathrm{M}}}{\gamma} \end{pmatrix}\begin{pmatrix} m_1(t) \\ m_2(t) \end{pmatrix} = 0\,. \tag{2.61}$$

The magnetization precession frequency is found by taking the determinant of the equation (1.7) to 0,

$$\left(\frac{\omega_{\mathrm{M}}}{\gamma}\right)^2 = (G_{22} - G_3)(G_{11} - G_3) - {G_{12}}^2\,. \tag{2.62}$$

where $G_{11} = 4\pi M_{\mathrm{s}}(\sin\theta_{\mathrm{M}})^2$, $G_{12} = G_{21} = 0$, $G_{22} = 0$, $G_3 = -H_{\mathrm{app}}\cos(\theta_{\mathrm{H}} - \theta_{\mathrm{M}}) + 4\pi M_{\mathrm{s}}(\cos\theta_{\mathrm{M}})^2$. With this given, the equation (2.62) is given by

$$\omega_{\mathrm{M}} = \gamma\sqrt{\left[H_{\mathrm{app}}\cos(\theta_{\mathrm{H}} - \theta_{\mathrm{M}}) - 4\pi M_{\mathrm{S}}\cos(2\theta_{\mathrm{M}})\right]} \tag{2.63}$$

$$\times\sqrt{\left[H_{\mathrm{app}}\cos(\theta_{\mathrm{H}} - \theta_{\mathrm{M}}) - 4\pi M_{\mathrm{S}}\cos(\theta_{\mathrm{M}}^2)\right]}$$

This formula is often called *Kittel frequency* or *uniform FMR mode*, where $\vec{\boldsymbol{k}}_{\mathbf{SW}} = 0$.

Now, the polar magnetization angle, θ_{M} aligns to minimize the total energy in the magnetic system at equilibrium state. Previously, the free energy was generalized to $m_1,\ m_2$, and m_3 to accommodate the approximation which involved partial derivative

of free energy over m_1, m_2, and m_3. The free energy also can be examined at equilibrium state, by inserting the equilibrium condition of $m_{1,2} = 0$ and $m_3 = 1$ is applied to equation (2.50), the equilibrium energy is given by

$$G_{\text{Zeeman}} = -M_s H_{\text{app}} \cos(\theta_H - \theta_M),$$

$$G_{\text{Shape}} = 2\pi M_S^2 (\cos\theta_M)^2,$$

$$G = -M_s H_{\text{app}} \cos(\theta_H - \theta_M) + 2\pi M_S^2 (\cos\theta_M)^2. \quad (2.64)$$

Therefore, the polar magnetization angle θ_M is found at the minimum energy,

$$\frac{\partial G}{\partial \theta_M} = -2\pi M_S^2 \sin(2\theta_M) - M_S H_{\text{app}} \sin(\theta_H - \theta_M) = 0. \quad (2.65)$$

3. Experimental Methods for Magnetoelastically Coupled Dynamics

3.1. FMR Technique

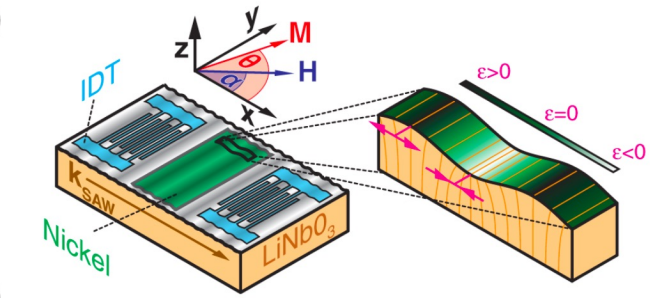

Figure 3.1. Schematics of SAW-driven FMR measurement showing the coordinate system. SAWs interact with a Ni thin film located between the two IDTs as they travel along the $LiNbO_3$ piezoelectric film. SAWs are detected at the IDT on the opposite side of the device. The magnetization of the Ni film is denoted as $\boldsymbol{M}$, and the externally applied magnetic field is denoted as $\boldsymbol{H}$. The figure on the right shows the strain applied to the Ni thin film due to interaction with SAWs. [30]

Magnetoelastic coupling introduces a time-dependent component to the effective applied field $H_{\text{eff}}(t)$ in the Landau-Lifhshitz-Gilbert equation (2.43). There are a couple of ways to experimentally measure the resulting magnetization dynamics.

Surface acoustic wave (SAW)-driven ferromagnetic resonance (FMR) is one of the most popular techniques for measuring magnetization dynamics as it is a non-destructive method which does not damage the sample upon measurement.[30,31,37,40,57–61] It is composed of two interdigitated transducers (IDTs) that generate and receive signals. A piezoelectric substrate is used as a medium for SAWs to propagate from the generator IDT through the magnetic element to the receiver IDT. In this technique, the SAW is used as an excitation tool to initiate and detect the magnetization dynamics. SAW is the mechanical wave that travels along the piezoelectric substrate material at a speed of sound wave (typically in the range of $v_{\mathrm{SAW}} \sim 4000\,\mathrm{m/s}$ for lithium niobate substrate, for Rayleigh SAW). As depicted in figure 3.1, the RF strain, ε is applied on the surface of the piezoelectric substrate. The wavelength of the SAW λ_{SAW} is determined by the spacing of the IDTs fingers, and the frequency of SAW is given by

$$f_{\mathrm{SAW}} = \frac{v_{\mathrm{SAW}}}{\lambda_{\mathrm{SAW}}}\,. \tag{3.1}$$

Figure 3.1a shows schematics of SAW-driven FMR measurement taken from one of the early works done by Weiler et. al.[30] Both IDTs and magnetic element are fabricated on the piezoelectric substrate to effectively deliver the strain waves.

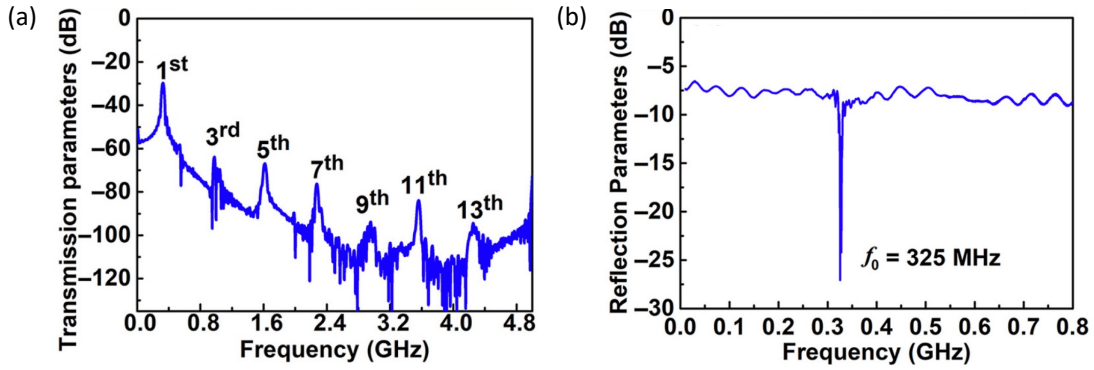

Figure 3.2. (a) Transmission spectra $|S_{21}|$ of higher harmonics of SAW frequencies. (b) Reflection spectra at $H_{app} = 1\ kOe$ at $\alpha = 60°$. [61]

Upon application of V_{RF} on the first IDT, the deformation on the piezoelectric substrate is induced by the inverse piezoelectric effect. After the SAWs undergo magnetoelastic coupling and interplay between the phonon and magnon, the voltage induced by the piezoelectric effect on the substrate is measured at the receiver IDT. The transmission spectra S_{21}, $|S_{21}|$, or $|S_{21}|^2$ are commonly used to plot the RF pump frequency dependent FMR response. In figure 3.2a, S_{21} was used to display the frequency response of SAW without external magnetic field applied. In this case, multiple distinct peaks show up in the transmission spectra indicating the higher-order harmonics of SAW frequencies, where the fundamental frequency is determined by the equation (3.1). The transmission spectra are obtained while sweeping the DC externally applied magnetic field at $H_{\mathrm{app}} \leq |H_{\mathrm{app,max}}|$, while sweeping the RF frequency at each applied magnetic field. When the frequency of the external magnetic field matches the resonant frequency of the magnetic moments (f_0), a sharp absorption peak (reflection dip) is observed in the spectra (Fig. 3.2b).

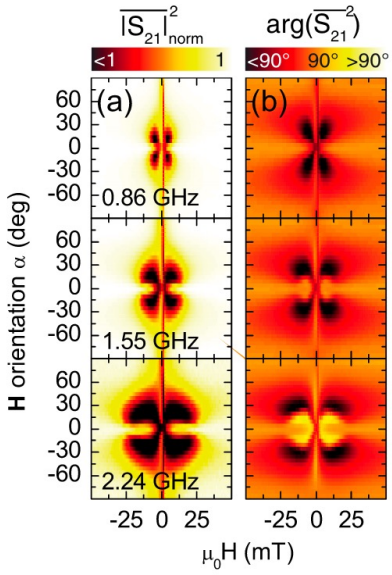

Figure 3.3. (a) Normalized transmission spectra ($|S_{21}|_{norm}{}^2$) and (b) their signal phase spectra ($arg(|S_{21}|^2)$) at various magnetic field (H_{app}) and in-plane orientation α of applied external magnetic field – see the system in figure 3.1 [30].

In this configuration, orientation of applied magnetic field can be applied along the various angles, denoted as α. Near the magnetic resonance frequency ($f_0 = 2.4$ GHz in the figure 3.3a), a noticeable attenuation of the SAW transmission (dark color in the spectra) is observed. This is because the absorption of the SAW in the magnetic film is increased due to magnetoelastic coupling. Additionally, figure 3.3 clearly suggests fourfold angular symmetry, which is the characteristics of SAW-driven FMR. As depicted in the transmission spectra, the strength of magnetoelastic coupling depends on the in-plane orientation of applied magnetic field. Moreover, various types of acoustic waves demonstrate distinct symmetries, influenced by the polarization of

SAWs[62]. This is due to the fact that longitudinal and shear acoustic waves feature different dominant strain elements.

To improve the SAW transmission signal, time gating with Fourier transformation technique is often used to remove the primary SAW signals contributing to spurious reflections or electromagnetic crosstalk.[63]

3.2. Optical Methods

Another method of detecting the hybrid dynamics of magnon and phonon coupling is to use the time-resolved magneto-optic Kerr effect (TR-MOKE) in polar configuration. Dual-color pump–probe microscopy using TR-MOKE is a mainstay for the study of magnetization dynamics and offers excellent temporal (femtosecond) and spatial (sub-micron) resolution while requiring little to no additional sample fabrication and preparation.

Before delving into the TR-MOKE technique, let us start by understanding what happens in the magnetic specimen when excited by laser pulses. According to the three-temperature model (3TM), upon excitation of the laser pulses, the femtosecond pulse energy transfers to the electron system. As the electron system reaches the equilibrium states, the heat in the electron system dissipates to both phonons and spins. Thus, the laser pulse acts as a thermal perturbation in the spin system.

3.2.1. Weiss Mean Field Theory (Molecular Field Theory) and Laser Pulses

As we focus on ferromagnetic resonance in this thesis, we introduce the Weiss mean field (molecular field) theory, which is the first theory accounting for the mechanism of spontaneous magnetization proposed by Pierre Weiss in 1907[64]. In this theory, the magnetic field seen by one spin due to interaction of neighboring spins are defined as molecular field, $n_{\mathrm{W}}\vec{\boldsymbol{M}}$, where n_{W} is the Weiss coefficient. When an external magnetic field is applied, effective magnetic field seen by one spin, $\vec{\boldsymbol{H}}_{\boldsymbol{i}}$, is expressed by

$$\vec{\boldsymbol{H}}_{\boldsymbol{i}} = n_W\vec{\boldsymbol{M}} + \vec{\boldsymbol{H}}_{\mathrm{app}}. \tag{3.2}$$

The thermodynamic average value of magnetic moment is expressed by

$$\langle\vec{\boldsymbol{\mu}}_{\mathbf{Z}}\rangle = |\vec{\boldsymbol{\mu}}_{\mathbf{0}}|\left[\frac{2J+1}{2J}\coth\frac{2J+1}{2J}x - \frac{1}{2J}\coth\frac{x}{2J}\right], \tag{3.3}$$

where $|\vec{\boldsymbol{\mu}}_{\mathbf{0}}| = g|\mu_{\mathrm{B}}|J$, and the Brillouin function $B_J(x) = \frac{2J+1}{2J}\coth\frac{2J+1}{2J}x - \frac{1}{2J}\coth\frac{x}{2J}$, with $x = \mu_0|\vec{\boldsymbol{\mu}}_{\mathbf{0}}|\left(n_W M + H_{\mathrm{app}}\right)/k_B T$. The maximum magnetization is given by $M_0 = n|\vec{\boldsymbol{\mu}}_{\mathbf{0}}| = ng\mu_B J$, where $n = N/V$. Writing the equation (3.3) in terms of magnetization,

$$M = M_0 B_{\mathrm{J}}(x). \tag{3.4}$$

Without the presence of external magnetic field, H_{app}, M becomes spontaneous magnetization, I_{S}. The Brillouin function is now written in terms of spontaneous magnetization,

$$\frac{I_S}{M_0} = B_J(x_0), \tag{3.5}$$

where $x_0 = \mu_0|\vec{\boldsymbol{\mu}}_0|(n_W M)/k_B T$. Using the relationship of Curie constant, $C = \mu_0 n|\vec{\boldsymbol{\mu}}_{\text{eff}}|^2/3k_B$, where $|\vec{\boldsymbol{\mu}}_{\text{eff}}| = g|\mu_B|\sqrt{J(J+1)}$, equation (3.5) is written by

$$\frac{I_S}{M_0} = [T(J+1)/3JCn_W]x_0. \tag{3.6}$$

The temperature-dependent $\frac{I_S}{M_0}$ is plotted in figure 3.4a, showing the magnetization property of ferromagnet vanishes at the critical temperature, T_C.

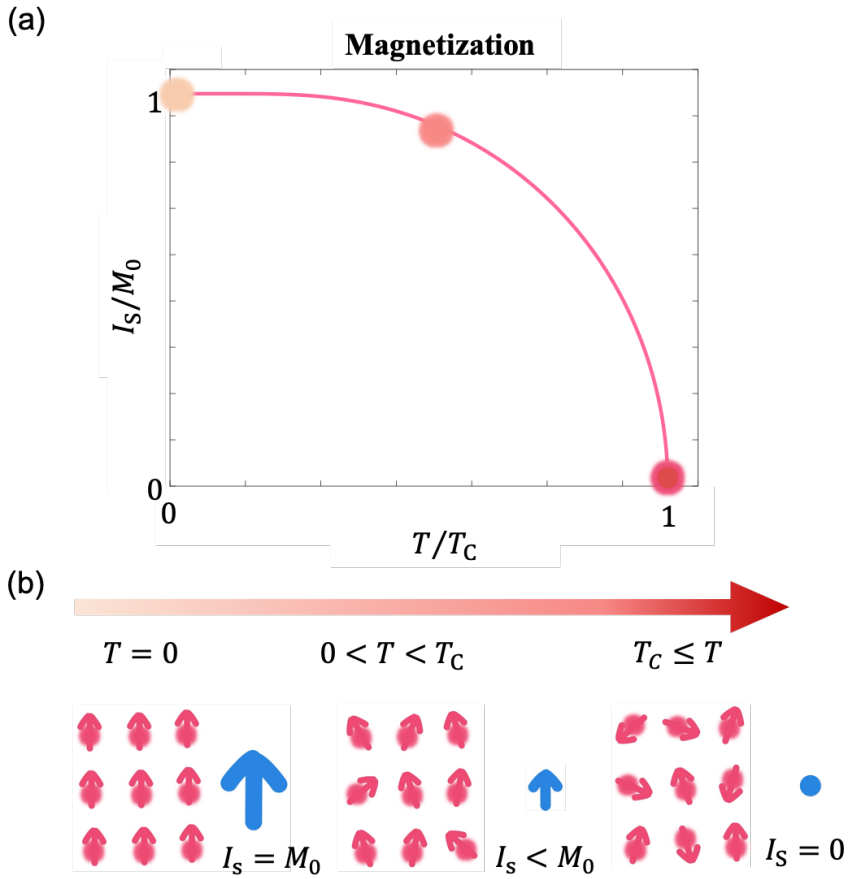

Figure 3.4. Spontaneous magnetization response at different temperatures. (a) Spontaneous magnetization over the maximum magnetization calculated using the Weiss mean field introduced in equation (3.6). The circles corresponds to the 3 different

temperatures at $T = 0$, $0 \ll T < T_C$, and $T_C < T$. (b) Schematics of spontaneous magnetization response upon introduction of heat in the ferromagnetic system. As the temperature increases, randomization in the spin orientation is introduced, leading to a lower magnetization in the system. At the critical temperature, the magnetization vanishes as more random orientation of spin is introduced, which averages out to zero magnetization. The blue arrows are the net spontaneous magnetization in the ferromagnet, and the pink arrows are the spins at each electron cites.

3.2.2. Magnetization Dynamics upon Femtosecond Laser Pulse Excitation

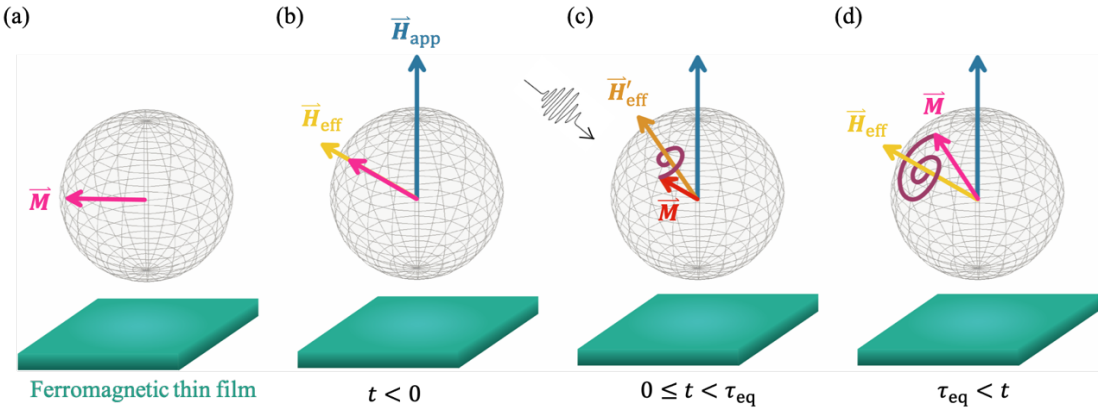

Figure 3.5. Schematics of magnetization dynamics upon excitation of femtosecond laser pulses. (a) Magnetization before the application of external magnetic field, $\vec{H}_{app}$. The magnetization direction lies along the magnetic easy-axis, which is in the in-plane direction for an arbitrary poly-crystalline thin film in this example. (b) Magnetization points along the $\vec{H}_{eff}$ with the presence of $\vec{H}_{app}$ before the irradiation of laser pulses.

(c) Upon excitation of laser pulses, the heat is introduced in the spin system resulting in the reduced magnetization. Consequently, the magnetization precess about the new effective magnetic field $\overrightarrow{\boldsymbol{H}}'_{\boldsymbol{eff}}$. (d) After the spin system cools down, the magnetization recovers its original states, thus the effective magnetic field points at the initial orientation as shown in (b). $\overrightarrow{\boldsymbol{H}}_{\boldsymbol{eff}}$ acts as a torque to the magnetization, resulting in the precession about the axis of $\overrightarrow{\boldsymbol{H}}_{\boldsymbol{eff}}$.

The magnetization dynamics is initiated when sufficiently large external field is applied angled away from the equilibrium magnetization direction (easy-axis). Before the excitation of laser pulses, the equilibrium direction of magnetization points along the effective magnetic field $\overrightarrow{\boldsymbol{H}}_{\mathbf{eff}}$ defined in equation (2.45). When the laser pulse introduce heat in the magnetic system, the spontaneous magnetization reduces due to thermal effect. As a result, the internal magnetization is reduced (demagnetized), changing the effective magnetic field to a new vector, $\overrightarrow{\boldsymbol{H}}'_{\mathbf{eff}}$, where the direction and magnitudes are both changed. Due to the timescale in thermal exchange between the electron-lattice-spin reservoirs is faster than the timescale of magnetization precession, the magnetization cannot be aligned to $\overrightarrow{\boldsymbol{H}}'_{\mathbf{eff}}$ immediately. Thus, the new effective magnetic field is applied canted away from the magnetization direction, acting as a torque for the reduced magnetization to providing the precessional motion about the axis of $\overrightarrow{\boldsymbol{H}}'_{\mathbf{eff}}$. After the spins in the ferromagnet dissipate heat to the background within τ_{eq}, the reduced magnetization recovers to its initial magnetization as the temperature cools

down. In return, the effective magnetic field recovers back the initial $\vec{\boldsymbol{H}}_{\mathbf{eff}}$, leaving the magnetization canted away from $\vec{\boldsymbol{H}}_{\mathbf{eff}}$. Therefore, the recovered magnetization precess about $\vec{\boldsymbol{H}}_{\mathbf{eff}}$, due to the torque provided by $\vec{\boldsymbol{H}}_{\mathbf{eff}}$.

3.2.3 Magneto-Optic Kerr Effect (MOKE)

Magnetic materials possess different index of refraction for right circularly polarized light (RCP) and left circularly polarized light (LCP) due to their circular magnetic dichroism. Note that it is completely different concept than the electro-optic Kerr Effect. Magneto-optic Kerr Effect (MOKE) is observed when linearly polarized light is reflected at the surface of magnetic specimen.

According to Lorentz's atomic model of dispersion, the electrons are bound to their equilibrium position following the harmonic oscillation model with friction, $\gamma\dot{\vec{\boldsymbol{r}}}$. With the presence of electric field $\vec{\boldsymbol{E}} = \vec{\boldsymbol{E}}_{\boldsymbol{0}} e^{i(\omega t - gz)}$, where $\vec{\boldsymbol{E}}_{\boldsymbol{0}} = E_x \hat{\boldsymbol{e}}_{\boldsymbol{x}} + E_y \hat{\boldsymbol{e}}_{\boldsymbol{y}}$, and an externally applied static magnetic field, $\vec{\boldsymbol{B}} = B\hat{\boldsymbol{e}}_{\boldsymbol{z}}$, the equation of motion of the electrons are written as

$$\ddot{\vec{\boldsymbol{r}}} + \gamma\dot{\vec{\boldsymbol{r}}} + \omega_0^2\vec{\boldsymbol{r}} = \frac{e}{m}\vec{\boldsymbol{E}}_{\boldsymbol{0}} e^{i(\omega t - gz)} + \frac{e}{mc}\dot{\vec{\boldsymbol{r}}} \times \vec{\boldsymbol{B}}, \tag{3.7}$$

where $\vec{g} = g\hat{\boldsymbol{e}}_{\boldsymbol{z}}$ is the wave vector.

Transforming the cartesian coordinate into the circular coordinate system, ($\hat{\boldsymbol{e}}_{+}$, $\hat{\boldsymbol{e}}_{-}$, $\hat{\boldsymbol{e}}_{\boldsymbol{z}}$), where $\hat{\boldsymbol{e}}_{+} = \frac{1}{\sqrt{2}}\left(\hat{\boldsymbol{e}}_{\boldsymbol{x}} + i\hat{\boldsymbol{e}}_{\boldsymbol{y}}\right)$ and $\hat{\boldsymbol{e}}_{-} = \frac{1}{\sqrt{2}}\left(\hat{\boldsymbol{e}}_{\boldsymbol{x}} - i\hat{\boldsymbol{e}}_{\boldsymbol{y}}\right)$, and using the relationship of the total polarization to the electric field, $\vec{\boldsymbol{P}}_{\pm} = Ne\vec{\boldsymbol{r}}_{\pm} = \tilde{\alpha}_{\pm}\,\vec{\boldsymbol{E}}_{\pm}$, where $\tilde{\alpha}_{\pm}$ is the

polarizability, and N is the number electrons per unit volume, the complex dielectric function is written by

$$\tilde{\varepsilon}_{\pm} = 1 + 4\pi\tilde{\alpha}_{\pm} = \tilde{\varepsilon}_{1\pm} - i\tilde{\varepsilon}_{2\pm}, \tag{3.8}$$

$$\tilde{\varepsilon}_{1\pm} = 1 + \frac{4\pi Ne^2}{m}\frac{\omega_0^2 - \omega^2 \pm \omega\omega_{\mathrm{C}}}{(\omega_0^2 - \omega^2 \pm \omega\omega_{\mathrm{C}})^2 + (\omega\gamma)^2},$$

$$\tilde{\varepsilon}_{2\pm} = \frac{4\pi Ne^2}{m}\frac{\omega\gamma}{(\omega_0^2 - \omega^2 \pm \omega\omega_{\mathrm{C}})^2 + (\omega\gamma)^2},$$

where $\tilde{\varepsilon}_{1\pm}$ and $\tilde{\varepsilon}_{2\pm}$ are the real and imaginary part of $\tilde{\varepsilon}_{\pm}$, respectively with + and – signs denoting the RCP and LCP light. $\omega_0^2 = \frac{\hat{f}}{m}$ is the resonance frequency with Hook's law force constant $\hat{f}$, $\omega_{\mathrm{C}} = \frac{eB}{mc}$ is the cyclotron frequency.

With the presence of magnetic field or spontaneous magnetization, the complex dielectric tensor of the magnetic materials is given by

$$\tilde{\boldsymbol{\varepsilon}} = \begin{pmatrix} \tilde{\varepsilon}_{+} & 0 \\ 0 & \tilde{\varepsilon}_{-} \end{pmatrix}. \tag{3.9}$$

Taking the coordinate transformation from circular coordinate system to cartesian coordinate system, the anisotropic complex dielectric tensor is obtained by

$$\tilde{\boldsymbol{\varepsilon}} = \begin{pmatrix} \tilde{\varepsilon}_{xx} & \tilde{\varepsilon}_{xy} & 0 \\ -\tilde{\varepsilon}_{xy} & \tilde{\varepsilon}_{xx} & 0 \\ 0 & 0 & \tilde{\varepsilon}_{zz} \end{pmatrix}, \tag{3.10}$$

where $\tilde{\varepsilon}_{xx} = \frac{1}{2}(\tilde{\varepsilon}_{+} + \tilde{\varepsilon}_{-})$, and $\tilde{\varepsilon}_{\pm} = \tilde{\varepsilon}_{xx} + i\tilde{\varepsilon}_{xy}$.

As a result of complex dielectric function, the complex refractive index $\tilde{n}_{\pm}$ is defined by

$$\tilde{n}_{\pm} = (n_{\pm} - ik_{\pm}), \tag{3.11}$$

where $n_{\pm}$ and $k_{\pm}$ are the real part and imaginary part of the complex refractive index, respectively. Consequently, the complex reflection coefficient is given by

$$\tilde{r}_{\pm} = \frac{\tilde{n}_{\pm} - 1}{\tilde{n}_{\pm} + 1}. \tag{3.12}$$

Phenomenologically, the Kerr-effect involves the rotation of the major axis of rotation θ_{K} and ellipticity η_{K} of the reflected light, which is written by a complex Kerr rotation $\tilde{\theta}_{\mathrm{K}}$

$$\tilde{\theta}_{\mathrm{K}} = \theta_{\mathrm{K}} - i\eta_{\mathrm{K}}. \tag{3.13}$$

There are three possible MOKE configurations; polar, longitudinal, and transverse. In the polar configuration, the magnetization direction points to the normal direction (out-of-plane) of the magnetic specimen. When the magnetization points in-plane and parallel to the plane of incidence, the configuration is called the longitudinal configuration. If the magnetization points in-plane but perpendicular to the plane of incidence, then it is the transverse configuration. In this thesis, we discuss polar MOKE configuration.

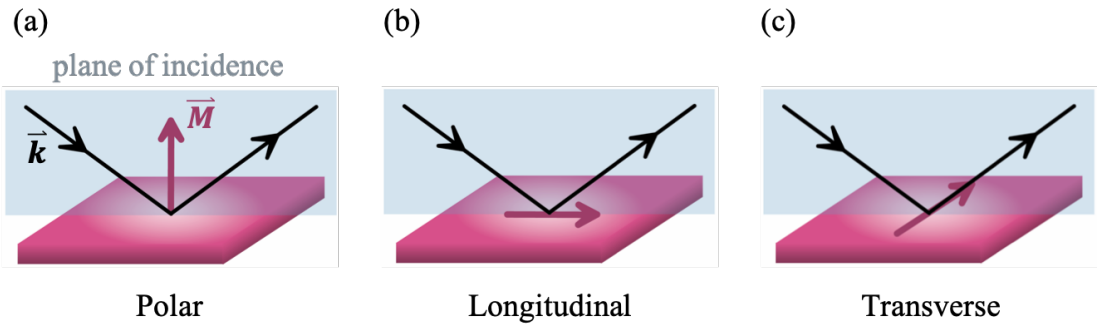

Figure 3.6. Schematics of (a) Polar, (b) longitudinal, and (c) transverse MOKE configurations.

In polar MOKE configuration, the Fresnel's formula for reflection at normal incident accounts for the Kerr-effect. Writing the complex reflection coefficient in polar coordinate, $\tilde{r}_{\pm} = r_{\pm}e^{i\phi_{\pm}}$, the complex Kerr rotation is given by

$$\tilde{\theta}_{\mathrm{K}} \equiv i\frac{\tilde{r}_{+} - \tilde{r}_{-}}{\tilde{r}_{+} + \tilde{r}_{-}}, \tag{3.14}$$

$$\theta_{\mathrm{K}} = -\frac{\phi_{+} - \phi_{-}}{2},$$

$$\tan\eta_{\mathrm{K}} = -\frac{r_{+} - r_{-}}{r_{+} + r_{-}}.$$

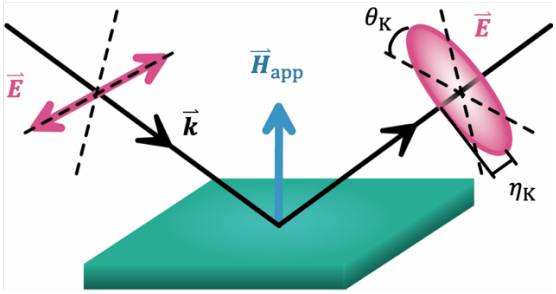

Figure 3.7. Schematics showing the magneto-optic Kerr effect upon reflection on the magnetic specimen, demonstrating the Kerr rotation and Kerr ellipticity.

Another way to express the magneto-optic Kerr effect is to use the magneto-optical constant Q, and the following derivation is reproduced based on the work of C.-Y. You and S.-C. Shin[65]. The complex dielectric tensor is given by

$$\varepsilon = \varepsilon_{xx}\begin{pmatrix} 1 & -iQm_z & iQm_y \\ iQm_z & 1 & -iQm_x \\ -iQm_y & iQm_x & 1 \end{pmatrix}, \tag{3.15}$$

where $Q = i\frac{\varepsilon_{xy}}{\varepsilon_{xx}}$. In polar MOKE configuration, $m_z = 1, m_x = m_y = 0$.

As the phenomenological magneto-optic Kerr effect can be explained by Fresnel reflection, the Fresnel reflection matrix associated with MOKE is found

$$\widehat{\Re} = \begin{pmatrix} r_{\mathrm{pp}} & r_{\mathrm{ps}} \\ r_{\mathrm{sp}} & r_{\mathrm{ss}} \end{pmatrix}, \tag{3.16}$$

where r_{ij} satisfies the relationship $\begin{pmatrix} \vec{E}_{\mathrm{s}}^{\mathrm{r}} \\ \vec{E}_{\mathrm{p}}^{\mathrm{r}} \end{pmatrix} = \begin{pmatrix} r_{\mathrm{pp}} & r_{\mathrm{ps}} \\ r_{\mathrm{sp}} & r_{\mathrm{ss}} \end{pmatrix} \begin{pmatrix} \vec{E}_{\mathrm{s}}^{\mathrm{i}} \\ \vec{E}_{\mathrm{p}}^{\mathrm{i}} \end{pmatrix}$ with s and p denotes the s-polarized light and p-polarized light, respectively. Considering a case where the light is incident from a non-magnetic medium with refractive index n_0 at an incident angle θ_0 to a magnetic medium with n_1, and θ_1 is the complex refractive angle in the magnetic medium. The elements of the Fresnel reflection matrix for the polar MOKE configuration is given by

$$r_{\mathrm{pp}} = \frac{n_1 \cos\theta_0 - n_0 \cos\theta_1}{n_1 \cos\theta_0 + n_0 \cos\theta_1},$$

$$r_{\mathrm{ss}} = \frac{n_0 \cos\theta_0 - n_1 \cos\theta_1}{n_0 \cos\theta_0 + n_1 \cos\theta_1},$$

$$r_{\mathrm{sp}} = i\frac{n_0 n_1 (\cos\theta_0)(\cos\theta_1) Q}{(n_1 \cos\theta_0 + n_0 \cos\theta_1)(n_0 \cos\theta_0 + n_1 \cos\theta_1)\cos\theta_1},$$

$$r_{\mathrm{ps}} = i\frac{n_0 n_1 (\cos\theta_0)(\cos\theta_1) Q}{(n_1 \cos\theta_0 + n_0 \cos\theta_1)(n_0 \cos\theta_0 + n_1 \cos\theta_1)\cos\theta_1}. \tag{3.17}$$

Using this relationship, the complex Kerr rotation is defined as

$$\tilde{\theta}_{\mathrm{K}}^{\mathrm{s}} = \theta_{\mathrm{K}}^{\mathrm{s}} - i\eta_{\mathrm{K}}^{\mathrm{s}} \equiv \frac{r_{\mathrm{ps}}}{r_{\mathrm{ss}}},$$

$$\tilde{\theta}_{\mathrm{K}}^{\mathrm{p}} = \theta_{\mathrm{K}}^{\mathrm{p}} - i\eta_{\mathrm{K}}^{\mathrm{p}} \equiv \frac{r_{\mathrm{sp}}}{r_{\mathrm{pp}}}. \tag{3.18}$$

3.2.4. Detection Mechanism with Balanced Photodetector (BPD)

To briefly explain it, the electric field is initially polarized by a polarizer and incident to the magnetic specimen. The reflected electric field passes through the second polarizer, called analyzer before collected at the photodetector. The intensity, $\boldsymbol{I}$, of the electric field collected at the photodetector provides information of the magnetization dynamics, which is given by

$$\boldsymbol{I} = \vec{\boldsymbol{E}}_{\mathbf{f}}\vec{\boldsymbol{E}}_{\mathbf{f}}^{*}, \tag{3.19}$$

where $\vec{\boldsymbol{E}}_{\mathbf{f}}$ denotes the final electric field after passed through the analyzer. By adapting Jones formalism, the intensity can be mathematically calculated. The following work is reproduced based on the work of B. Koopman[66]. Given that the angles of optical axes for polarizers and analyzers with respect to plane of incident are α_{P} and α_{A}, the final electric field is described by

$$\boldsymbol{I} = \vec{\boldsymbol{E}}_{\mathbf{f}}\vec{\boldsymbol{E}}_{\mathbf{f}}^{*} = \left|L(\alpha_{\mathrm{A}}) \cdot \hat{\Re} \cdot L(\alpha_{\mathrm{P}})\vec{\boldsymbol{E}}_{\boldsymbol{i}}\right|^{2}, \tag{3.20}$$

Where $\hat{\Re}$ is the reflection matrix found from equation (3.16), and $L\left(\alpha_{\mathrm{A,P}}\right)$ is the Jones formalism for a linear polarizer.

Assuming for the case of s-polarized electric field, $\alpha_{\mathrm{P}} = \frac{\pi}{2}$, and the polarizer and analyzer are almost crossed ($|\alpha_{\mathrm{A}}| \ll 1$), equation (3.20) to the second order yields

$$\boldsymbol{I} = \hat{\Re} \cdot (\alpha_{\mathrm{A}}^{2} + 2\alpha_{\mathrm{A}}\theta_{\mathrm{K}} + \theta_{\mathrm{K}}^{2} + \eta_{\mathrm{K}}^{2}). \tag{3.21}$$

Taking a partial derivative to find the transient intensity caused by the laser pump pulse (laser-induced), we find

$$\Delta\boldsymbol{I} = 2R_{0}\alpha_{\mathrm{A}}\Delta\theta_{\mathrm{K}}(t) + \alpha_{\mathrm{A}}^{2}\Delta R(t), \tag{3.22}$$

where the first term ($\Delta\theta_{\mathrm{K}}(t)$) shows the transient magneto-optical rotation, and the second term ($\Delta R(t)$) represents the transient reflection. In this MOKE detection, only the Kerr rotation is resolved (θ_{K}), however, the Kerr ellipticity (η_{K}) cannot be detected. In order to minimize the non-magnetic background signal ($\Delta R(t)$), α_{A} should be set nearly zero. Therefore, the non-magnetic background signal is always present in this configuration.

By substituting the analyzer to a Wollaston prism (polarizing beam splitter, PBS), the electric field is split into two orthogonal components where the two components are detected separately by the photodetectors. The two photodetectors are balanced when $\alpha_{\mathrm{A}} = \alpha_{\mathrm{PBS}} = 45^{\circ}$, where the signals from the two photodetectors are equal. In this case, the transient difference signal is measured by

$$\Delta I(t) = 2R_0\Delta\theta_{\mathrm{K}}(t) + 2\theta_0\Delta R(t). \tag{3.23}$$

In most cases, $\frac{\Delta R(t)}{R_0} \ll \frac{\Delta\theta(t)}{\theta_0}$, equation (3.23) yields,

$$\Delta I(t) = 2R_0\Delta\theta_{\mathrm{K}}(t). \tag{3.24}$$

Therefore, the $\Delta I(t)$ provide direct measurement of magnetic response in BPD configuration.

3.3. Time-Resolve MOKE Setup for Simultaneous Detection of Magnon and Phonon Dynamics

The time-resolved magneto-optic Kerr effect (TR-MOKE) in polar configuration setup used in this thesis is described in figure 3.8. With the application of balanced

photodetector (BPD) instead of using an analyzer, TR-MOKE provides simultaneous detection of magnon and phonon dynamics separately, making it a powerful tool for studying the hybrid magnon-phonon dynamics. It is an all-optical method that measures the change in magnetization in the time domain using a polarized laser pulse that is reflected from the magnetic sample plane via the magneto-optic Kerr effect. One of the advantages of TR-MOKE is that it requires minimal to no sample preparation for a measurement. On top of this, it provides great spatial (sub-micrometer) and time (femtosecond) resolution.

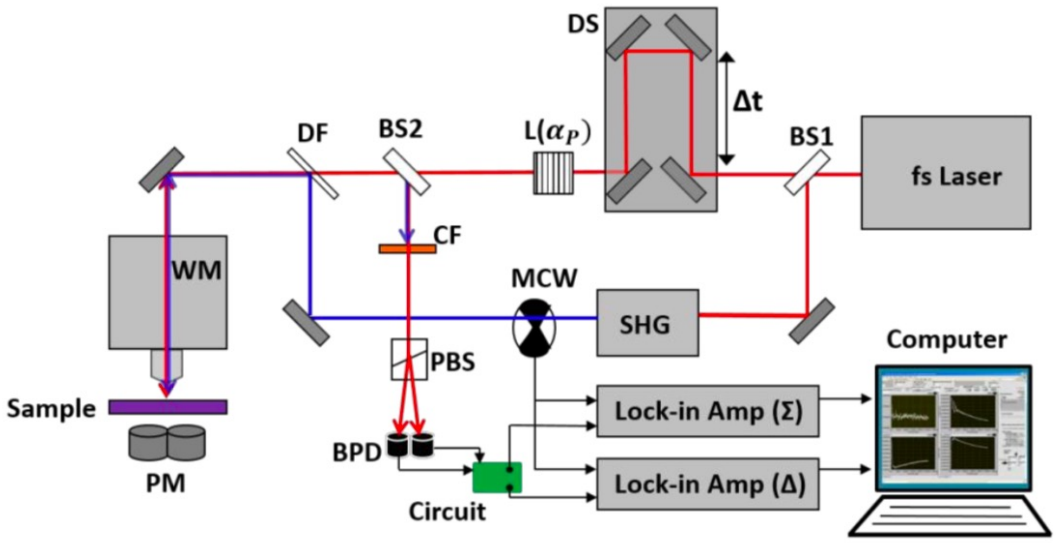

Figure 3.8. Schematics of TR-MOKE setup with BPD configuration.[32] The pump beam path is highlighted with blue line and the probe beam path is highlighted with red line. See main text for detail. BS: beam splitter, SHG: second-harmonic generator, MCW: mechanical chopper wheel, DF: dichroic filter, DS: delay stage, L(α_P): linear polarizer, WM: WiTec microscope, PM: permanent magnets, CF: color filter, PBS: polarized beam splitter, BPD: balanced photodetector.

In realizing time-resolved optical study, two-color pump and probe laser pulses are introduced. At the beginning of the beam path, the laser pulse is split at the beam splitter (BS) into two different beam paths. The stronger beam undergoes frequency doubling at the second-harmonic generator (SHG), and it arrives at the magnetic sample plane under the WiTec microscope objective (WM). This beam is often called as a pump beam because it arrives at the magnetic sample earlier than the probe beam $(\mathrm{t} = 0)$, initiating (pumping up the energy level from the equilibrium state) the magnetization dynamics. The weaker beam is then steered to add beam path on the motorized delay stage (DS). The delay stage controls the length of the beam path of the probe beam to ensure that the probe beam arrives after the pump beam $(\mathrm{t} = \Delta t)$. Once the pump beam is delayed by additional beam path, it passes a linear polarizer $(\mathrm{L}(\alpha_{\mathrm{P}}))$ before merging with the pump beam path at the dichroic filter (DF) and enters the WiTec microscope objective lens. Then the polarized probe beam undergoes Kerr rotation upon reflection on the magnetic material. Both of the beams are reflected back through the same objective lens. However, the pump beam is removed using a spectral filter (CF). The probe beam alone is now going through the polarizing beam splitter (PBS) to separate the horizontal and vertical components to be collected separately by the two balanced photodetectors. The sum of both signals obtained from the two photodetectors provides information of change in reflection (phononic dynamics), while the difference of the two signals provides information of change in magnetization (magnonic dynamics). The difference signal is balanced before the onset of the pump beam by evenly distributing the horizontal and vertical components to the two photodetectors. Upon

initiation of the magnetization dynamics, the polarization of the probe beam starts deviating from the initially balanced polarization due to the Kerr rotation. This unbalances the amplitudes of signal at the two photodetectors allowing us to detect the magnetization precession via the difference channel. On the other hand, the sum channel adds the signal detected at the two photodetectors, leaving the sum channel unaffected by the magnetization dynamics. However, when the phononic dynamics is initiated by the thermal expansion or vibration, the sum channel displays such change in the reflectivity. This change in reflectivity is equally detected at the horizontal and vertical components of magnetic signal, leaving the magnetic signal unaffected by the phononic signal.

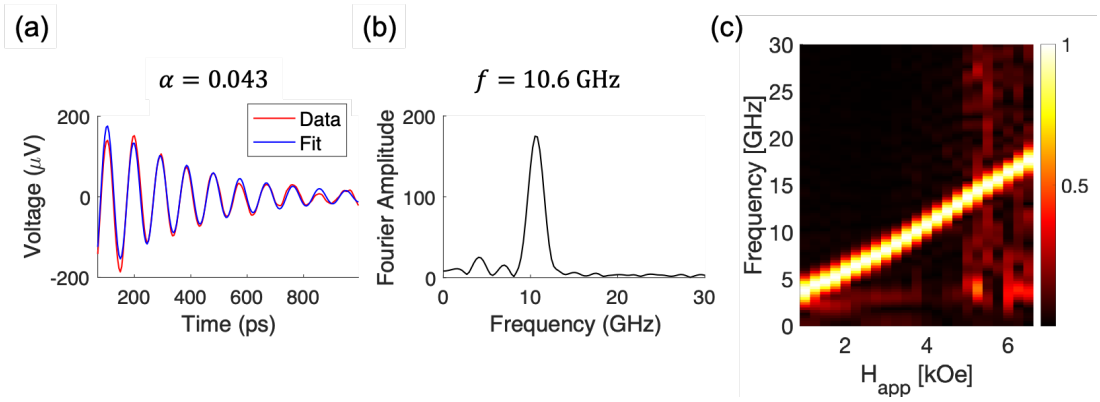

Figure 3.9. Time-dependent Kerr rotation of z-component of magnetization of a Ni thin film. (a) Voltage data taken in the time domain from the difference channel and (b) its Fourier transformed data, showing a single resonance frequency. (c) Accumulated Fourier transformed data of (b) after sweeping over various H_{app}.

The electric signals detected at the BPD are collected and amplified by lock-in amplifiers and analyzed using software, such as LabVIEW. As shown in figure 3.9a, the signals are originally taken in the time domain and their thermal background is subtracted for further analysis. Now that the signal represents the Kerr rotation, θ_{K}, the following equation is used for the fitting to calculate the magnetic precession frequency and damping parameter.[67,68]

$$\theta_{\mathrm{K}} = A\sin(\omega t + \phi)e^{-\frac{t}{\tau}}\ , \tag{3.1}$$

where $\omega = 2\pi f$ is the angular frequency of magnetic precession described by LLG equation, and τ is the decay rate related to the effective Gilbert damping parameter, $\alpha_{\mathrm{eff}} = \frac{1}{\omega\tau}$. To analyze the magnetic precession dynamics in the frequency domain, Fourier transformation is taken to the fitted plot (Fig. 3.9b). Finally, externally applied magnetic field is swept along the range of interest, and the accumulated frequency response seen in figure 3.9b is collected on a single colormap to plot the magnetic precession frequency over the applied magnetic field (Fig. 3.9c).

To study magnon-phonon coupling in a nanoscale magnet, a microscope system with a piezoelectric stage can be introduced in addition to the typical TR-MOKE with the BPD configuration. The piezo-stage provides spatial control of a sample on the nanoscale to align the laser beams to the magnetic nanostructures. Another important step when exciting an array of nanomagnets is to defocus the pump beam to homogeneously excite the broad area of nanomagnets. As the pump and pulse beams

at different wavelengths pass the objective lens, they undergo chromatic aberration, leaving the two beams focused at different planes. At the focal plane where the probe beam is focused, the pump beam is then defocused to cover a larger area ensuring that the nanostructure is homogeneously excited. The detailed sample preparation and techniques for various ways (hot and cold excitation methods) to study the hybrid magnon-phonon system using TR-MOKE with BPD configuration are introduced in reference [69] and will be discussed in the subsequent sections with example studies.

One drawback of TR-MOKE is that the back reflection of the probe beam reflected from the film surrounding the nanoelement. If the back reflection is stronger than the magnetization signal, this can be a critical issue. In this case, introducing an anti-reflection (AR) coating on the substrate when patterning the nanoelement helps absorbing the probe beam. For example, hafnium oxide (HfO_2) can be used for AR-coating for 800 nm wavelength of probe beam.

Chapter 4. Magnetoelastics in Nanomagnets

4.1. Magnetoelastic Effect (Villari Effect) and Magnetostrictive Materials

4.1.1. Magnetostriction and Magnetoelastic Effect (Villari Effect)

In general, there are different ways to excite magnetization dynamics: external magnetic fields, thermal or optical excitation. More recently, the option to couple into the mechanical degrees of freedom of a material and create strain-induced dynamics has come into focus. Initially, this relationship was found by Joule in 1842 when the magnetic materials undergo change in magnetization, a deformation to their original dimension was found, suggesting there is a relationship between strain and the magnetization.[70] This phenomenon is called *magnetostriction effect*. The fundamental origin of magnetostriction lies in the spin-orbit coupling. One of the examples of spin-orbit coupling affecting the magnetic energy is magnetocrystalline anisotropy and magnetostriction is closely related to this energy.

To explain the origin of magnetostriction effect, let us take an example of a virtual material system that shows an extremely strong spin-orbit coupling described in figure

4.1. Notice that the electron clouds are elongated along the spin orientation to exaggerate the strong spin-orbit coupling. Without the presence of an external magnetic field ($H_{\text{app}} = 0$), the net magnetization and the electron clouds would be rotated into the preferred orientation – magnetic easy-axis (left to right in this figure). Here, magnetocrystalline anisotropy is the energy that accounts for the act of rotation and the spin-orbit coupling is the mechanism why both net magnetization and the electron clouds rotate simultaneously. Now, we apply a magnetic field on the crystal perpendicular to the easy-axis. Generally, a few hundred Oersted is sufficient to overcome the magnetocrystalline anisotropy energy and to rotate the orientation of spins away from the easy-axis. Then the net magnetization would be rotated along the direction of the applied magnetic field, hence the electron clouds rearranged. Because of the realignment in the atomic structure, there is a change in distance between the nuclei, hence the total length of the crystal has changed by ΔL. The ratio of deformation in length is called magnetic field-induced magnetostriction, and it is expressed as $\frac{\Delta L}{L}$.

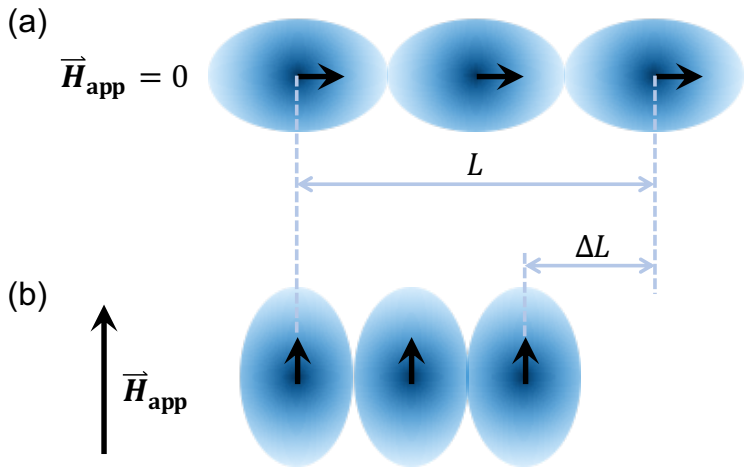

Figure 4.1. Schematics of mechanism of magnetostriction below T_C (a) without applied magnetic field and (b) with applied magnetic field. The ellipses represent the electron clouds belonging to each atom, the dark area at the center of the ellipses represents atomic nuclei, the arrows at the center of the electron clouds indicate the vector of the net magnetic moment per atom.

One of the most important parameters that affects the magnon-phonon coupling is, hence, the saturation magnetostriction coefficient, λ_S . Generally, the linear magnetostriction coefficient, λ is defined by the fraction of change in length of a magnetic material, when it is exposed to a magnetic field. When the strain in the magnetic material reaches its saturation, the change in length is defined as the saturation magnetostriction coefficient (unless specified, generally it is called "magnetostriction coefficient"), $\lambda_S = \frac{\Delta L}{L}$. The strain due to the applied magnetic field is on the order of 10×10^{-6}, and usually saturated at a fairly low magnetic field of $<$

1000 Oe. The unit for magnetostriction coefficient is 10^{-6} or often used as [ppm] – parts per million.

The saturation magnetostriction coefficient for cubic crystals having ⟨100⟩ or ⟨111⟩ as an easy-axis is given by,

$$\lambda_S = \lambda_{100} + 3(\lambda_{111} - \lambda_{100})(\alpha_1{}^2\alpha_2{}^2 + \alpha_2{}^2\alpha_3{}^2 + \alpha_3{}^2\alpha_1{}^2)\,, \qquad (4.1)$$

where $\alpha_1, \alpha_2, \alpha_3$ are the direction cosines, and λ_{100} , λ_{111} are the saturation magnetostriction coefficient along the ⟨100⟩ and ⟨111⟩ direction, respectively.

For polycrystalline materials, there is one magnetostriction coefficient regardless of their orientation. It is because we assume that each grain is oriented randomly, i.e. in a way that their magnetostriction is averaged out over the entire crystal. Therefore, the average magnetostriction in polycrystalline materials, $\bar{\lambda}_S$, is given by,

$$\bar{\lambda}_S = \frac{2}{5}\lambda_{100} + \frac{3}{5}\lambda_{111}\,. \qquad (4.2)$$

The opposite phenomenon to the magnetostriction is called **magnetoelastic effect**, or the **Villari effect**, where there is a change in magnetization of a material when a stress is applied to it. The magnetoelastic energy is provided in a paper by L. Néel in 1954[71] and the magnetoelastic energy is derived from the exchange energy between the two nearby spins. By adding the exchange energy for all the nearest neighbor pairs in a unit volume, the magnetoelastic energy, E_{MEL} for the simple cubic lattice is generalized,

$$E_{\mathrm{MEL}} = B_1\left[\varepsilon_{xx}\left({\alpha_1}^2 - \frac{1}{3}\right) + \varepsilon_{yy}\left({\alpha_2}^2 - \frac{1}{3}\right) + \varepsilon_{zz}\left({\alpha_3}^2 - \frac{1}{3}\right)\right] + B_2\left[\varepsilon_{xy}\alpha_1\alpha_2 + \varepsilon_{yz}\alpha_2\alpha_3 + \varepsilon_{zx}\alpha_3\alpha_1\right], \quad (4.3)$$

where B_1 and B_2 are the magnetoelastic constants that describe the relationship between magnetostriction coefficients (λ_{100}, λ_{111}) and the elements of stiffness tensors (c_{11} and c_{12}, c_{44}) by,

$$\left(\frac{\Delta L}{L}\right)_{100} \equiv \lambda_{100} = -\frac{2}{3}\frac{B_1}{c_{11} - c_{12}},$$

$$\left(\frac{\Delta L}{L}\right)_{111} \equiv \lambda_{111} = -\frac{1}{3}\frac{B_2}{c_{44}}\,. \quad (4.4)$$

4.1.2. Magnetostrictive Materials – Building Blocks for Magnetoelastic Coupling

Material	$\bar{\lambda}_S\ [10^{-6}]$	$\lambda_{100}\ [10^{-6}]$	$\lambda_{111}\ [10^{-6}]$
Fe		20.7 [72]	−21.2 [72]
Ni		−45.9 [72]	−24.3 [72]
$Ni_{61.9}Fe_{38.1}$	14.7 [73]		

$Co_{0.8}Fe_{2.2}O_4$	-210 [74]	-590 [74]	120 [74]
$Co_{73}Fe_{27}$	260 [75]	1300 [75]	
Galfenol ($Fe_{83}Ga_{17}$)	400 [76]	> 250 [77]	
$TbFe_2$	2500 [78]		
Terfenol-D ($Tb_{0.3}Dy_{0.7}Fe_2$)	1200 [79]		

Table 4.1. Magnetostriction coefficients for selected magnetostrictive materials.

4.1.2.1. 3d Transition Metals

3d transition metals such as Fe, Ni and Co are some of the most popular magnetic material systems. As a matter of fact, the first report of magnetostriction phenomenon observed by Joule was using Fe particles[70]. The magnetostriction constants and elastic moduli for Ni and Fe are given in table 4.1 below. Ni possesses medium magnetostriction, large enough to enable the studies introduced in the subsequent section that will demonstrate magnon-phonon coupling in a Ni thin film and strong magnon-phonon coupling in a single Ni nanoelement[32].

4.1.2.2. Terfenol-D Alloy ($Tb_{0.3}Dy_{0.7}Fe_2$)

Among the $4f$ rare-earth (RE) metals, rare-earth transition-metals (RE-TM) with Tb alloys are known to possess large magnetostriction coefficient at the order of $10^3 \times 10^{-6}$ due to their unquenched orbital magnetic moments. The magnetostriction

of $TbFe_2$ was measured to be over $\lambda_{111} = 2500 \times 10^{-6}$ at room temperature[78]. However, their magnetocrystalline anisotropy is very large that such high magnetostriction can be only achieved when high magnetic field is applied ($H_{\text{app}} = 8\ \text{kOe}$). To overcome such high magnetocrystalline anisotropy, Dy compounds are introduced in TbFe alloy, Terfenol-D ($Tb_{0.3}Dy_{0.7}Fe_2$) to be particular, because they have the opposite signs in anisotropy which lowers the magnetocrystalline anisotropy, while exhibiting high magnetostriction constants of 1200×10^{-6} at $H_{\text{app}} = 0.5\ \text{kOe}$ under 10 MPa (Fig. 4.2)[79].

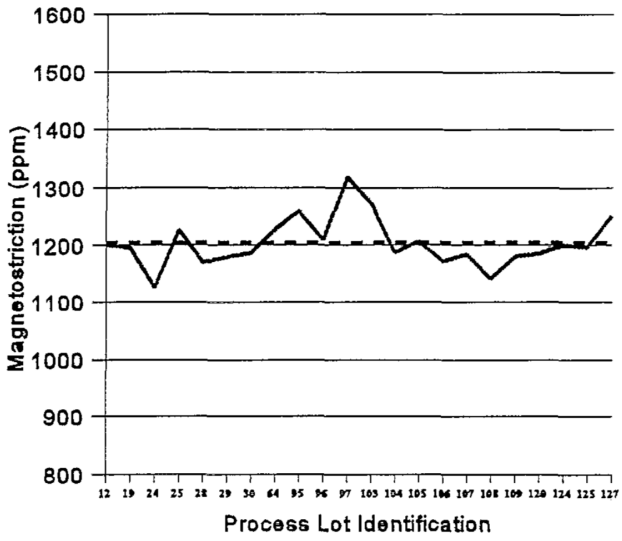

Figure 4.2. Magnetostriction coefficient of Terfenol-D at 0.5 kOe under 10 MPa from multiple lots, where x-axis shows the individual lot identification number. The dashed line indicates their averaged magnetostriction coefficient.[79]

4.1.2.3. Co-Fe Alloys

Co-Fe alloys are known to have a wide range of magnetostriction values depending on their composition. The largest magnetostriction in Co-Fe alloy was observed in $Co_{73}Fe_{27}$, where the effective magnetostriction was measured at 84×10^{-6} at $H_{app} = 100$ Oe.[75] When the Co content is around 75 %, it is near the phase boundary between BCC and coexisting phase of BCC and FCC of the Co-Fe phase diagram. The effective magnetostriction of a Co-Fe alloy can be further increased up to 260×10^{-6} by adding thermal processing after the deposition of the film. Also, it was followed by an analysis showing that $\lambda_{100} \approx 1300 \times 10^{-6}$ can be achieved in this system.[75] Indeed, strong magnon-phonon coupling was observed in a single polycrystalline CoFe nanoelement[80] and will be discussed in chapter 4.3.

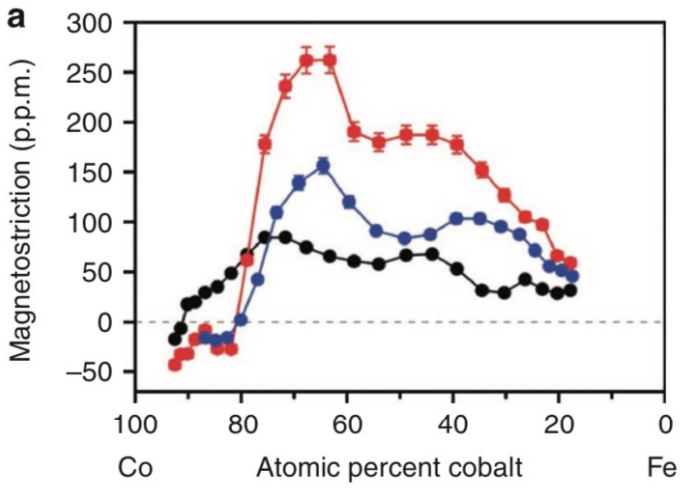

Figure 4.3. Magnetostriction coefficient of $Co_{1-x}Fe_x$ at three different post deposition treatments; as deposited (black dots), annealed and slow-cooled (blue dots), annealed and water quenched (red dots).[75]

4.1.2.4. Galfenol Alloys (Fe-Ga)

When a small amount of Ga substitutes Fe atoms, a large magnetostriction of $\lambda_{100} > 250 \times 10^{-6}$ was measured for $Fe_{83}Ga_{17}$ at up to $H_{app} = 100$ Oe under 10.3 to 96.5 MPa.[77] To increase the magnetostriction constant, further thermal treatment was processed, and a magnetostriction value of 400×10^{-6} was achieved.[76]

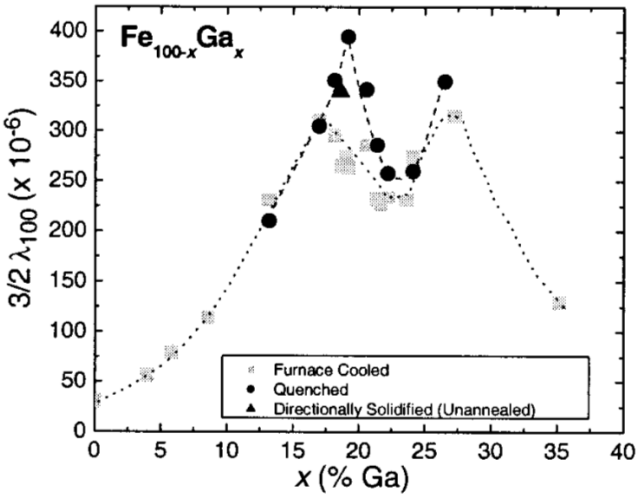

Figure 4.4. Magnetostriction of $Fe_{1-x}Ga_x$ alloys at different thermal treatments as a function of Ga composition.[76]

4.2. Surface-Acoustic Wave (SAW)-Driven Magnetoelastic Coupling

One of the most popular forms of creating mechanical modulation of a material is via surface acoustic waves (SAW). The most common realization of SAW-driven magnetoelastic coupling is a planar magnetic film deposited on an elastic and non-

magnetic, often piezoelectric, substrate, as described in figure 3.1. A more complicated geometry can be adopted to study isolated acoustic waves in a suspended membrane, despite the added complexity of fabrication. In this device configuration, a thick magnetic film deposited on a piezoelectric is suspended in air after back etching of the base substrate. Due to the significant thickness of the magnetic film, the strain along the thickness is nonuniform, hence spin waves can be excited (Lamb waves)[81]. On the other hand, in the commonly used structure as described in figure 3.1, as an example, tens of nanometer-thick magnetic thin film is used. In this configuration, the thickness of the magnetic film is small enough to approximate that the strain is uniform across the thickness of the magnetic film. Therefore, the uniform FMR mode is excited. The Rayleigh-type SAW and the Love-type SAW are examples of surface acoustic waves that can be excited in this thin film geometry, where the Rayleigh wave is a longitudinal wave and the Love wave is a shear horizontal wave.

The magnetization dynamics via magnetoelastic coupling can be experimentally realized by utilizing various form of phononic excitation; electrically, thermally, and optically. Before exploring experimental methods to excite the SAW-driven, we will discuss the theoretical aspect of magnetoelastically coupled dynamics. In the following subsections, we illustrate each of three approaches with representative examples and show how elastic waves can interfere with the intrinsic magnetization dynamics, but also be used as new approaches to extract intrinsic magnetic material properties.

4.2.1. Theoretical Overview of Magnetoelastically Coupled Dynamics

The traveling wave is characterized by its velocity that is close to the sound wave – this is the origination of the term 'acoustic' wave -, and their frequency. In an exemplary demonstration of driving magnetization dynamics with SAWs, a Ni film was placed between the interdigital transducers (IDT) (Fig. 4.5).[31] In this configuration, the magnetization dynamics is indirectly excited by the traveling SAWs at a frequency predetermined by the period of the IDT and material property of the substrate.

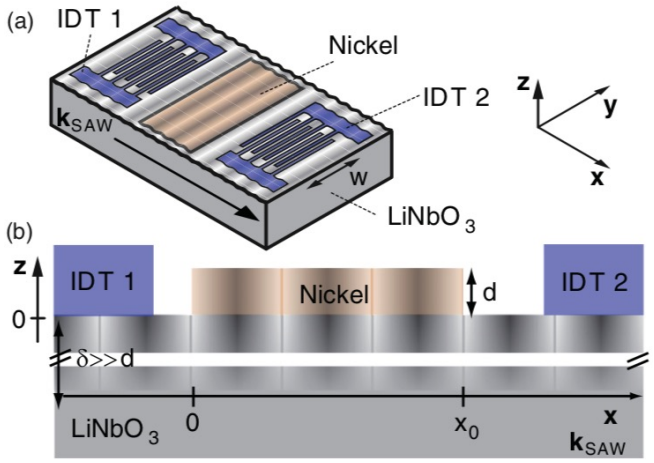

Figure 4.5. (a) Schematics of the sample construction considered in SAW excited magnetization dynamics. (b) Cross-section of the sample set up.[31]

The sample configuration considered in this work is given in figure 4.5 and is similar to the setup discussed in chapter 3.2.[32] In the case where the acoustic waves are traveling with the vector $\vec{\boldsymbol{k}} = k_x\hat{\boldsymbol{x}}$, and the fundamental frequency of the SAW is

determined based on the period of the transducer, and their higher orders can be used to tune their frequencies. Therefore, the angular frequency of phonon mode, ω_{ph}, of a traveling acoustic wave is given by

$$\omega_{\mathrm{ph}} = \frac{2\pi v_{\mathrm{R}}}{P} = v_{\mathrm{R}} k_x, \tag{4.5}$$

where $v_{\mathrm{R}} = 3440\ \mathrm{m/s}$ is the Rayleigh sound velocity, P is the period of the IDT bars. As we consider more complicated dynamics including the magnetoelastic coupling, the wave propagation of SAW cannot be described by the equation (4.5) anymore. Instead, their dynamics is described by solving the elastic wave equation below.

$$\rho \frac{\partial^2}{\partial t^2} u_i = \sum_{j=1}^{3} \frac{\partial}{\partial x_j} \sigma_{ji}\,, \tag{4.6}$$

where ρ denotes mass density of medium, u_i are the displacement vector components in an acoustic wave medium from its original position with respect to the unstrained solid, with $i = \{x, y, z\}$ in (x, y, z) coordinate system. σ_{ji} is the Cauchy stress tensor given by

$$\sigma_{ji} = \frac{\partial}{\partial \varepsilon_{ji}} W^{\mathrm{tot}}\,, \tag{4.7}$$

where $\varepsilon_{ij} = \left(\frac{\partial u_i}{\partial x_j} + \frac{\partial u_j}{\partial x_i}\right)/2$ denotes the strain elements, and $i, j = \{x, y, z\}$ in (x, y, z) coordinate system, W^{tot} is the total elastic energy stored in the nanomagnets.

To describe the equation of motion including the influence of magnetoelastic coupling in the magnetic materials, additional energy term describing the magnetoelastic coupling (G^{d}) is introduced to the total Gibbs free energy in equation (2.45).

$$G^{\mathrm{tot}} = G + G^{\mathrm{d}}\,, \tag{4.8}$$

$$\begin{aligned} G^{\mathrm{d}} = {} & b_1\left[\varepsilon_{xx}(x,t){m_x}^2 + \varepsilon_{yy}(x,t){m_y}^2 + \varepsilon_{zz}(x,t){m_z}^2\right] \\ & +2b_2\left[\varepsilon_{xy}(x,t)m_x m_y + \varepsilon_{yz}(x,t)m_y m_z + \varepsilon_{zx}(x,t)m_z m_x\right], \end{aligned} \tag{4.9}$$

where b_1 is the magnetoelastic constant responsible for compressive/tensile stress and b_2 is the magnetoelastic constant responsible for shear stress. Note that the Gibbs free energy used in this section is normalized to both total volume (V) and magnetization (M).

Accordingly, the total elastic energy in the wave equation (Eq. 4.7) considers both elastic energy and the magnetoelastic energy. Thus, the total elastic energy is found,

$$W_{\mathrm{EL}} = \frac{1}{2} C_{ijkl}\varepsilon_{ij}\varepsilon_{kl},$$

$$W_{\mathrm{MEL}} = G^{\mathrm{d}} M,$$

$$W^{\mathrm{tot}} = W_{\mathrm{EL}} + W_{\mathrm{MEL}} = \frac{1}{2} C_{ijkl}\varepsilon_{ij}\varepsilon_{kl} + G^{\mathrm{d}} M. \tag{4.10}$$

Here, we introduced Einstein notation to express the elastic energy, where C_{ijkl} are the elements of the stiffness tensor. Finally, solving the elastic wave equation returns the displacement in terms of magnetization.

Quantitative understanding of magnetization dynamics requires revisiting the LLG equation (Eq. 2.43) and incorporating the elastic deformation of the magnetic material. As discussed in chapter 4.1, spin waves experience reorientation due to the presence of spin-orbit coupling when acoustic waves alter their solutions (u_i) as a result of magnetoelastic coupling. Corresponding magnetoelastic free energy is added to the magnetic system, which in return, induces magnetoelastic field $\vec{\boldsymbol{H}}_{\mathbf{MEL}}$

$$\vec{\boldsymbol{H}}_{\mathbf{MEL}} = -\vec{\nabla}_{\mathbf{m}} G^{\mathrm{d}} . \tag{4.11}$$

Therefore, the effective magnetic field in equation (1.6) is modified to reflect the magnetoelastic coupling term,

$$\begin{aligned} \vec{\boldsymbol{H}}_{\mathbf{eff}}^{\mathbf{tot}} &= -\vec{\nabla}_{\boldsymbol{m}}(G + G^{d}) \\ &= -\left[\begin{pmatrix} G_{11}m_1 + G_{12}m_2 \\ G_{12}m_1 + G_{22}m_2 \\ G_3 \end{pmatrix} + \begin{pmatrix} G_1^d \\ G_2^d \\ G_3^d \end{pmatrix}\right], \end{aligned} \tag{4.12}$$

where $G_{ij} = \frac{\partial}{\partial m_i}\frac{\partial}{\partial m_j} G\Big|_{m=m_0}$, and $G_i^{\mathrm{d}} = \frac{\partial}{\partial m_i} G^{\mathrm{d}}\Big|_{m=m_0}$.

We assume that the phononic vibration is a plane wave, taking a plane wave ansatz for the displacement component, $u_i = u_i^0 e^{i(\vec{k}\cdot\vec{x} - \omega_{\mathrm{ph}} t)}$. Due to the magnon-phonon coupling, we assume that the magnetization components follow the spatial profile of

SAW. Therefore, the magnetization is assumed to follow plane wave ansatz, $m_{1,2}(t) = m_{1,2}^{0} e^{i(\vec{k}\cdot\vec{x}-\omega_{\mathrm{ph}}t)}$. Again, the Gilbert damping parameter is ignored in this derivation for simplicity. Substituting $\overrightarrow{\boldsymbol{H}}_{\mathbf{eff}}$ with $\overrightarrow{\boldsymbol{H}}_{\mathbf{eff}}^{\mathbf{tot}}$ from equation (4.12), equation (2.53) is found,

$$\begin{pmatrix} G_{12} - \dfrac{i\omega_{\mathrm{M}}}{\gamma} & G_{22} - G_3 \\ G_{11} - G_3 & G_{12} + \dfrac{i\omega_M}{\gamma} \end{pmatrix} \begin{pmatrix} m_1(t) \\ m_2(t) \end{pmatrix} = \begin{pmatrix} -G_1^{\mathrm{d}} \\ -G_2^{\mathrm{d}} \end{pmatrix}. \tag{4.13}$$

Comparing equation (4.13) for the coupled dynamics and equation (2.61) of the counterpart, the magnetization precession frequency considering the magnetoelastic coupling shows the distinct response compared to the bare magnetic film.

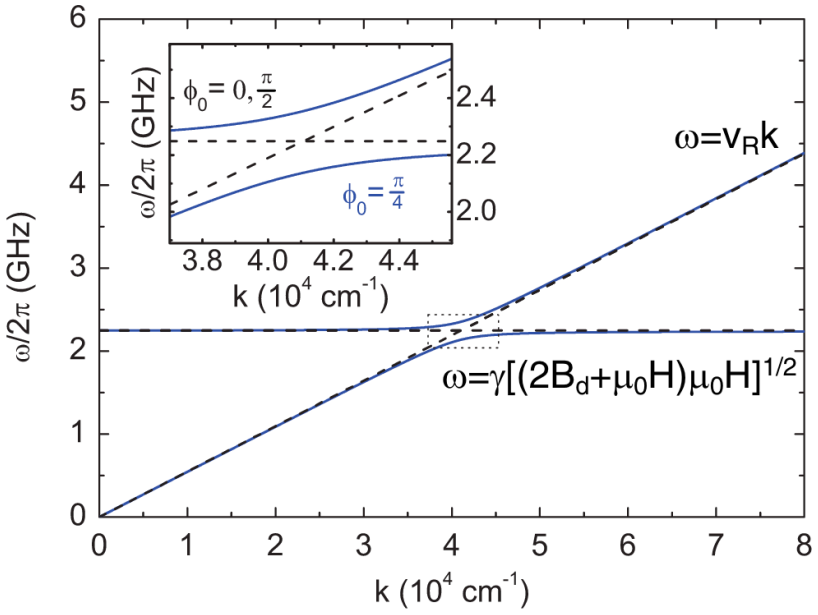

Figure 4. 6. Dispersion plot using the solution obtained from equation 4.13. [31] The k represents k_x, and H represents H_{app} in the main text.

Let us take a dispersion relation shown in figure 4.6 as an example to explain how the solution for the magnetoelastically coupled system is distinguished from the uncoupled system. The black dashed line shows solutions for uncoupled system, where the k-independent line represents magnetic response based on solving equation (2.61), and the k-dependent line represents the solution for phononic response in equation (4.5). These two distinct solutions can intersect when their solutions cross at the same angular frequency, representing uncoupled system. On the other hand, the solutions for the coupled dynamics solved using the equation (4.13) are marked with blue solid lines, showing anti-crossing when the magnonic and phonoic solutions intersect. The detailed derivation for solving the equation (4.13) is well described in the reference [31],

therefore we will lightly go over this particular example to provide more insight on the magnetoelastically coupled system.

The non-zero strain tensor elements for the longitudinal Rayleigh-type SAW are ε_{xx}, ε_{xz}, and ε_{zz}, while for the shear horizontal Love-type SAW, the dominant non-zero strain tensor element is ε_{xy}. Therefore, in this example where the SAW is excited at $\vec{\boldsymbol{k}} = k_x\hat{\boldsymbol{x}}$, we consider only ε_{xx}, ε_{xy}, and ε_{xz} strain components. As the strain tensor elements enter the magnetoelastic energy term, the magnetoelastic coupling exhibits a characteristic anisotropy with respect to the angle of the applied magnetic field. Considering the strain tensor elements of interest, equation (4.8) and (4.10) now read as,

$$W_{\mathrm{EL}} = \frac{1}{2}C_{11}{\varepsilon_{xx}}^2 + \frac{1}{2}C_{44}{\varepsilon_{xy}}^2\,, \tag{4.14}$$

$$G^{\mathrm{d}} = b_1[\varepsilon_{xx}(x,t){m_x}^2] + 2b_2\left[\varepsilon_{xy}(x,t)m_x m_y + \varepsilon_{zx}(x,t)m_z m_x\right]. \tag{4.15}$$

Notice that the equation (4.15) also depends on the $\hat{z}$-coordinate, therefore the strength of magnetoelastic coupling is impacted by the thickness of the magnetic thin film[82].

Now, solving the equation (4.13) yields the coupled equation with variables M_1 and M_2 and $u_{x,y,z}$. The solution can be found by setting the determinant to vanish in equation (4.13).

To provide insight into the complicated solution, let us take an example with a simplified case of a pure longitudinal wave where $\varepsilon_{xy} \neq 0$ and $\varepsilon_{xy} = \varepsilon_{xz} = 0$, (also $u_x \neq 0$ and $u_y = u_z = 0$).

The solution is then found,

$$\left[\omega^2 - {v_l}^2 {k_x}^2 \left(1 - \frac{F{b_1}^2}{{v_\mathrm{l}}^2 \mu_0 \rho}\{\chi_{11}{w_1}^2 + \chi_{22}{w_2}^2 - (\chi_{12} + \chi_{21})w_1 w_2\}\right)\right] u_x = 0, \quad (4.16)$$

where

$$w_1 = 2 \sin\theta_\mathrm{M} \cos\theta_\mathrm{M} \cos^2\phi_\mathrm{M},$$

$$w_2 = 2 \sin\theta_\mathrm{M} \cos\phi_\mathrm{M} \sin\phi_\mathrm{M},$$

$v_\mathrm{l} = \sqrt{\frac{c_{11}}{\rho}}$ represents the velocity of the acoustic longitudinal wave, χ_{ij} is the component of the Polder susceptibility tensor ($\overleftrightarrow{\chi}$) that describes the relations $M = \overleftrightarrow{\chi} H$, $F = \frac{d}{\delta}$ is the filling factor to account for the fact that only a fraction of volume is strained by the SAW that strains the magnetic film. Here, d is the thickness of the magnetic film and δ is the penetration depth of the SAW.

If we consider a case where the magnetization is oriented along the in-plane direction (i.e. $\theta_\mathrm{M} = {\pi}/{2}$), and $\mathrm{v_l} = v_\mathrm{R}$, where v_R represents the Rayleigh type of SAW while ignoring the transverse component (i.e., the wave is purely longitudinal), then equation (4.16) is simplified to

$$\omega^2 = {v_\mathrm{R}}^2 {k_x}^2 \left[1 - \frac{4F{b_1}^2 \sin^2\phi_\mathrm{M} \cos^2\phi_\mathrm{M} \left(\mu_0 H_\mathrm{app} + 2B_\mathrm{d}\right)\mu_0 M}{{v_\mathrm{R}}^2 \mu_0 \rho \left(\mu_0 H_\mathrm{app} + 2B_\mathrm{d}\right)\mu_0 H_\mathrm{app} - \left(\frac{\omega}{\gamma}\right)^2}\right]. \quad (4.17)$$

The solution for this case in equation (4.17) is plotted in figure 4.6 in the dispersion relation for $\phi_{\mathrm{M}} = 0, \frac{\pi}{2}$ and $\phi_{\mathrm{M}} = \frac{\pi}{4}$. The parameters used in calculation is found $\mu_0 H_{\mathrm{app}} = 6.7\ \mathrm{mT}$, $B_{\mathrm{d}} = 0.4\ \mathrm{T}$, $v_{\mathrm{R}} = 3440\ \mathrm{m/s}$, $d = 50\ \mathrm{nm}$, $b_1 = 23\ \mathrm{T}$, $b_2 = b_1$ (polycrystalline film), $\rho = 8900\ \mathrm{kg/m^3}$, $\gamma = 2.185\ \mu_{\mathrm{B}}/\hbar$, where μ_{B} is the Bohr magneton, and the $\hbar$ is the Planck constant.

At $\phi_{\mathrm{M}} = 0$ and $\frac{\pi}{2}$, the equation (4.17) becomes identical to equation (4.5), converging to the case without the presence of magnetoelastic coupling (i.e., only considering two distinct solutions for magnetic frequency and phononic frequency). In this case without coupling, the two modes can intersect at $\frac{\omega}{2\pi} = 2.24\ \mathrm{GHz}$ (solution for magnon modes at $\mu_0 H_{\mathrm{app}} = 6.7\ \mathrm{mT}$), showing a clear mode crossing where two solutions have identical solution (dashed line). However, in the case with $\phi_{\mathrm{M}} = \frac{\pi}{4}$, there is a clear anti-crossing where the two solutions show distinct frequency splitting when the magnon and phonon interfere. This splitting is a hallmark of coupling of two quanta.

4.2.2. Electrically Excited Magnetoelastic Coupling

In the electrical excitation method, interdigital transducers (IDTs) are most popular, where a set of 2 IDTs are patterned for generating the SAW and detecting the SAW transmission (see chapter 3 above).

This approach is exemplified by the system described in chapter 3.2. A magnetic polycrystalline Ni thin film (thickness: $d = 50$ nm, width: $w = 400$ nm, length: $x_0 = 570$ μm) was e-beam evaporated on a Y-cut Z-propagating $LiNbO_3$ piezoelectric substrate. Two sets of aluminum (Al) IDTs (thickness 70 nm, spacing 5 μm) are fabricated so that one set of IDTs can function as a SAW generator and the other set of IDTs as a receiver after passing through the Ni thin film. The given IDT geometry generates SAWs at a fundamental frequency of 172 MHz. However higher harmonics of 5^{th}, 9^{th}, and 13^{th} harmonic frequencies are used (corresponding to 0.86, 1.55, and 2.24 GHz) to support the SAW-driven FMR study.

It is worth mentioning that the cut direction of piezoelectric substrates provides additional selectivity. As mentioned in the previous sections, the various types of surface acoustic waves have distinct polarization. There are two common types of cut directions used in SAW-driven magnetoelastic coupling; An "ST-cut" refers to the substrates cut slightly tilted from the main crystal direction, whereas "X (or Y, Z) -cut" refers to the substrates cut perpendicular to the $\hat{x}$ (or $\hat{y}$, $\hat{z}$) axis. Therefore, ST-cuts can be used to selectively excite shear propagating acoustic waves (Love waves), whereas Y-cut can support exciting both Rayleigh and Love waves.

Figure 4.7 compares the experimental and theoretical data of the power absorbed (P_{abs}) due to SAW-driven FMR, the transmission magnitude ($|S_{21}^{\mathrm{norm}}|$) and its phase ($arg(S_{21}^{\mathrm{norm}})$) for three configurations.

As for the experimental data, the resonantly absorbed power, P_{abs} was calculated based on measuring the scattering parameter (S_{11}), and the complex forward transmission (S_{21}). In the experimental setting, S_{11} refers to the voltage ratio between the reflected and applied electromagnetic waves at the transducer, and S_{21} refers to the voltage ratio between the electromagnetic waves detected at IDT 2 and applied at IDT 1. Then P_{abs} was calculated by

$$P_{\mathrm{abs}} = (1 - |S_{21}^{\mathrm{norm}}|^2) P_{\mathrm{SAW}}, \tag{4.18}$$

where $S_{21}^{\mathrm{norm}} = S_{21}(\mu_0 H)/S_{21}(\mu_0 H_{\mathrm{off}})$, $\mu_0 H_{\mathrm{off}}$ is the off-resonance magnetic field of $\mu_0 H_{\mathrm{off}} = 150\ \mathrm{mT}$ for the in-plane configuration, and $\mu_0 H_{\mathrm{off}} = 1.2\ \mathrm{T}$ is the off-resonance magnetic field for the out-of-plane configurations. $P_{\mathrm{SAW}} = \Delta|S_{11}|^2 P_0$, where $\Delta|S_{11}|^2$ denotes the magnitude of the dip observed at the matching harmonic center frequency of the transducer, and P_0 denotes the input power supplied to the transducer.

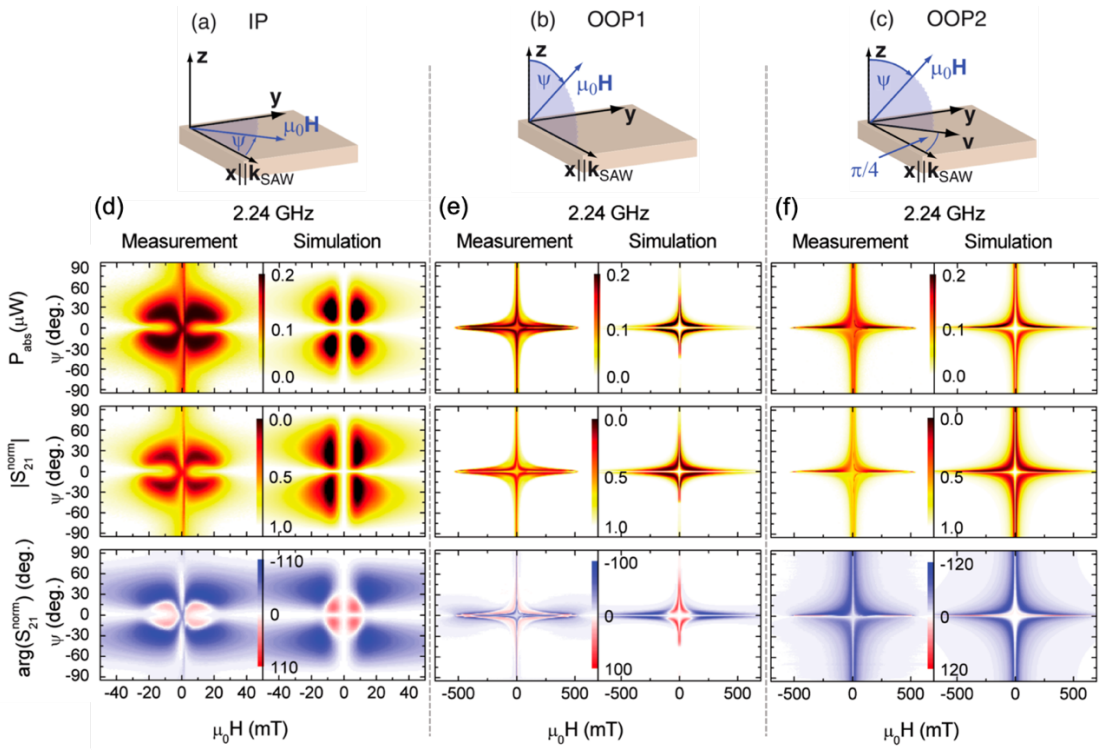

Figure 4. 7. (a-c) Experimental geometries for three different configurations of applied external magnetic field ($\mu_0\boldsymbol{H}$) and its angle (ψ) away from the major axis**.** [31] (a) in-plane (IP) where $\mu_0\boldsymbol{H}$ lies within the xy film plane, (b) out-of-plane 1 (OOP1) where $\mu_0\boldsymbol{H}$ lies within the xz plane, (c) out-of-plane 2 (OOP2) where $\mu_0\boldsymbol{H}$ is rotated from OOP1 configuration by $\pi/4$ with respect to the $\hat{z}$ axis. (d-f) Side-by-side comparison of measurement and simulation data of P_{abs}, $|S_{21}^{norm}|$, and $arg(S_{21}^{norm})$ for various applied magnetic fields and angles.

For the corresponding simulation plots, the absorbed power was calculated based on the energy conservation upon FMR, where a portion of the SAW power was consumed

to drive the magnetization dynamics. Therefore, P_{abs} was taken from the imaginary part of the change of the transmitted power ΔP, which is given by

$$\Delta P = -\frac{\omega \mu_0}{2} \int_{V_0} (h_1^*, h_2^*) \bar{\chi} \begin{pmatrix} h_1 \\ h_2 \end{pmatrix} dV \,, \tag{4.19}$$

where V_0 denotes the volume of the ferromagnetic thin film, h_1 and h_2 are $\mu_0 h_i = -G_i^{\mathrm{d}}$ $(i = 1, 2)$ are taken by solving the equation (4.13). The normalized complex scattering parameter, S_{21}^{norm} was taken from describing the resonant attenuation and phase shift of the acoustic wave. The longitudinal acoustic wave upon magnetoelastic interaction with a small perturbation is given by

$$u_x(x = x_0) = u_x(x = 0) e^{ik_0 x_0} e^{i\Delta k x_0}, \tag{4.20}$$

$$S_{21}^{\mathrm{norm}} = e^{i\Delta k x_0},$$

$$arg(S_{21}^{\mathrm{norm}}) = \mathrm{Re}[\Delta k_x] x_0,$$

where $k_0 = \omega / v_{\mathrm{R}}$ is the unperturbed wave number, and the change in wave number due to perturbation is given by $\Delta k = F \frac{\omega b_1^2}{2 v_{\mathrm{R}}^3 \mu_0 \rho} \{\chi_{11} w_1^2 + \chi_{22} w_2^2 - (\chi_{12} + \chi_{21}) w_1 w_2\}$.

The comparison between the experimentally and theoretically calculated P_{abs} and S_{21}^{norm} show that this model accounts for the behavior of SAW-driven magnetoelastic coupling in a ferromagnetic thin film.

4.2.3. All-Optical Thermally Excited Magnetoelastic Coupling

The all-optical thermal excitation method involves impulsively heating the magnetic elements with a laser pulse. The laser pulse initially provides thermal energy to the magnetic nanostructures, raising their temperature to cause a three-dimensional deformation. Subsequently, the strain waves propagate along the surface of the substrate layer, mediating collective lattice vibration to propagate in phase throughout the nanomagnets. It is worth noting that all-optically induced magnetoelastic coupling can be also realized in a magnetic thin film without introducing nanostructures. In this case, two spatially interfering ultrafast light pulses can be used to generate SAWs[83], or multiferroic heterostructure can be involved[84].

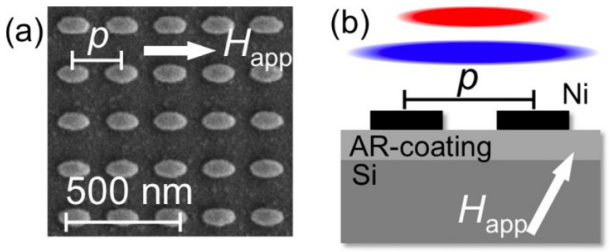

Figure 4.8. (a) SEM image of an array of polycrystalline Ni nanomagnets. (b) Schematics showing the thermal excitation method. Ni nanomagnet arrays (periodicity = p) patterned on an AR-coated on Si substrate. The red circle on top of the nanomagnets represents the probe beam and the blue circle represents the pump beam. [85]

One of the early studies of strain-driven magnetization dynamics in nanomagnets were investigated by Yahagi et. al. in dense periodic arrays.[44] Specifically, an array of elliptical polycrystalline Ni nanomagnets (140 nm $\times$ 80 nm, thickness 30 nm) was periodically patterned ($p = 212$ nm) on an antireflection coating (HfO_2 AR-coating, 110 nm) on a Si substrate (Fig. 4.8a).[85] In this thermal excitation method as depicted in figure 4.8b, a laser pulse is used both to drive the magnetization dynamics, and to provide thermal expansion in the nanomagnet array. Then the strain wave propagates from the nanomagnet to the substrate, enabling the SAW to travel on the surface, mostly in the AR-coating layer.

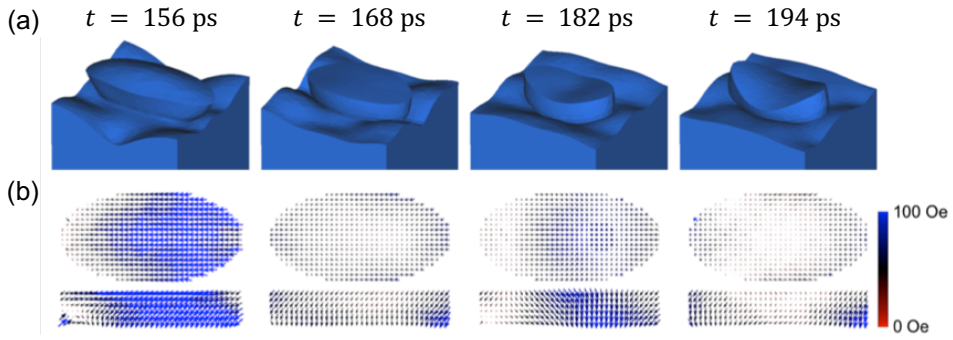

Figure 4.9. (a) displacement of nanomagnet at different timing of thermal excitation in a periodic unit cell. The amplitude of nanomagnet is exaggerated for better display. (b) Effective magnetoelastic field induced at magnetic element.[86]

To provide more insight on laser pulse induced thermal excitation, the finite element method (FEM) simulation is used to describe the dynamics of geometry given in figure 4.8a. The figure 4.9a shows the dynamics of displacement in the nanomagnet in a

periodic unit cell calculated using FEM simulation. Note that the backaction dynamics including W_{MEL} is not considered in this elastic wave equation to simply present the impact of laser pulse on the displacement of elastic wave by only considering W_{EL}. Once thermally excited by the laser pulses, the nanomagnets are thermally expanded and their fluctuation of displacement is described by the elastic wave equation (Eq. 4.6). Interestingly enough, the spin orientation within the nanomagnet is also affected by the strain in the nanomagnets (Fig. 4.9b) due to **magnetoelastic coupling**. This reconfiguration of spin waves induces H_{MEL} as depicted in the figure 4.9b on the orders of ~ 100 Oe.

It should be noted that the SAW in this experiment follows the behavior of Rayleigh Waves. At each nanomagnet, acoustic waves form nodes, therefore the SAW frequency is controlled dominantly by the period of the nanomagnet array in the following way.

$$f_{\mathrm{SAW}} = \sqrt{h^2 + k^2}\,\frac{v_{\mathrm{S}}}{P}\,, \tag{4.21}$$

where h and k are the indices, v_{S} is the speed of acoustic wave of a medium, and P is the period of the nanoelement. In this case, the SAW medium is the thin AR-coating layer and the speed of acoustic wave in this medium is $v_{\mathrm{S}} \sim 2400\ \mathrm{m/s}$.

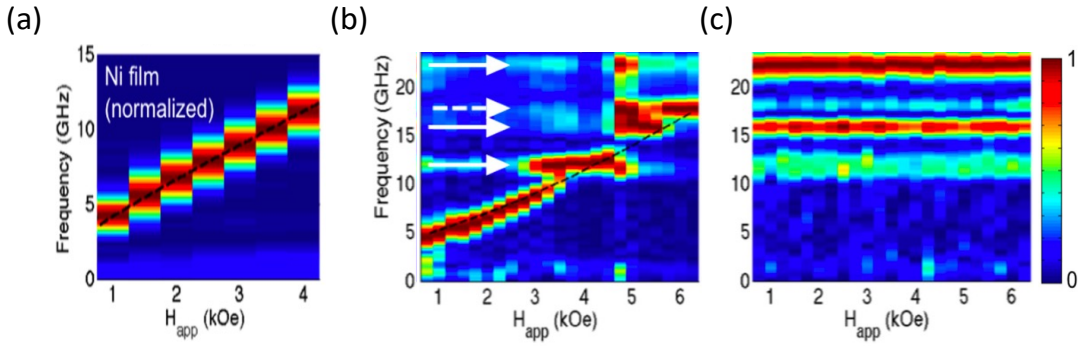

Figure 4.10. TR-MOKE spectra taken from the magnonic channel measured for (a) Ni film and (b) array of Ni nanomagnets presented in figure 4.8, and (c) the spectra taken from the phononic channel for Ni nanomagnets (white arrows: SAW frequencies).[85]

Their magnetization dynamics is compared to the bare Ni film without any patterning on the surface and plotted in figure 4.10a. A single magnetic precession frequency is clearly seen in the figure with a good agreement with the Kittel mode calculated in the precious chapter. However, the magnetic response of an array of Ni nanomagnets follows distinctly different response as anticipated due to the magnetoelastic coupling (Fig. 4.10b). To be specific, the magnetic response marked at the white arrows at higher magnetic field shows pinning of broad-field response at the frequency where the phononic frequencies coincides with the magnonic frequency.

The magnetoelastic coupling is observed in the magnetic channel as the pinning of the magnetic precession frequency increases where it coincides with the SAW frequencies (Fig. 4.10c). In this case the SAW frequencies are observed at $12.2_{(1,0)}$, $15.8_{(1,1)}$, and $22.3_{(2,0)}$ GHz marked with the white arrows in the non-magnetic channel. Such pinning

in the magnetic frequency at the intersection suggests that the SAW and the magnetic Kittel modes are coupled. There is another frequency observed at the non-magnetic response at 17.7 GHz which originates from the surface skimming longitudinal wave (SSLW). The SSLW is the in-plane longitudinal acoustic wave, and it is a type of surface wave. However, as an SSLW propagates, the elastic energy in SSLW dissipates from the magnetic layer at a greater rate than the SAW's[87,88]. This results in a shorter lifetime compared to SAWs, however their velocity remains in the range of the longitudinal acoustic wave (near 6000 m/s).

4.2.4. Controlling the Magnetoelastic Coupling

Phonons are known to exhibit longer lifetime. Due to this, when the phonons and magnons are coupled via magnetoelastic effect, the magnetic response shows a lot lower effective damping parameter. In other words, having magnetoelastic effect when measuring the damping property with nanopatterned magnetic film greatly interfered, as well as the magnetization precession frequency is affected showing the pinning effect. In order to reduce the interference caused by the coupling, a couple of methods were explored.

4.2.4.1. Control via Dielectric Coating Layer

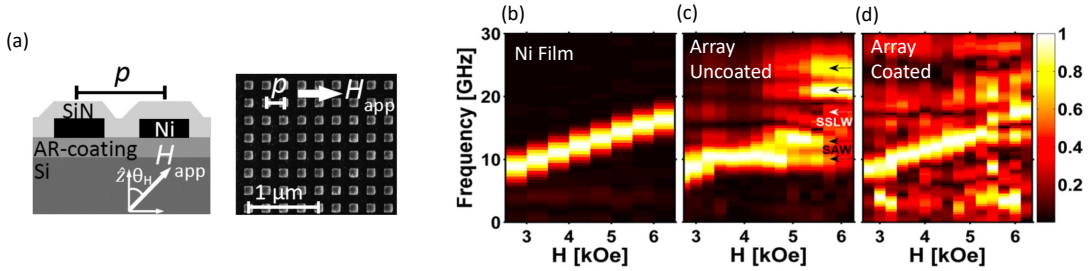

Figure 4.11. (a) Schematics and SEM image of an array of nanomagnet capped with SiN dielectric layer. (b-d) Fourier spectra taken from the magnonic channel for (b) Ni film, (c) uncoated array (without SiN layer), and (d) coated array (with SiN layer).[89]

In figure 4.11a, the thick dielectric coating (SiN, thickness 65 nm) was deposited on top of an array of square polycrystalline Ni nanomagnets (125 nm × 125 nm, thickness 30 nm, period 250 nm) on the AR-coated layer (HfO_2, 110 nm).[89] The magnetic response of the array of square Ni nanomagnets is given in figure 4.11c. Without the deposition of a SiN coating, as the magnetoelastic coupling is in play, the magnetic response shows pinning at the intersection of the phononic frequencies marked with the black arrows. In contrast, the magnetic response of coated array of Ni nanomagnets recovers from its coupled magnetic dynamics showing more prominent Kittel mode similar to the response of the bare Ni film case (Fig. 4.11b, d). It is due to the fact that the thick deposition of dielectric layer suppresses the vibration in the substrate, thereby hindering the transfer of SAW in the nanomagnets.

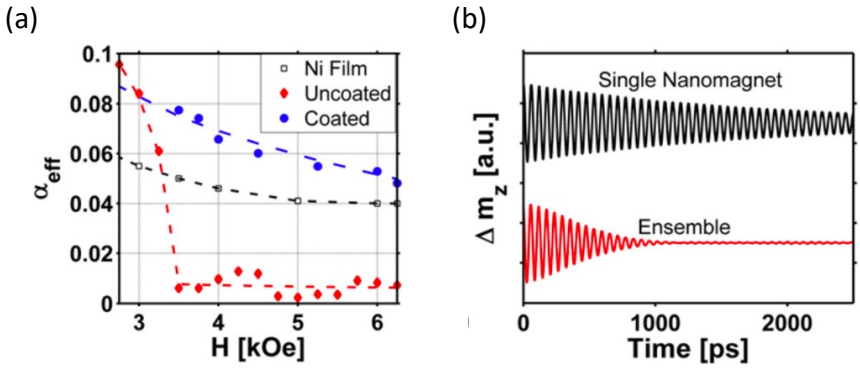

Figure 4.12. (a) Effective damping parameter for Ni film (unfilled square), uncoated array (red diamond), and coated array (blue dots). (b) OOMMF simulation of Δm_z for a single nanomagnet and an array of nanomagnet (Ensemble).[89]

One of the properties of coupling of magnon and phonon is that the lifetime of magnons tend to be elongated due to the longer lifetime of phonons. The effective magnetic damping parameter (α_{eff}) is related to the effective lifetime (τ_{eff}) as given by,

$$\alpha_{\text{eff}} = \frac{1}{2\pi f_{\text{mag}} \tau_{\text{eff}}} . \tag{4.22}$$

To investigate the effect of extended lifetime in magnon dynamics due to magnetoelastic coupling, the effective magnetic damping parameter is plotted in figure 4.12a. As predicted by the property of magnetoelastic coupling between magnon and phonon, the effective damping parameter is observed to be lower for the uncoated array of Ni nanomagnets, due to the coupling to the long-lived phononic modes regardless the applied magnetic fields. The lowest effective damping was observed at $H_{\text{app}} = 5\ \text{kOe}$, where $\tau_{\text{eff}} \sim 5000\ \text{ps}$ for the array of nanomagnets without the coating, in

contrast to $\tau_{\text{eff}} \sim 300$ ps for the bare film. It confirms that the magnetoelastic coupling extended the lifetime of magnons, in this case, nearly $16 \times$ longer.

On the other hands, the effective damping parameter for the coated array does not show such lower damping. This is because the coating suppresses the coupling of magnon and phonon, thereby the pure magnetic response is more dominant. However, it is noticed that the effective damping parameter for the coated array is observed to exhibit higher value than that of the bare film. The effective damping parameter is dependent on both intrinsic (ω_{int}) and extrinsic property (ω_{ext}) of the magnetic elements. The origin of extrinsic damping is found due to the magnetic inhomogeneity (ω_{MI}) arising from the local anisotropy in nanomagnets that contributes to the anisotropy field (H_{K}), also due to the various shapes of the magnetic array ω_S that broadens the precession frequency resulting in the dephasing.[90]

$$\Delta\omega_{\text{eff}} = \Delta\omega_{\text{int}} + \Delta\omega_{\text{ext}} = \Delta\omega_{\text{int}} + \Delta\omega_{\text{MI}} + \Delta\omega_{\text{S}} \,. \tag{4.23}$$

The micromagnetic computation result plotted in figure 4.8b suggests that the extrinsic magnetic damping is contributed from the array of nanomagnets in this case.

4.2.4.2. Control via Random Array

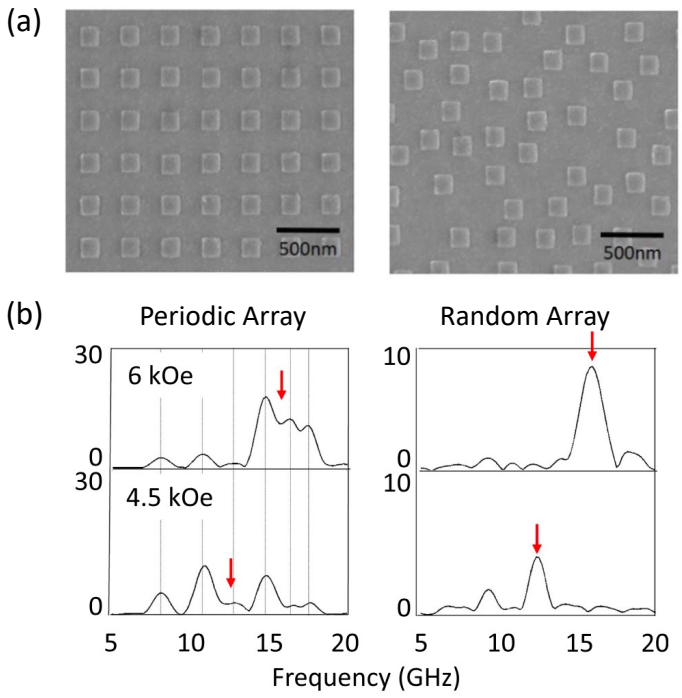

Figure 4.13. (a) SEM images of periodic array (left) and randomized array (right). (b) Fourier spectra at $H_{app} = 4.5\ kOe$ and $6\ kOe$ for periodic (left) and randomized (right) array.[91]

Another strategy to decouple the magnetoelastic coupling between magnons and phonons is by randomizing the pattern of a nanomagnet array as shown in figure 4.13a.[91] Both arrays of square polycrystalline Ni nanomagnets (156 nm × 156 nm, thickness 30 nm) are patterned on an AR-coated layer (HfO_2, 110 nm) on a silicon substrate, with the same dimensions. The period of nanomagnets in the periodic

array is $P = 330$ nm with corresponding fill factor of 0.22, and the random array was patterned to exhibit the same filling factor with random periods.

The phononic eigenfrequencies for the periodic array were calculated using the equation 4.5, with $P = 330$ nm, and the speed of the acoustic wave, $v_s = 2673$ m/s was used, as the medium of acoustic wave is dominantly determined by the elastic property of AR-coating layer underneath the nanomagnets.

The magnetic response of both periodic and random arrays is shown in figure 4.9b. In the spectra of the periodic array, there are multiple magnetic precession frequencies, which shows great agreement with the phononic frequencies marked as a gray line for both $H_{\mathrm{app}} = 4.5$ kOe and 6 kOe. Note that these frequencies are independent of the applied fields. On the other hand, a single dominant peak originating from the pure magnetic Kittel mode is observed in the random array (figure 4.13b, marked with red arrow). Therefore, the magnetic response is restored to exhibit a single magnetic Kittel mode, suggesting that the magnetoelastic coupling has vanished in the random array.

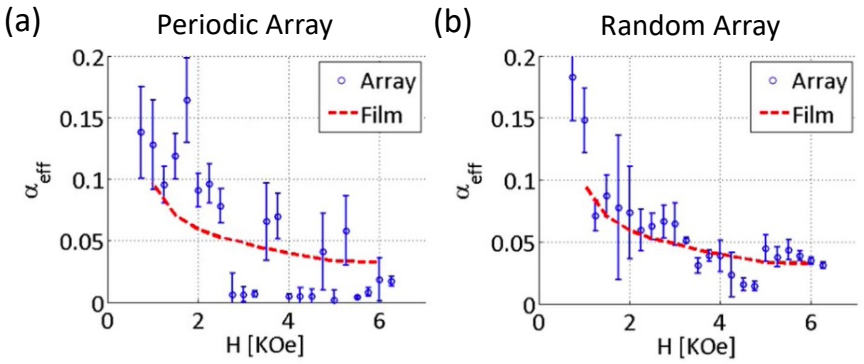

Figure 4.14. Effective damping parameter of Kittel mode or magnetoelastically coupled mode for (a) periodic array and (b) randomized array – see figure 4.13.[91]

In order to confirm that the magnetic response is fully restored, the effective damping parameter was taken for both periodic array and random array (Fig. 4.14). In the periodic array, the magnetic damping parameter was shown lower than the case with the film due to the magnetoelastic coupling. On the other hand, the effective damping parameter shows similar response as the film suggesting that the restored magnetic response in the random array allows physically meaningful magnetic studies.

4.2.5. Magnetoelastic Coupling as a Measure of Intrinsic Damping

So far, we have considered direct optical excitation of the nanomagnets via thermal excitement using laser pulses. This method intrinsically involves thermal effects on the magnetization dynamics dampening the lifetime of magnons at lower applied magnetic fields. In the next exemplary work, a single nanomagnet was considered and it was

excited by a SAW without involving thermal excitation of the nanomagnet. Therefore, this approach is called “cold excitation”. In this configuration, the magnetic dynamics within the nanoelements are driven by SAWs induced by thermal excitation far away from the nanomagnet, representing an all-optical version of the IDT generated SAWs of chapter 3. The geometry involves the periodic metal bars patterned around a nanomagnet, where the laser pulse is used to introduce the thermal vibration on the metal bars. The strain pulse of the SAW travels normal to the periodic bars toward the nanomagnet where it initiates the magnetization dynamics.

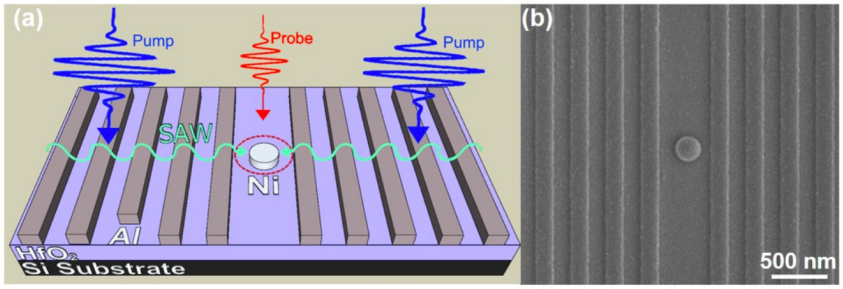

Figure 4.15. (a) Schematics of cold excitation method using SAW grating bars and the Ni nanomagnet. (b) SEM image of SAW gratings and the Ni nanomagnet.[92]

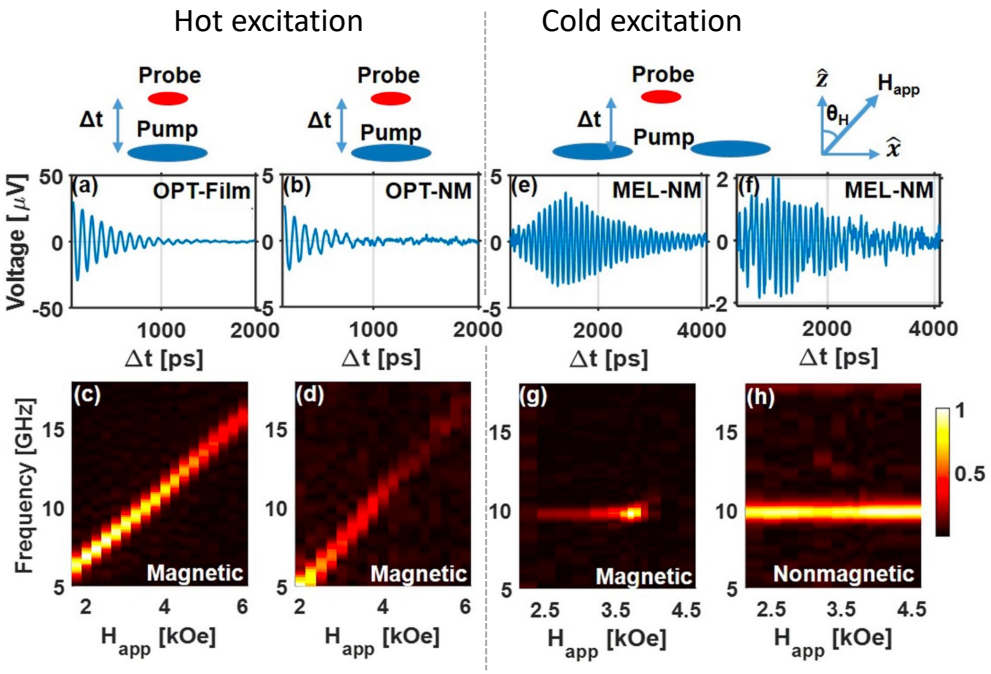

Figure 4.16. (a-b) Time traces and (c-d) corresponding Fourier spectra of magnetization precession taken with TR-MOKE using the hot excitation method for (a, c) Ni film and (b, d) a single Ni nanomagnet (NM). (e-f) Time trace and (g-h) corresponding Fourier spectra of a single Ni nanomagnet using the cold excitation method. (e-g) Data taken from magnonic channel. (f-h) Data taken from phononic channel.[92]

This approach was accomplished by positioning a single nanomagnet between non-magnetic aluminum metal bars as seen in figure 4.15.[92] A single circular polycrystalline Ni nanomagnet (Diameter 200 nm, thickness 30 nm) was patterned on an AR-coated layer (HfO_2, thickness 110 nm) on a silicon substrate, and four different periods of Al bars were patterned ($P = 250, 300, 350, 400$ nm) using two-step e-beam lithography

and e-beam evaporation. It is worth noting that the sample preparation technique for the optical cold excitation method is simpler than other methods of cold excitation, such as IDTs which require expensive piezoelectric materials and electrical control and synchronization. The corresponding SAW frequencies of the Al gratings are given by,

$$f_{\mathrm{SAW}} = \frac{v_{\mathrm{S}}}{P}\,, \tag{4.24}$$

where the speed of the acoustic wave in the HfO_2 AR-coating layer was estimated at $v_{\mathrm{S}} \sim 3000\ \mathrm{m/s}$. Using this formula, the frequencies of acoustic wave from the four distinct Al bars with four different P were found at $f_{\mathrm{SAW}} = 11.45, 9.75, 8.65,$ and 7.75 GHz.

In the cold optical excitation configuration, as depicted in the figure 4.15a, the Al SAW bars are excited by the laser pulses, and the SAWs are generated due to the thermal vibrations in the Al bars, similar to the previously studied arrays of nanomagnets. Then the strain wave propagates orthogonally to the SAW bars toward the nanomagnet, thereby driving the magnetic dynamics inside the nanomagnet without introducing the thermal effect (cold excitation). The magnetization dynamics shown in a single nanomagnet by thermal excitation via laser pulse without the presence of SAW, follows magnetic Kittel modes similar to the case of bare film (Fig. 4.16a - d).

In contrast, when the magnetization dynamics within the nanomagnet is driven by the magnetoelastic coupling, their magnetic response shows different response. As shown in figure 4.16e, f, both the amplitudes of magnetic precession and acoustic wave

increase and peak at $\Delta t \sim 1$ ns. As the center of the laser pulse is located at the Al bars ~ 3 μm away from the nanomagnet, it takes approximately ~ 1 ns for the acoustic wave to arrive at the nanomagnet to initiate the magnetoelastic driven magnetization dynamics. Because the nanomagnet is only excited at the f_{SAW} (Fig. 4.16h), the magnetic precession at other frequencies is impossible (Fig. 4.16g). Furthermore, more than 4 × extended lifetime of magnon was also observed in the magnetoelastic driven magnetization dynamics (Fig. 4.16e), in contrast to the hot excitation of a single nanomagnet using the laser pulse (Fig. 4.16b).

One of the advantages of using the magnetoelastic driven excitation method (cold excitation) is that thermal effects are not involved in the magnetization dynamics in the nanomagnet. The effective damping parameter is determined by both intrinsic and extrinsic according to the relation,

$$\frac{1}{\tau_{\mathrm{eff}}} = \frac{1}{\tau_{\mathrm{Gilb}}} + \frac{1}{\tau_{\mathrm{ext}}}\ , \tag{4.25}$$

where τ_{Gilb} is the lifetime associated with the intrinsic Gilbert damping (α) and τ_{ext} is the lifetime determined by the additional damping (extrinsic damping) that hampers the in-phase precession of magnetization and generally depends on applied magnetic field. Therefore, the cold excitation method provides a reliable method to extract the intrinsic Gilbert damping parameter. In the polycrystalline Ni film, the damping mechanism that accounts for the extrinsic damping is two-magnon scattering (TMS). Thus, α can be found using the model presented by[93–96]

$$\alpha_{\text{eff}} = \frac{1}{2\pi f_{\text{mag}}}\left[\frac{1}{\tau_{\text{Gilb}}} + \frac{1}{\tau_{\text{TMS}}}\right], \tag{4.26}$$

$$\approx \frac{1}{2\pi f_{\text{mag}}}\left[\frac{\alpha\gamma(H_1 + H_2)}{2}\right.$$
$$\left. + N_0 \sum_k \frac{C(k)}{2\pi f_{\text{mag}}} \text{Im}\left\{4\pi^2\left({f_{\text{mag},k}}^2 - {f_{\text{mag}}}^2 + i\delta f_{\text{mag},k} f_{\text{mag}}\right)^{-1}\right\}\right],$$

where $H_{1,2}$ are effective fields contributed from the applied field and demagnetization field, $N_0 = \frac{\gamma^4}{3}(H_1 + H_2)\langle h'^2\rangle$ is the scattering intensity, where h' is the magnitude of inhomogeneous field due to sample defects, $C(k) = \frac{2\pi\xi^2}{[1+(k\xi)^2]^{3/2}}$ is the correlation function, where ξ is the correlation length of h', $f_{\text{mag},k}$ and $\delta f_{\text{mag},k}$ are the frequency of spin wave and wave-vector-dependent inverse lifetime.

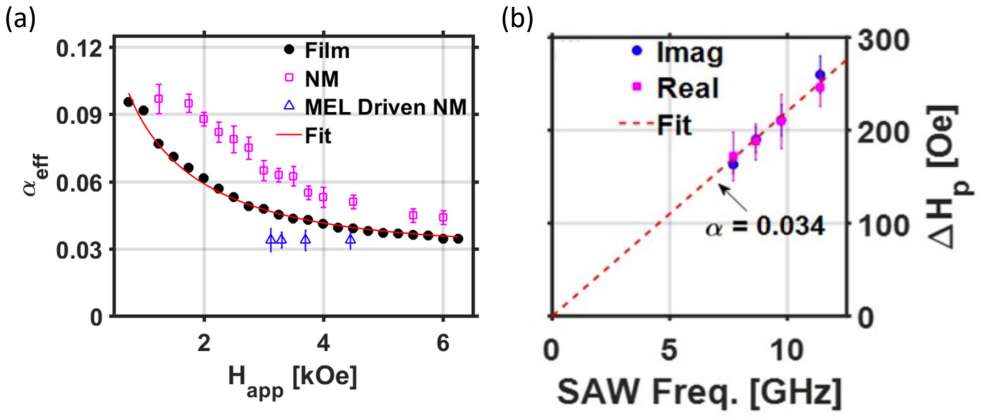

Figure 4.17. (a) Effective damping parameter at various magnetic field taken for Ni film with hot excitation method (black circles), a single Ni nanomagnet with hot excitation method (pink square), a single Ni nanomagnet with cold excitation method

(MEL driven NM, blue triangle). (b) Pinning width (ΔH_P) taken with 4 different SAW frequencies.[92]

To investigate this, the effective damping parameter of the three cases were extracted using the equation (4.22). The effective damping parameter of thermally excited nanomagnet follows similar behavior of the bare film case, while consistently higher than the effective damping parameter of the film. It is because the thermal conductivity of HfO_2 is nearly $\times 10^{-2}$ times lower than Ni. During the laser heating, the temperature of Ni nanomagnet patterned on the HfO_2 rises higher than the Ni film, which contributes to reducing the τ_{ext}, thus increasing α_{eff}. The fitting was done using the equation (4.26), and the extracted intrinsic Gilbert damping parameter was taken at $\alpha = 0.03$.

Interestingly, the α_{eff} taken for the magnetoelastic driven magnetization shows dramatically different result (Fig. 4.13a), where the effective damping parameter exhibits field-independent response. The α_{eff} is related to the pinning width (ΔH_{P}) at the f_{SAW} given by

$$\Delta H_{\text{P}} = \alpha_{\text{eff}}\left(H_{\text{app}}\right)\frac{4\pi}{\gamma} f_{\text{SAW}}\,. \tag{4.27}$$

Using the data obtained in the figure 4.12g, the SAW frequency and the pinning width are plotted in figure 4.13b, showing linear dependency with $\alpha_{\text{eff}} = 0.034$ for the magnetoelastic driven dynamics. It is worthwhile to note that the extracted effective

damping parameter is close to the intrinsic Gilbert damping parameter ($\alpha = 0.03$) using the optical cold excitation method.

4.3. Strong Magnon-Phonon Coupling

The cooperativity, C is commonly used as a figure-of-merit to describe the strength of coherent coupling of hybrid quantum system, i.e. magnon and phonon in our study. It is described as the ratio of the induced dissipation of magnon caused by phonon (γ'_{Mag}) to the intrinsic dissipation of magnon (γ_{Mag}), $C = \frac{\gamma'_{\mathrm{Mag}}}{\gamma_{\mathrm{Mag}}}$, and vice versa. In this context, the Strong coupling of magnon and phonon is defined when the dissipation of magnon is dominated by the induced dissipation derived by phonons, $C \geq 1$. C is given by

$$C = \frac{{\Gamma_{\mathrm{C}}}^2}{\kappa_{\mathrm{M}}\kappa_{\mathrm{P}}}\,, \tag{4.28}$$

where $\Gamma = \frac{\Delta f_{\mathrm{min}}}{2}$ is the coupling rate and Δf_{min} is the frequency splitting at the mode crossing, and $\kappa_{\mathrm{M}} = \alpha_{\mathrm{M,eff}} f$ is the field-dependent magnonic loss rate with the frequency at the mode crossing, f, and the effective damping, $\alpha_{\mathrm{M,eff}}$, and $\kappa_{\mathrm{P}} = \alpha_{\mathrm{P,eff}} f$ is the field-dependent phononic loss rate with the effective damping, $\alpha_{\mathrm{P,eff}}$. In the strong coupling regime, $C > 1$ is required as it implies that coherent coupling dominates incoherent loss mechanisms.[97]

The coupling of hybrid quantum system in the strong coupling regime is of a great interest in achieving reliable quantum communication technology. The first experimental demonstration of coherent strong coupling in magnon-phonon system was recently shown by Berk et. al., in 2019.[32] Their demonstration relied on optical thermal excitation of the vibrational eigenmodes of a single square nanomagnet. In this case the frequency of phonons is mainly determined by the geometry and materials of the nanoelement. Due to the static vibration mode derived from the confined structure, the phononic modes are quantized in contrast to the continuous excitation of phononic modes in the previous section.

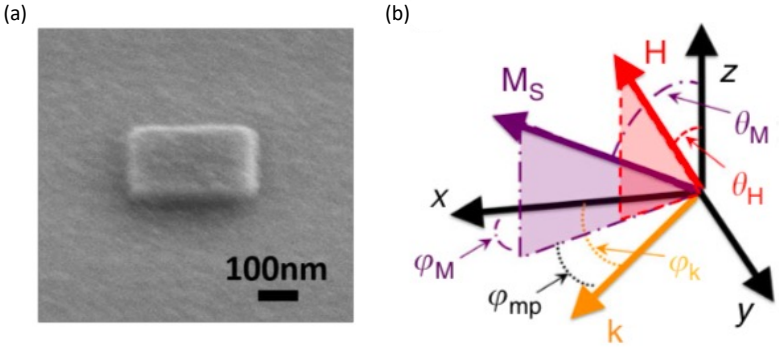

Figure 4.18. (a) SEM image of a single nanoelement considered in the theoretical and experimental calculation. (b) The coordinate system defined in this section.[32]

4.3.1. Phononic Dynamics in the Absence of Magnon-Phonon Coupling

When the phononic vibration is confined in a nanostructure as shown in figure 4.18a,[32] the phonon dynamics in the nanoelement are treated differently than the case with the traveling acoustic wave. In the previous section, we assumed that the phononic frequency is driven by the traveling SAW along the $\hat{x}$ axis. Here, however, we consider a polycrystalline square nanoelement that is directly excited by a laser pulse. In this case, the phononic vibrations are quantized along both $\hat{x}$ axis and $\hat{y}$ axis because the phonons are confined within the nanoelement. For that reason, the frequency of confined phonon within the nanoelement should be calculated differently.

We assume that the nanoelement is thin enough to be approximated as a 2D nanostructure. This allows us to neglect the $\hat{z}$ components of the displacement vector. Again, the in-plane displacement vector components are assumed to follow the plane wave ansatz,

$$u_{x,y} = u_{x,y}^{0} e^{i(\vec{k}\cdot\vec{x}-\omega_{\mathrm{ph}}t)}, \tag{4.29}$$

where $\vec{k} = k_x\hat{x} + k_y\hat{y}$ and $\vec{x} = x\hat{x} + y\hat{y}$. k is the geometry dependent wave vector which satisfies the relation $k^2 = {k_x}^2 + {k_y}^2$, and $k_{x,y} = \frac{n_{x,y}\pi}{l_{x,y}}$ where $l_{x,y}$ is the size of the nanoelement. We can further simplify the displacement vector components by examining how the phononic vibration is excited. In this case, thermally excited

phonons within the nanoelement are assumed to have equal amplitude along the $\hat{x}$ axis and $\hat{y}$ axis, due to the isotropic property of the medium ($u_x^0 = u_y^0$). The strain components that are considered in this 2D nanoelement case are ε_{xx}, ε_{yy}, ε_{xy}. The elastic energy stored in the nanoelement because of the strain provided by the phonon without considering the coupling is given by

$$W_{\mathrm{EL}} = \frac{1}{2}\left[C_{11}{\varepsilon_{xx}}^2 + C_{11}{\varepsilon_{yy}}^2\right] + \frac{1}{2}C_{44}{\varepsilon_{xy}}^2 + C_{12}\varepsilon_{xx}\varepsilon_{yy}\,. \tag{4.30}$$

Putting equation (4.30) into (4.7) to solve the elastic equation (4.6), while neglecting the W_{MEL} term for now, the angular phonon frequency is found,

$$\omega_{\mathrm{ph}} = \frac{(2\lambda + 3\mu)k^2}{2\rho}\,, \tag{4.31}$$

where we substituted $C_{11} = 2\mu + \lambda$, $C_{12} = \lambda$, $C_{44} = \mu$, where the Lamé's first parameter, $\lambda = \frac{E\nu}{(1+\nu)(1-2\nu)}$ and Lamé's second parameter, $\mu = \frac{E}{2(1+\nu)}$ are written in terms of Young's modulus, E, and the Poisson's ratio, ν.

4.3.2. Coupled Magnon-Phonon Dynamics via Magnetoelastic Coupling

The displacement component including the magnon-phonon coupling is derived by taking the same analogy as in the previous section.

First, the Gilbert energy density for the magnetoelastic coupling is given,

$$G^{\mathrm{d}} = b_1\left[\varepsilon_{xx}(x,t){m_x}^2 + \varepsilon_{yy}(x,t){m_y}^2\right] + 2b_2\left[\varepsilon_{xy}(x,t)m_x m_y\right]. \tag{4.32}$$

Combining equation (4.30) and (4.32) provides W^{tot}, and we substitute the new W^{tot} into equation (4.7) to solve the elastic wave equation (4.6). Taking the small-angle ansatz for the magnetization, $M_{1,2} = M_{1,2}^0 e^{i(\vec{k}\cdot\vec{x}-\omega t)}$, the displacement in the nanoelement accounting for the strain due to the magnetoelastic coupling is found,

$$u_x = \frac{i\left(2M_{\mathrm{s}}b_1k_xw_1 + 4M_sb_2k_yw_2\right)M_1 - i\left(2M_{\mathrm{s}}b_1k_xw_4 - 2M_{\mathrm{s}}b_2k_yw_5\right)M_2}{C_{11}{k_x}^2 + C_{12}k_xk_y + \frac{C_{44}}{2}\left(k_xk_y + {k_y}^2\right) - \rho\omega^2},$$

$$u_y = \frac{i\left(2M_{\mathrm{s}}b_1k_yw_3 + 4M_{\mathrm{s}}b_2k_xw_2\right)M_1 - i\left(2M_{\mathrm{s}}b_1k_yw_4 + 2M_{\mathrm{s}}b_2k_xw_5\right)M_2}{C_{11}{k_y}^2 + C_{12}k_xk_y + \frac{C_{44}}{2}\left({k_x}^2 + k_xk_y\right) - \rho\omega^2}, \tag{4.33}$$

where

$$w_1 = \sin 2\theta_{\mathrm{M}} \cos^2 \phi_{\mathrm{mp}},$$

$$w_2 = \sin 2\theta_{\mathrm{M}} \sin 2\phi_{\mathrm{mp}},$$

$$w_3 = \sin 2\theta_{\mathrm{M}} \sin^2 \phi_{\mathrm{mp}},$$

$$w_4 = \sin\theta_{\mathrm{M}} \sin 2\phi_{\mathrm{mp}},$$

$$w_5 = \sin\theta_{\mathrm{M}} \cos 2\phi_{\mathrm{mp}}.$$

To solve the magnetoelastcially coupled LL equation, $G_{1,2}^{\mathrm{d}}$ is found below.

$$G_1^{\mathrm{d}} = \left(b_1 w_1 i k_x + \frac{1}{2} b_2 w_2 i k_y\right) u_x + \left(b_1 w_3 i k_y + \frac{1}{2} b_2 w_2 i k_x\right) u_y ,$$

$$G_2^{\mathrm{d}} = \left(-b_1 w_4 i k_x + b_2 w_5 i k_y\right) u_x + \left(b_1 w_4 i k_y + b_2 w_5 i k_x\right) u_y . \qquad (4.34)$$

Analogous to the previous section, we can combine the equation (4.33) and (4.34) to find the coupled equation of M_1, M_2 and u_x, u_y, and plug them into equation (4.13). Finally, the solution is found by setting the determinant to 0.

$$\left(\omega^2 - {\omega_{\mathrm{ph}}}^2\right)\left[(\omega^2 - {\omega_{\mathrm{M}}}^2)\left(\omega^2 - {\omega_{\mathrm{ph}}}^2\right) - {\omega_{\mathrm{C}}}^4\right] = 0 , \qquad (4.35)$$

where

$${\omega_{\mathrm{C}}}^4 = \frac{\gamma M_{\mathrm{S}}}{\rho}(\omega_1 C_2 + \omega_2 C_1) k^2,$$

$$\omega_1 = \gamma(G_{11} - G_3),$$

$$\omega_2 = \gamma(-G_3),$$

$$C_1 = {b_1}^2(\cos^2\phi_{\mathrm{k}}\, {w_1}^2 + \sin^2\phi_{\mathrm{k}}\, {w_3}^2) + \frac{3}{4} b_1 b_2 \sin 2\phi_{\mathrm{k}}\, w_2(w_1 + w_3) + \frac{1}{2}{b_2}^2 {w_2}^2,$$

$$C_2 = {b_1}^2 {w_4}^2 + 2{b_2}^2 {w_5}^2,$$

$$b_1 = b_2 = -\frac{3\lambda_S C_{44}}{M_S}.$$

The three solutions to the equation above are $\omega = \omega_{ph}$ and $(\omega^2 - {\omega_M}^2)(\omega^2 - {\omega_{ph}}^2) - {\omega_C}^4 = 0$, which accounts for the two solutions of the coupled magnon-phonon system. The solutions for the upper equation of coupled dynamics resemble the solutions we found in figure 4.6.

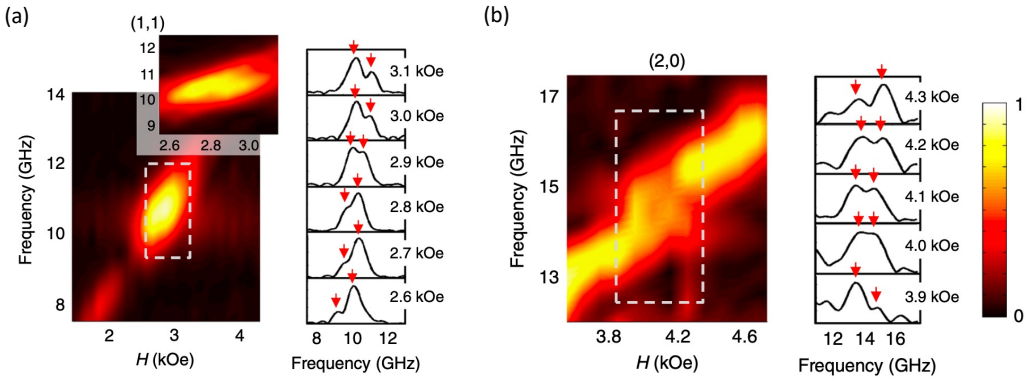

Figure 4.19. Fourier spectra of time traces taken from TR-MOKE measurement of a single Ni nanomagnet displayed in figure 4.18a showing avoided crossing for phononic mode (a) (1,1) and (b) (2,0).[32]

By sweeping the applied magnetic field, magnonic modes can be brought into the phononic eigenmodes predetermined by the geometry of the nanomagnet given in equation (4.31). Figure 4.19 shows mode crossings at two different phononic modes (1,1) and (2,0) – (k_x, k_y) – near 3 kOe and 4 kOe, respectively. There are two distinct peaks at the applied field near the crossing attributed from hybridization modes (marked with red arrows). This anti-crossing at the intersection of magnonic and

phononic modes is the hallmark of hybrid coupling. It is noteworthy that the minimum separation of two peaks at the mode crossing of (2,0) was found $\Delta f_{\min} = 0.85$ GHz which is greater than the separation at (1,1) mode ($\Delta f_{\min} = 0.76$ GHz), as the coupling strength is a function of wavevector, k^2 (eq. 4.35).

Let us examine the solutions for the coupled dynamic system. Coupling strength can be controlled by tuning the parameters in ${\omega_C}^4$. For example, properties from the choice of materials attribute mainly to $\gamma, M_S, \rho, \lambda_S, \nu, E, \alpha_{\text{eff}}, \theta_M$, and the geometrical properties attribute mainly to k, θ_M, ϕ_{mp}. In the following subsections, we will discuss controlling strong coupling by geometrical perspective and materials perspective.

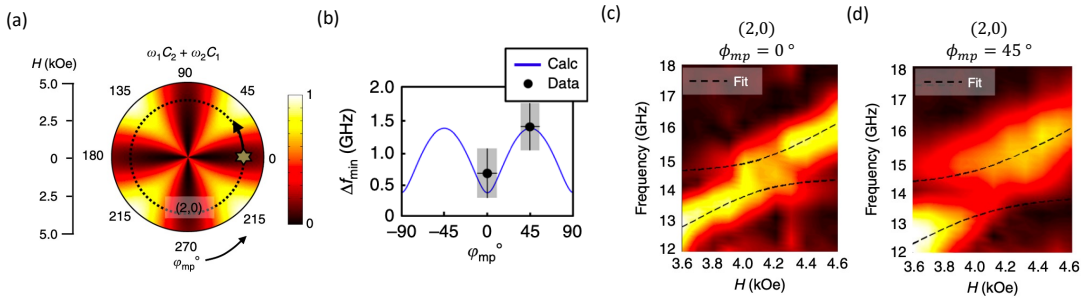

Figure 4.20. (a) The weighted coupling energy calculated for $0 < \phi_{mp} < 2\pi$ and $0 < H_{app} < 5.0\ kOe$. (b) ϕ_{mp} dependent calculated minimum frequency separation Δf_{min}. (c-d) Fourier spectra measured with TR-MOKE technique for phononic mode (2,0) for (c) $\phi_{mp} = 0°$ and (d) $\phi_{mp} = 45°$.[32]

4.3.3. Controlling Strong coupling: Geometric perspective

We can calculate the weighted coupling strength, $\omega_1 C_2 + \omega_2 C_1$ as a function of ϕ_{mp} to demonstrate how the geometrical property affect the coupling strength. The calculated weighted coupling strength for the mode crossing at $(2,0)$ is plotted in figure 4.20a as a function of H_{app} and ϕ_{mp}, while the $\theta_{\mathrm{H}} = 60^{\circ}$ remained fixed. The corresponding experimental plot of minimum frequency separation between the two peaks (Δf_{min}) at the $(2,0)$ crossing is plotted in figure 4.20b showing great agreement with the calculation. This plot shows the idea of how the geometrical tuning can be used to control the coupling strength. According to this plot, the coupling strength is at maximum at $\phi_{\mathrm{mp}} = 45^{\circ}$, in great agreement with the experimental data taken at $\phi_{\mathrm{mp}} = 0^{\circ}$(Fig. 4.20c) and 45° (Fig. 4.20d), where the anticrossing for $\phi_{\mathrm{mp}} = 45^{\circ}$ is observed larger than the case at $\phi_{\mathrm{mp}} = 0^{\circ}$.

In this geometry at $\phi_{\mathrm{mp}} = 45^{\circ}$ for $(2,0)$ mode crossing, the cooperativity was increased to $C = 1.65^{+0.48}_{-0.32} > 1$ demonstrating that the examined hybrid magnon-phonon coupled system is indeed, in the strong coupling regime.

5. Hybrid Magnon-Phonon Dynamics in a Poly-crystalline CoFe Nanomagnet

5.1. Introduction

Ni does not possess a high magnetostriction coefficient compared to some of the materials introduced in chapter 4. Nonetheless, Berk et al., were able to demonstrate Strong coupling in a single Ni nanomagnet system as discussed in the previous chapter.[98] According to equation (4.35), the coupling strength ${\omega_C}^4$ is also dependent on λ_S. It suggests that composing a hybrid magnon-phonon system using materials that have larger magnetostriction can enhance the coupling strength.

Figure 5.1. Illustration of fabrication process for poly-crystalline CoFe nanomagnet. The process starts from left to right.

5.2. Phononic Dynamics in a Single Nanomagnet (NM)

Poly-crystalline square CoFe nanomagnets (here after, CoFe NM) of dimensions of $208 \times 208 \times 30\ \mathrm{nm}^3$ were patterned using e-beam lithography, then the $Co_{50}Fe_{50}$ was

deposited via e-beam evaporator and finished by the lift-off of the metal layer and e-beam PMMA layer (Fig. 5.1). This patterning process was done in collaboration with the Molecular foundry at University of California Berkeley. The magnetic and phononic response of the fabricated CoFe NM were measured by sweeping the externally applied magnetic field ($3\,kOe \leq \mathrm{H}_{app} \leq 6\,kOe$) with the magnetic field applied along the edge of the CoFe NM ($\phi_{\mathrm{H}} = 45°$) using TR-MOKE technique with BPD as described in chapter 3. Additionally, the magnetic response of the poly-crystalline CoFe thin film (here after, CoFe thin film) was measured to compare the magnetic dynamics of the CoFe NM.

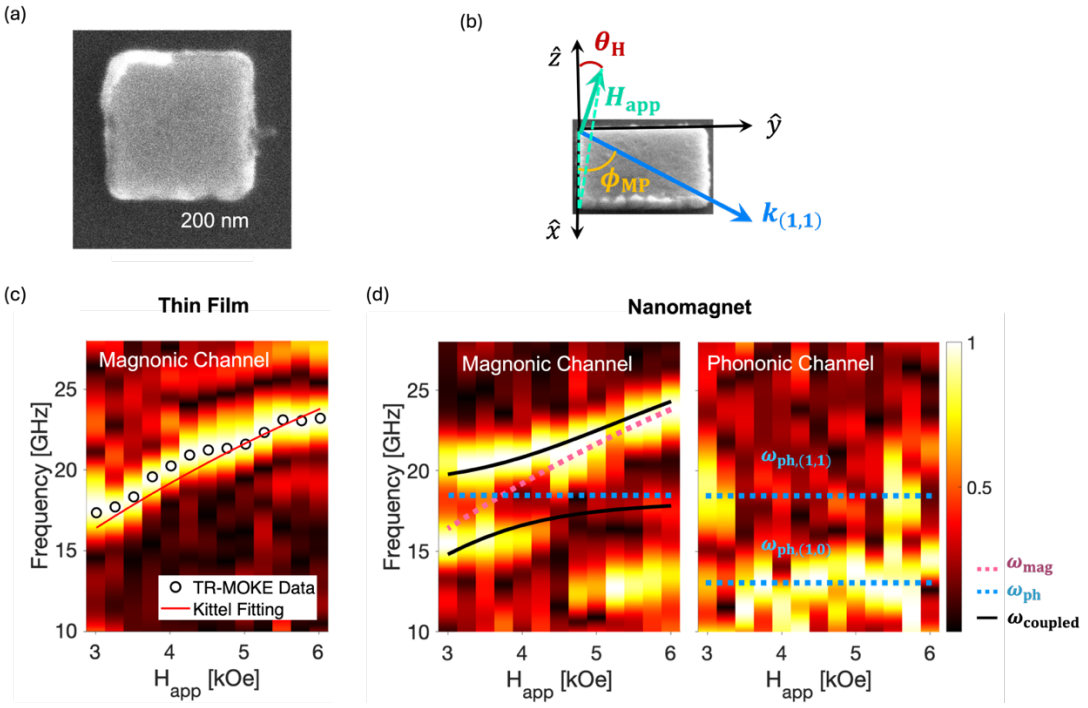

Figure 5.2. (a) SEM image of a nanomagnet ($208 \times 208 \times 30\ nm^3$) fabricated using the process mentioned in figure 5.1(a). (b) Geometry of H_{app} and $k_{(1,1)}$ with respect to x, y, z coordinate on an SEM image of an arbitrary p-CoFe nanomagnet. (c, d) Fourier-

transformed TR-MOKE data presented in the frequency domain initially taken in the time domain by sweeping the externally applied magnetic field ($3\ kOe \leq H_{app} \leq 6\ kOe$). (c) The frequency response of magnonic dynamics of the CoFe thin film. Black circles represent the experimentally taken data points and the red line is the fit to the Kittel mode for poly-crystalline thin film. (d) The frequency response of magnonic (left) and phononic (right) response of the CoFe NM. The pink (blue) dotted line demonstrates the magnonic (phononic) frequency without the presence of magnon-phonon coupling, and he black solid line represents the fit to the coupled magnon-phonon dynamics showing great agreement with the experimentally obtained data.

The optically obtained frequency response of magnonic dynamics of the CoFe thin film is shown in figure 5.2(c). The experimentally taken magnonic frequency was fit to the Kittel mode calculated using equation (2.50), substituting $\phi_M = \phi_H = 0^\circ$ to account for the in-plane isotropy in infinitely large poly-crystalline thin film. the Kittel fitting gives $M_S = 1620\ \text{emu/cm}^3$ and $\gamma = 1.76\ \times 10^7 \text{rad/Oe} \cdot \text{s}$ for poly-crystalline CoFe thin film. Next, the magnonic and phononic response of magnonic mode was obtained in a CoFe NM, using the same TR-MOKE technique (Fig. 5.2(d)). The magnonic mode without considering the magnon-phonon coupling was taken from the Kittel mode fitted in the CoFe thin film in figure 5.2(c), which is plotted with the pink dotted line. Similarly, the phononic mode without the presence of magnon-phonon coupling is presented with the blue dotted lines in figure 5.2(d), which was fit to the equation (4.31). Distinctively noticeable changes in magnetic response were observed in the magnonic

channel in CoFe NM compared to the CoFe thin film. Particularly, a clear anti-crossing was observed at the frequency where the uncoupled magnonic and phononic modes overlap, otherwise. To account for the coupled dynamics of magnon-phonon, two frequencies near the phononic $(1,1)$ crossing shown in the magnonic channel were fit to equation (4.35). The fitting was performed assuming $\rho = 8190\ \mathrm{kg/m^3}$ and $\nu = 0.29$, and using the parameters $M_S = 1620\ \mathrm{emu/cm^3}$ and $\gamma = 1.76\ \times 10^7 \mathrm{rad/Oe \cdot s}$ obtained from the CoFe thin film. The resulting coupled modes were plotted with the solid black solid line in figure 5.2(d), for phononic $(1,1)$ crossing, giving $E = 216.45$ GPa and $\lambda_S = 175.82 \times 10^{-6}$. Please note that such high magnetostriction coefficient possessed in the CoFe material system are in good agreement with the previously reported values [75], suggesting CoFe as a high magnetostrictive material for magnon-phonon coupled system.

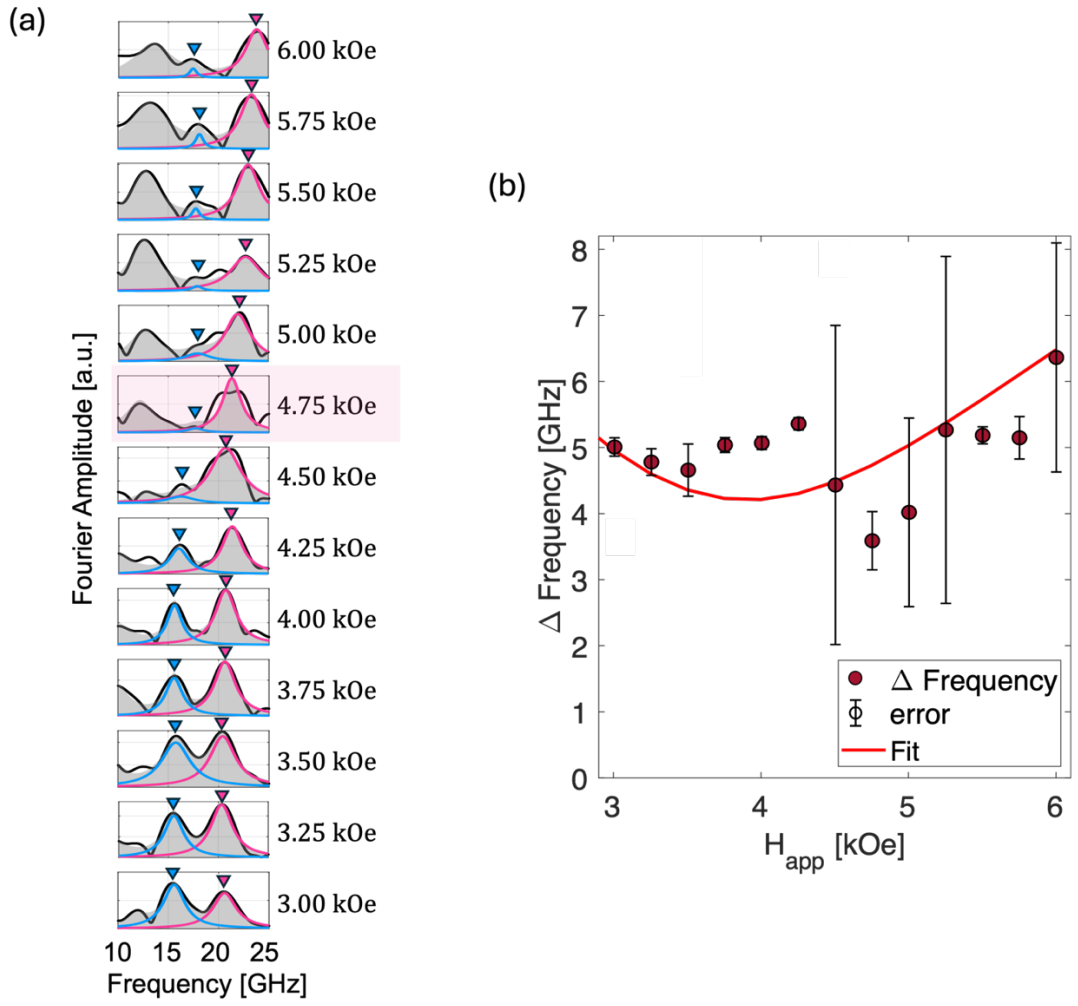

Figure 5.3. (a) Mode splitting of two frequencies at $(1,1)$ crossing, marked with arrows. The Lorentzian was done with three frequencies responsible for $(1,0)$ and $(1,1)$ crossings. Two frequencies fitted for the $(1,1)$ crossing are shown with blue and pink lines with their peaks are marked with arrows. The minimum splitting of two peaks was found at $H_{app} = 4.75\ kOe$ (highlighted). (b) The mode splitting of the CoFe NM at the phononic $(1,1)$ crossing. The red dots are the frequency splitting taken experimentally, and the red solid line represents the fit of frequency splitting. The error bar represents the standard deviation.

5.3. Materials Engineering Perspective (Ni vs. CoFe)

Each of the two coupled frequencies at $(1,1)$ crossing was fit to Lorentzian function to account for damped sinusoidal character of the optical measurement in the time domain (Fig. 5.3(a), pink and blue lines). As clearly shown in the figure 5.3(a), two frequencies are clearly separated at the $(1,1)$ crossing, which is the hallmark of strong coupling. Furthermore, the minimum frequency splitting ($\Delta f_{\min}$) was 3.60 GHz at $\mathrm{H}_{app} = 4.75\ kOe$ (Fig. 5.3(b)), which is over 2.5 times larger splitting than the case with a single Ni nanomagnet reported previously ($\Delta f_{\min,\mathrm{Ni}} = 1.41$ GHz, $(2,0)$ crossing at $\phi_{\mathrm{H}} = 45°$)[98]. Notice that the mode splitting at $(1,1)$ crossing at lower field range $H_{app} \leq 4.5$ kOe was measured larger than the calculated mode splitting. This is because the magnonic mode was coupled to the $(1,0)$ phononic mode, resulting in the splitting of the lower frequency of $(1,1)$ crossing to be pinned near 14.5 GHz.

The quantitative measure of coupling of two quanta, $C = \frac{\Gamma_{\mathrm{C}}^2}{\kappa_{\mathrm{M}}\kappa_{\mathrm{P}}}$ (Eq. 4.28), is calculated to demonstrate strong coupling of magnon-phonon in the CoFe NM. The parameter $\Gamma_{\mathrm{C}} = \Delta f_{\min}/2$ was taken from the coupled magnon-phonon dynamics in the CoFe NM, and $\kappa_{\mathrm{M}} = f_{\mathrm{M}}\alpha_{\mathrm{eff,M}}$ was taken from the uncoupled magnonic dynamics in the CoFe thin film to accommodate the fact that $\alpha_{\mathrm{eff,M}}$ depends on H_{app}, thus needs to be extracted from the applied field where the $\Delta f_{\min}$ was observed. For phonons, $\kappa_{\mathrm{P}} = f_{\mathrm{P}}\alpha_{\mathrm{eff},P}$ was taken from the phononic channel in the CoFe NM at $H_{\mathrm{app}} = 6.00$ kOe away from the H_{app} of center of coupling. For $(1,1)$ crossing, $\alpha_{\mathrm{eff,M}} = 0.0562$ at $f_{\mathrm{M}} = 21.89$ GHz,

giving the intrinsic loss rate for magnon $\kappa_M = 1.23$ GHz, and $\alpha_{eff,P} = 0.0202$ at $f_P = 14.56$ GHz, giving the intrinsic loss rate for phonon $\kappa_P = 0.29$ GHz. With $\Gamma_C = 1.80$ GHz, the cooperativity was calculated $C = 8.93$ (Table 5.1), demonstrating a Strong coupling in a single CoFe NM system, despite the 2.5 times smaller volume in the CoFe NM in this study compared to the previously reported Ni NM. It should be emphasized that this demonstration of greater cooperativity in a twin system with alternative material was a result of a careful engineering by choosing a material that possesses higher magnetostriction coefficient ($\lambda_{S,CoFe} = 178.86 \times 10^{-6}$) than Ni ($\lambda_{S,Ni} = -34 \times 10^{-6}$), based on the previous study[98].

Material	Crossing	Γ_C (GHz)	κ_M (GHz)	κ_P (GHz)	C
Ni	(2,0), 45°	0.71	0.65	0.47	1.65
p-CoFe	(1,1), 0°	1.80	1.23	0.29	8.93

Table 5.1. Summary of coupling strength, loss rate, cooperativity between Ni NM and poly-crystalline CoFe NM.

Material	Γ_C (GHz)	V (μm^3)	N ($\times 10^7$)	C	Γ_0 (Hz)	$\frac{C}{V}$ (μm^{-3})
YIG*	0.136	8.18×10^6	1.2×10^{10}	13,000	0.38	0.001589
Ni	0.71	0.003267	6.35	1.65	8.85×10^4	505.05
p-CoFe	1.80	0.001298	22.6	8.93	11.97×10^4	6,880

Table 5.2. Summary of coupling strength, volume, number of spins, cooperativity, coupling strength for a single Bohr magneton, and cooperativity per unit volume between YIG sphere, Ni NM and poly-crystalline CoFe NM. * Note that the parameters for YIG sphere were taken from magnon-photon coupling.

Given that the coupling strength, Γ_C depends on the number of spins assuming that the spins are collectively precessing at uniform mode[99–101], the coupling strength for a single Bohr magneton and cooperativity per unit volume were calculated (Table 5.2). The coupling strength per Bohr magneton, Γ_0 was given by $\Gamma_0 = \Gamma_C/\sqrt{N}$, where $N = M_S V/\left(\gamma\hbar/2\right)$ is the total number of spins with V being the volume of the magnetic specimen, and $\hbar$ being the Planck constant. To provide more insight on the strength of coupling in magnon-phonon hybrid system, we compared Γ_0 of a YIG sphere where magnon-photon coupling was studied with $C = 13{,}000$ [101]. We noticed that the coupling strength for a single Bohr magneton for both Ni and CoFe were comparable with Ni NM has $\Gamma_{0,\mathrm{Ni}} = 88.5$ kHz and the CoFe NM has $\Gamma_{0,\mathrm{CoFe}} = 119.7$ kHz, showing merely improved 1.35 times stronger coupling per Bohr magneton. The reason why the coupling strength per Bohr magneton didn't show as large difference, despite the small size (small number of spins) in CoFe is due to a higher saturation magnetization in CoFe ($M_{\mathrm{S,CoFe}} = 1620\ \mathrm{emu/cm^3}$) compared to Ni ($M_{\mathrm{S,Ni}} = 203\ \mathrm{emu/cm^3}$). However, $\Gamma_{0,\mathrm{CoFe}}$ was 315,000 times larger when compared to a magnon-photon coupled system in a YIG sphere. Moreover, cooperativity per $\mu\mathrm{m}^3$ (C/V) was $6880.24\ \mu\mathrm{m}^{-3}$ for the CoFe NM, which is more than an order of magnitude larger

($\times 13.62$) than calculated in the Ni NM system, and 6 orders of magnitude larger ($\times 4{,}330{,}000$) than calculated in the magnon-photon coupled system. Due to high magnetostriction coefficient and higher saturation magnetization in CoFe system, a poly-crystalline CoFe nanomagnet possesses strong coupling in the nanoscale regime. This study suggests that the CoFe-based nanomagnet as a great candidate for the magnonic hybrid quantum system when coupled to phonons.

Chapter 6. Magnetization Dynamics in Single-crystalline CoFe and CoFe/CMS Thin Films

6.1. Introduction

Epitaxially grown magnetic multilayers play a key role in spintronic devices[102–104], where their layered structures are designed to provide precise control over the electronic and magnetic properties for applications such as magnetic random access memory (MRAM), sensors, and spin transistors. Many of these devices rely on multilayer magnetic tunnel junctions (MTJs)[102–113] in which high spin polarization is essential to maximize the tunnel magnetoresistance (TMR) and, thus optimize device performance. Recently, Heusler alloys have received increasing attention for this purpose due to their half-metallic nature[114–119] and high Curie temperature[120–122], and Co_2MnSi (CMS) has emerged as one of the most promising candidates[123,124]. CMS can crystallize in the ordered $L2_1$ crystal structure which has been theoretically shown to possess nearly-zero spin down density of states at the Fermi energy due to Slater-Pauli behavior[125], and high spin polarization has been found in this phase[126]. By controlling the annealing temperature, CMS alloys can also crystallize in the $B2$ phase, which is

half-metallic as well[127]. Indeed, excellent static behavior, including a TMR ratio of 570% at low temperature in a CMS/AlO/CMS structure[128] and 753% in a CMS/MgO/CoFe[123] have been demonstrated. The crucially important interface quality between CMS and the tunneling oxide can be improved with a thin intermediate layer based on cobalt iron (e.g. CoFeB), resulting in TMR ratios as high as 222% at room temperature[124]. In addition to MTJ applications, Heusler alloys are also promising materials for spintronic THz emitters[129,130]. Moreover, multilayer structures with adjacent CoFe and CMS layers can also be used to build novel spintronic devices, such as THz sources based on nonlinear magnon-magnon interactions[131].

It is, therefore, of great interest to investigate the magnetic properties of CMS in structures in which it is surrounded by another magnetic layer. In addition to static properties such as TMR, sound knowledge and understanding of the dynamic properties are also important as it determines the time-dependent device behavior and can reveal important material parameters such as the Gilbert damping parameter. Indeed, the suppression of spin-flip processes in half metals promises low damping,[132–134] and damping values as low as $< 8 \times 10^{-4}$ have been reported in Co_2FeAl films[135] and Co_2MnSi films[136].

Magnetization dynamics can be measured with different techniques. One of them is time-resolved magneto-optic Kerr effect (TR-MOKE) microscopy in which magnetic materials are non-invasively perturbed by a short laser pulse, and their dynamic response is analyzed with a second, delayed pulse.[66] Liu et al. have previously used this technique to analyze the magnetization dynamics of a thick (30 nm) CMS film grown

with a non-magnetic Cr buffer layer on MgO substrate and annealed at different temperatures[137]. They measured the precession frequency of the CMS film at low applied magnetic fields (below 1 kOe) and as a function of the azimuthal angle ϕ between the applied field and the [110] crystalline direction of the film. A fourfold symmetric dependence of both the precession frequency and damping as a function of ϕ was observed, caused by the magnetocrystalline anisotropy present in this cubic structure.

Here, we expand on these studies by investigating the magnetization dynamics of an epitaxial CMS layer that is part of a MgO/CoFe/CMS magnetic bilayer sequence that can act as a functional segment in future spintronic devices as discussed above. The part of this work was published in ref [138]. Using external magnetic fields applied at various polar and azimuthal angles, we extract the magnetization dynamics all the way up to the high field limit where inhomogeneous broadening mechanisms disappear, and the intrinsic Gilbert damping of the material can be determined.[139] Additional comparison with the dynamics of a CoFe film reveals that the dynamic response remains determined by the geometry of the CMS crystal anisotropy and is not affected by the CoFe crystal geometry. We also find that the angular dependence of the damping parameter disappears in the high magnetic fields limit.

This work (materials synthesis and x-ray characterization, and their analysis) was done and written in close collaboration with David Lederman group in the physics department and the materials science and engineering initiative at University of California Santa Cruz.

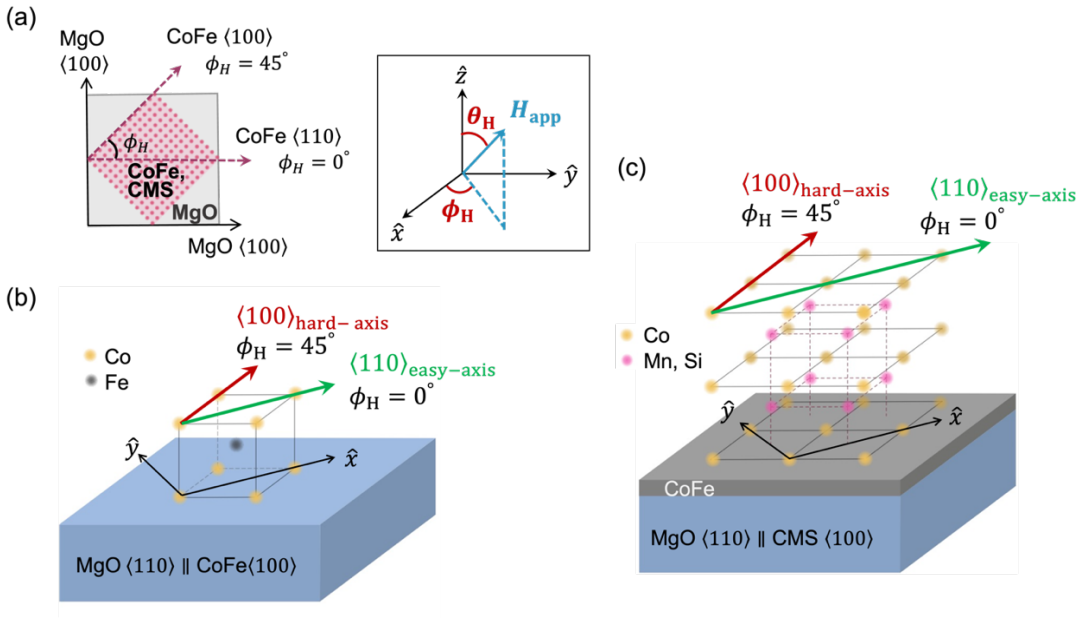

Figure 6.1. Sample geometry. (a) Top-down view of CoFe and CMS films with respect to the MgO film and the azimuthal angles. The CoFe and CMS ⟨110⟩ directions are parallel to the MgO ⟨001⟩ direction and the x-axis. Inset shows the geometry of the applied magnetic field with respect to the cartesian coordinate and the corresponding polar coordinate. (b) The unit cell of magnetic single layer CoFe film on MgO substrate. The magnetic easy-axis (green arrow) of the CoFe film corresponds to the ⟨110⟩ direction and $\phi_H = 0^\circ$, and the magnetic hard-axis (red arrow) of the CoFe film corresponds to the ⟨100⟩ direction and $\phi_H = 45^\circ$. (c) The unit cell of CMS film grown on top of the CoFe film and the MgO substrate. The magnetic easy-axis (green arrow) of the CMS film corresponds to the ⟨110⟩ direction and $\phi_H = 0^\circ$, and the magnetic hard-axis (red arrow) of the CMS film corresponds to the ⟨100⟩ direction and $\phi_H = 45^\circ$.[138]

6.2. Sample preparation and experimental procedure

Two different sample types were fabricated for this study. A reference sample, consisting of a single, 10.8 nm thick CoFe film was prepared on an MgO [001] substrate (see Fig. 6.1b). The MgO substrate was annealed at 800 ℃ at 100 Torr in an O_2 gaseous environment for 100 minutes, then the temperature was lowered to 700 ℃ and the substrate was left in a vacuum. The substrate was then cooled down to 400 ℃ and a thin layer of MgO was deposited by pulsed laser deposition (PLD) to improve the surface quality and to promote better crystallinity of the films. After the surface treatment, the substrate was transferred to an RF-Sputtering chamber while kept in a vacuum. A $Co_{50}Fe_{50}$ target was used to sputter a 10.8 nm-thick CoFe film at room temperature, followed by annealing (500 ℃ for 30 min) and cooling (400 ℃ for 1 hour) steps. The second sample consisted of a CoFe (1.7 nm) / CMS (7.0 nm) bilayer film (Fig. 6.1c). The thin 1.7 nm CoFe film was prepared on a separate MgO [001] substrate using the same protocol. Additionally, an RF sputtering step to deposit 7.0 nm CMS film at room temperature was performed, followed by annealing for 30 min at 400 ℃.

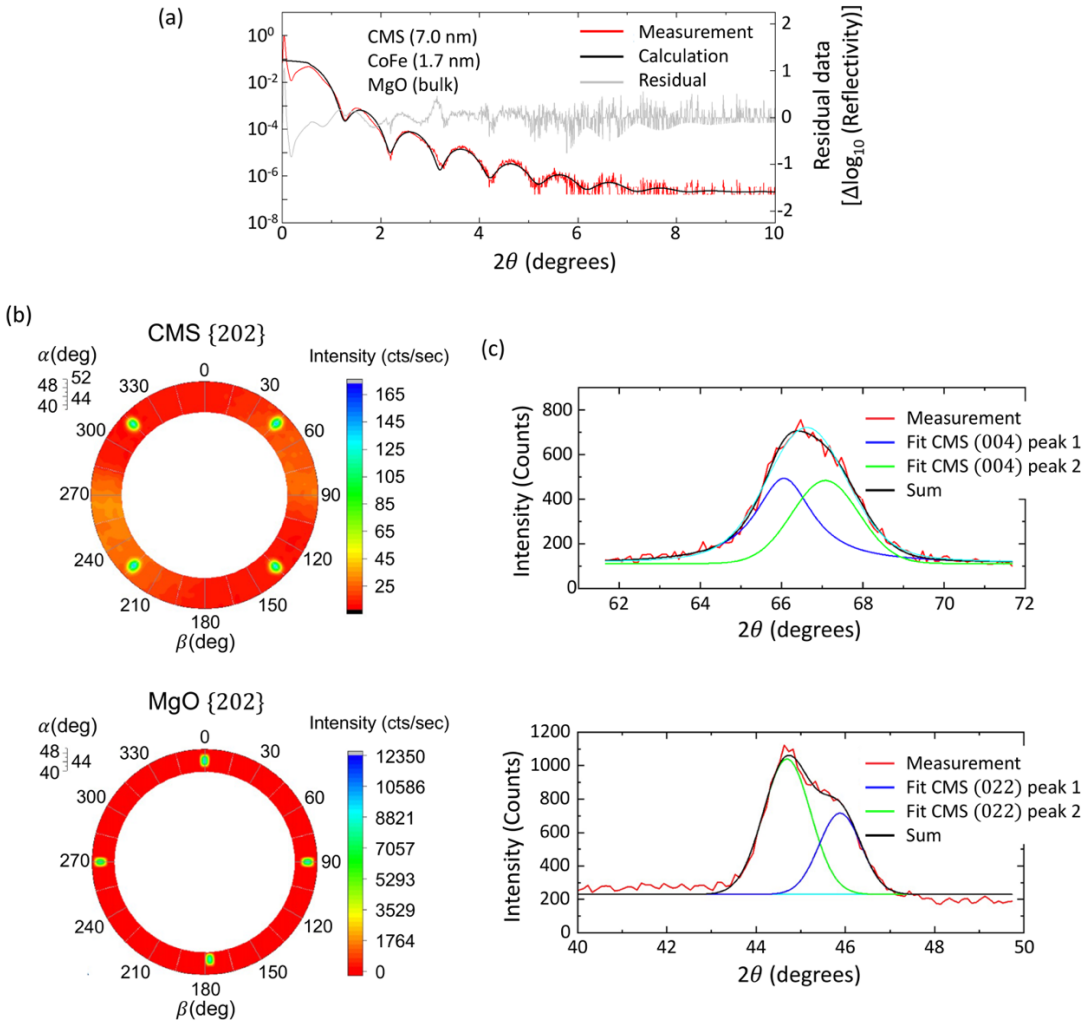

Figure 6.2. X-ray analysis of CoFe/CMS magnetic bilayer film. (a) X-ray reflectivity to measure the thickness of the CoFe/CMS layers. The red curve represents the measured data while the black curve is a fit to an optical scattering model with 1.69 nm of CoFe, 6.95 nm of CMS, and 0.3 nm of interface roughness at each interface. The gray curve is the residual [$\log_{10}$ (measured data) – $\log_{10}$ (model calculation)]. (b) Pole figure of the CMS {202} peaks and the MgO substrate {202} peaks about the surface normal, corresponding to the MgO [001] direction, showing the alignment of the in-

plane CMS [100] and the MgO [110] crystallographic directions. (c) Top: X-ray diffraction $\theta - 2\theta$ scan data (red) obtained with the scattering vector $\vec{q}$ along the direction perpendicular to the film's plane. Bottom: $\theta - 2\theta$ scan obtained with $\vec{q}$ along the CMS [022] direction with Gaussian lineshape fits. Gaussian peaks were fit to the data (green, blue), with the black curve being the sum of the two peaks. [138]

X-ray diffraction experiments using a parallel-beam configuration, an incoming double-bounce Ge monochromator, and Cu Kα1 radiation ($\lambda = 0.15406$ nm) were used to study the bilayer sample's structure. The layer thickness parameters of the CoFe / CMS bilayer film were determined from X-ray reflectivity, confirming a thickness of 1.7 nm for the CoFe layer, and 7.0 nm for the CMS layer with sharp interfaces of 0.3 nm roughness [Fig. 6.2(a)]. The epitaxial nature of the CMS was verified by taking pole figure scans of the CMS $\{202\}$ peaks [Fig. 6.2(b)]. The pole figures show that the CMS $[100]$ direction is indeed parallel to the MgO $[110]$ direction, as depicted in Fig. 6.1.

High-angle X-ray diffraction scans about CMS (004) and CMS (022) revealed that the CMS layer was oriented along its $[001]$ directions, as shown in the top graph of Fig. 6.2(c). The CMS (004) diffraction was composed of two peaks at $2\theta = 66.1°$and $2\theta = 67.1°$, correspondingly labeled peak 1 and peak 2 in Fig. 6.2(c). The (022) reflection was also composed of two peaks, located at $2\theta = 44.7°$ and $2\theta = 45.88°$, labeled peak 2 and peak 1, respectively. We believe this is due to a sudden relaxation of the crystal structure as it grows, probably at a thickness smaller than 3.5 nm given

the areas of the two peaks. Assuming that one of the crystals corresponds to peak 1 of the (004) reflection and peak 1 of the (022) reflection, we obtain a lattice constant out-of-plane equal to $d_{o,CMS1} = 0.565$ nm and an in-plane lattice constant of $d_{i,CMS1} = 0.553$ nm. For the crystal corresponding to peak 2, the lattice constant out-of-plane is $d_{o,CMS2} = 0.558$ nm, and the in-plane lattice constant is $d_{i,CMS2} = 0.591$ nm, with an uncertainty of ± 0.001 nm. The bulk CMS compound has a lattice constant of 0.5654 nm[140], and therefore it is likely that the peak 1 of CMS (004) and CMS (022) corresponds to a relatively unstrained CMS layer, while the peak 2 corresponds to a highly strained CMS layer. Indeed, the in-plane lattice constant corresponding to the in-plane (110) planes for the strained layer is $d_{i,CMS2}/\sqrt{2} = 0.418$ nm which is close to the (001) lattice constant of MgO of 0.421 nm. In other words, initially, the film attempts to grow epitaxially with the MgO substrate (peak 2), causing a large amount of tensile strain (approximately 6%), and then releases its strain after less than 3.5 nm to obtain an almost cubic structure consistent with the bulk compound (peak 1). The CoFe seed layer plays a key role in achieving this epitaxy; CMS films grown directly on MgO were not epitaxial but grew with a preferential (110) orientation (data not shown). The CoFe layer in this sample is too thin to be measured with our X-ray apparatus, however.

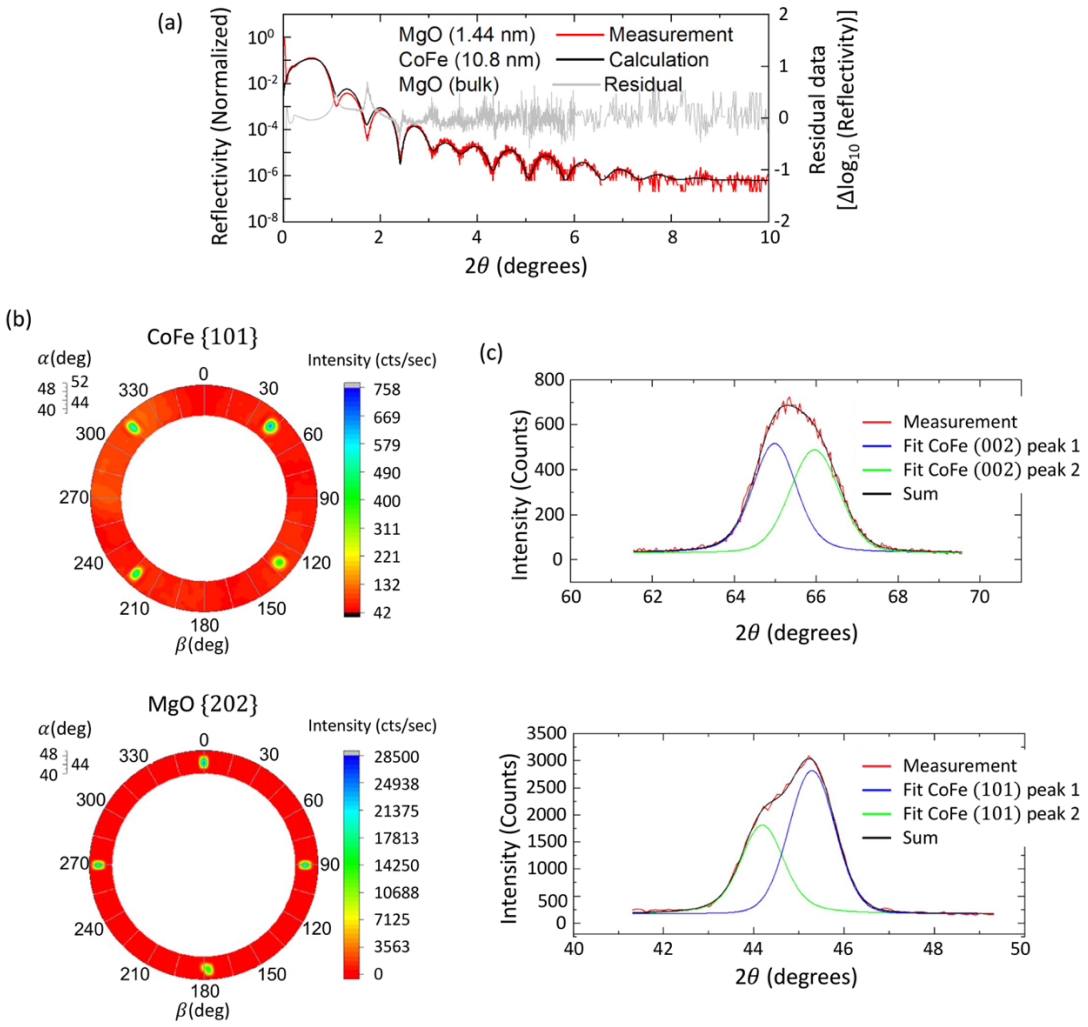

Figure 6.3. X-ray analysis of CoFe reference magnetic film. (a) X-ray reflectivity to measure the thickness of the CoFe layer. The red curve represents the measured data while the black curve is a fit to an optical scattering model with 10.8 nm of CoFe and 1.4 nm of MgO capping layer, and 0.5 nm of interface roughness at each interface. The gray curve is the residual [$\log_{10}$ (measured data) – $\log_{10}$ (model calculation)]. (b) Pole figure of the CoFe {101} peaks and the MgO substrate {202} peaks about the surface normal, corresponding to the MgO [001] direction, showing the alignment of the in-

plane CoFe [100] and the MgO [110] crystallographic directions. (c) Top: X-ray diffraction $\theta - 2\theta$ scan data (red) obtained with the scattering vector $\vec{q}$ along the direction perpendicular to the film's plane. Bottom: $\theta - 2\theta$ scan obtained with $\vec{q}$ along the CoFe [101] direction with Gaussian lineshape fits. Gaussian peaks were fit to the data (green, blue), with the black curve being the sum of the two peaks. [138]

Interestingly, a similar effect is found in the CoFe thin film. This film was capped with a thin layer of MgO to prevent oxidation. The X-ray analysis is shown in Fig. 6.3. The X-ray reflectivity shown in Fig. 6.3(a) indicated that the CoFe layer was 10.8 nm thick and that the MgO [110] axis is along the in-plane CoFe [100] axis, in agreement with literature[120]. The pole figures shown in Fig. 3(b) confirm that the CoFe film is epitaxial with the in-plane CoFe [100] direction parallel to the MgO [110] direction. Fig. 6.3(c) shows the high-angle X-ray scans about the CoFe (002) and CoFe (101). Using the same analysis as the one described above for the CMS film, we obtain that the out-of-plane lattice constants for the crystal layer that corresponds to the peak 1 are $d_{o,CoFe1} = 0.287$ nm and the in-plane lattice constant of $d_{i,CoFe1} = 0.279$ nm. For the second set of peaks (peak 2) we have out-of-plane lattice constant of $d_{o,CoFe2} = 0.283$ nm and in-plane lattice constant of $d_{i,CoFe2} = 0.297$ nm. The highly strained layer corresponding to peaks 2 results in an in-plane lattice constant of $d_{i,CoFe2}/\sqrt{2} = 0.420$ nm, also consistent with the epitaxial growth on MgO as described in Fig. 6.1.

There are two commonly observed phases in epitaxially grown CMS crystals - $L2_1$ and $B2$ phases - that are known to exhibit half-metallic behavior[127]. Unlike the $L2_1$ phase where the Mn and Si atoms are highly ordered, Mn and Si atoms are randomly located at lattice points in the cubic unit cell in the $B2$ phase. To determine which phase of CMS was grown, we attempted to obtain pole figures and $\theta - 2\theta$ scans about the expected positions of the CMS (111) peak, but we were unable to find such a peak. Because the characteristic (111) peak of the $L2_1$ phase was not observed in the XRD scan, it is likely that the epitaxial CMS film possessed the $B2$ structure. The magnetization dynamics of these samples were then analyzed using the TR-MOKE technique described in chapter 3.

6.3. Results and Discussion

To establish a reference for the bilayer structure and to potentially separate the behavior of the CoFe layer from that of the CMS film, we first analyzed the magnetization dynamics of the epitaxially grown CoFe film. To this end, an external magnetic field of H_{app} = 5 kOe was applied at multiple polar angles (θ, angle with respect to the z-axis), and various azimuthal angles (ϕ_{H}, angle with respect to the x-axis in the x-y plane) (see inset in Fig. 6.1(a)). Specifically, polar angles of $\theta_{\text{H}} = 30^{\circ}, 45^{\circ}$ and 55° were chosen and the azimuthal angle was scanned in each case between $-5^{\circ} \leq \phi_{\text{H}} \leq 85^{\circ}$ to probe the full fourfold symmetry in the BCC structure. Figure 6.1 (b) shows the unit cell of epitaxially grown CoFe on MgO substrate. For the CoFe grown on an MgO

⟨001⟩ substrate used in this study, the ⟨100⟩ easy axis coincides with the ⟨110⟩ direction of MgO as discussed earlier.

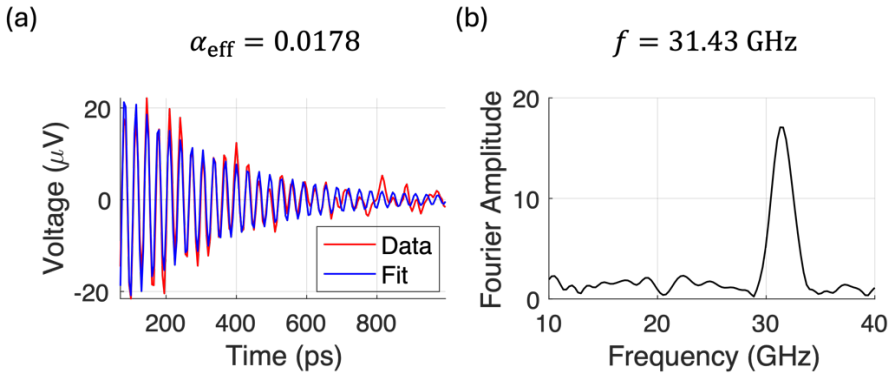

Figure 6.4. (a) Time trace and (b) its Fourier transformed data of a magnetic single layer CoFe thin film to illustrate the data analysis. The time trace data was taken at $H_{app} = 5\ kOe, \theta_H = 55^{\circ}, \phi_H = 5^{\circ}$.

The time-dependent magnetization dynamics were extracted from the difference signal of the balanced photodetectors and recorded via LabVIEW software (Fig. 6.4). After subtraction of an exponentially decaying thermal background, the Kerr rotation (θ_{K}) which is proportional to the magnetization change in the z direction, was fit to the equation (3.1) to extract the magnetic precession frequency and the effective damping parameter.[68,141]

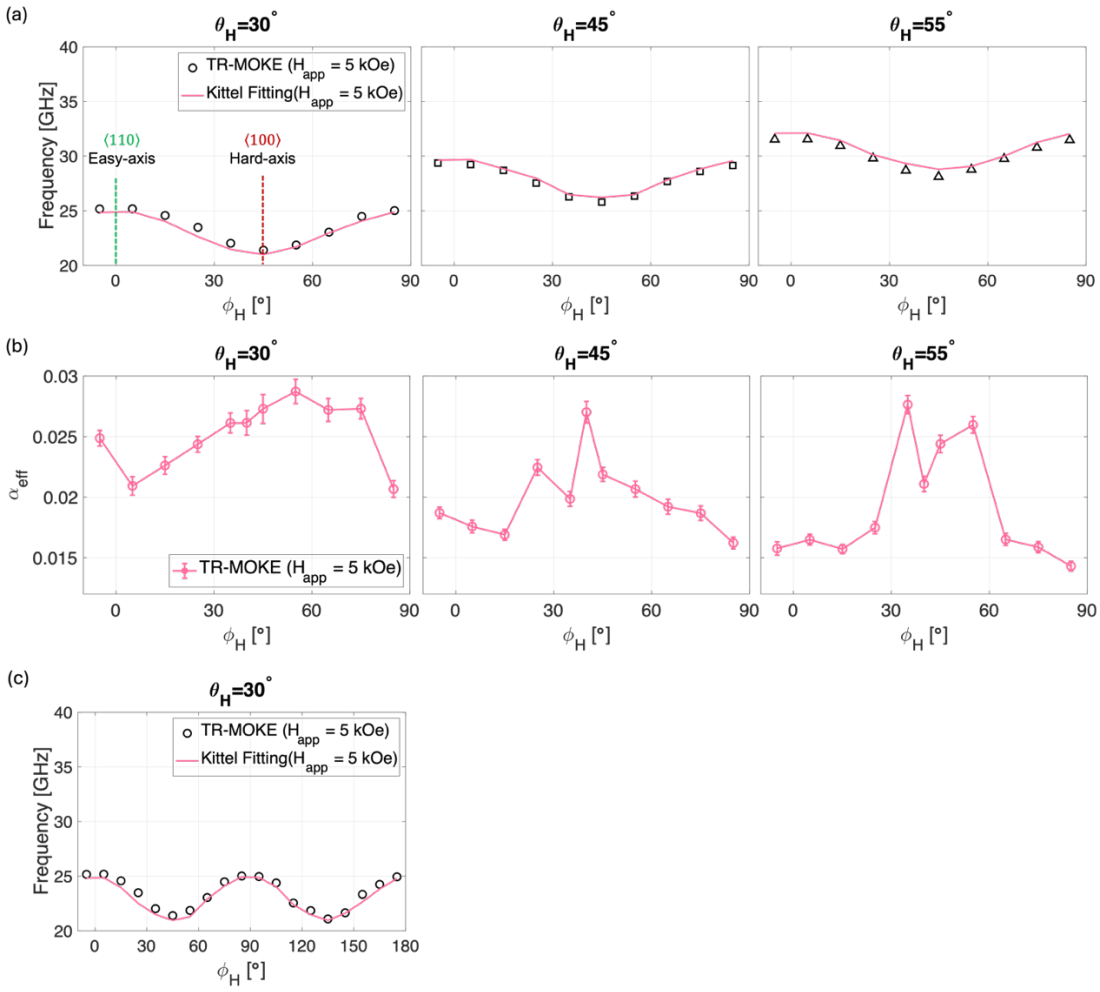

Figure 6.5. (a, c) Precession frequency of a single magnetic CoFe film at various applied magnetic fields. The scatter plots are TR-MOKE experimental data and the line plots show Kittel fitting. (b) Experimentally taken effective damping parameter of the corresponding single magnetic CoFe film at various applied magnetic fields. The TR-MOKE data in (a) and (b) were taken at a constant magnetic field (5 kOe) applied at three polar angles ($\theta_H = 30^{\circ}, 45^{\circ}$ and 55° from left to right), while sweeping the azimuthal angles from $\phi_H = -5^{\circ}$ to 85° to probe the fourfold symmetry of the cubic crystal. The red dashed (green dotted) lines are guides to the eye to denote when the in-

plane component of the applied magnetic field is along the magnetic hard (easy)-axis. The TR-MOKE data in (c) was taken at $H_{app} = 5\ kOe$ and $\theta_H = 30^{\circ}$, while the azimuthal angles were wept from $\phi_H = -5^{\circ}$ to 175°. [138]

Figure 6.5(a) shows the dependence of the magnetization precession frequency as a function of azimuthal angles for each of the three different polar angles. The frequency response depends strongly on ϕ_{H} and is symmetrically distributed around $\phi_{\mathrm{H}} = 45^{\circ}$, reflecting the fourfold symmetry character of the BCC crystal structure that originates from the magnetocrystalline anisotropy. At $\phi_{\mathrm{H}} = 0^{\circ}$ and 90°, the projection of the magnetic field in the x-y plane is applied along the magnetic hard axis ($\langle 110 \rangle$, Fig. 6.1(b)), and the lowest frequency was observed. At $\phi_{\mathrm{H}} = 45^{\circ}$, the in-plane component of the magnetic field is applied along the magnetic easy axis ($\langle 100 \rangle$ orientation, Fig. 6.1(b)), and the highest precession frequency was observed. The magnetic field was also applied and scanned including the face diagonal ($\theta_{\mathrm{H}} = 45^{\circ}$, $\phi_{\mathrm{H}} = 45^{\circ}$) and body diagonal ($\theta_{\mathrm{H}} = 55^{\circ}$, $\phi_{\mathrm{H}} = 0^{\circ}, 90^{\circ}$) directions of the CoFe structure. Qualitatively similar frequency responses were consistently observed for all applied polar angles. Next, the damping was extracted from the same time data trace used for the frequency analysis for the same range of applied magnetic fields [Fig. 6.5(b)]. Again, the fourfold symmetry corresponding to the magnetocrystalline anisotropy was also observed in the effective damping parameter. However, the effective damping parameter was highest when the in-plane component of magnetic field was applied along the hard axis ($\phi_{\mathrm{H}} =$

$0^{\circ}, 90^{\circ}$), and lowest when the in-plane component of magnetic field was applied along the easy axis ($\phi_{\mathrm{H}} = 45^{\circ}$).

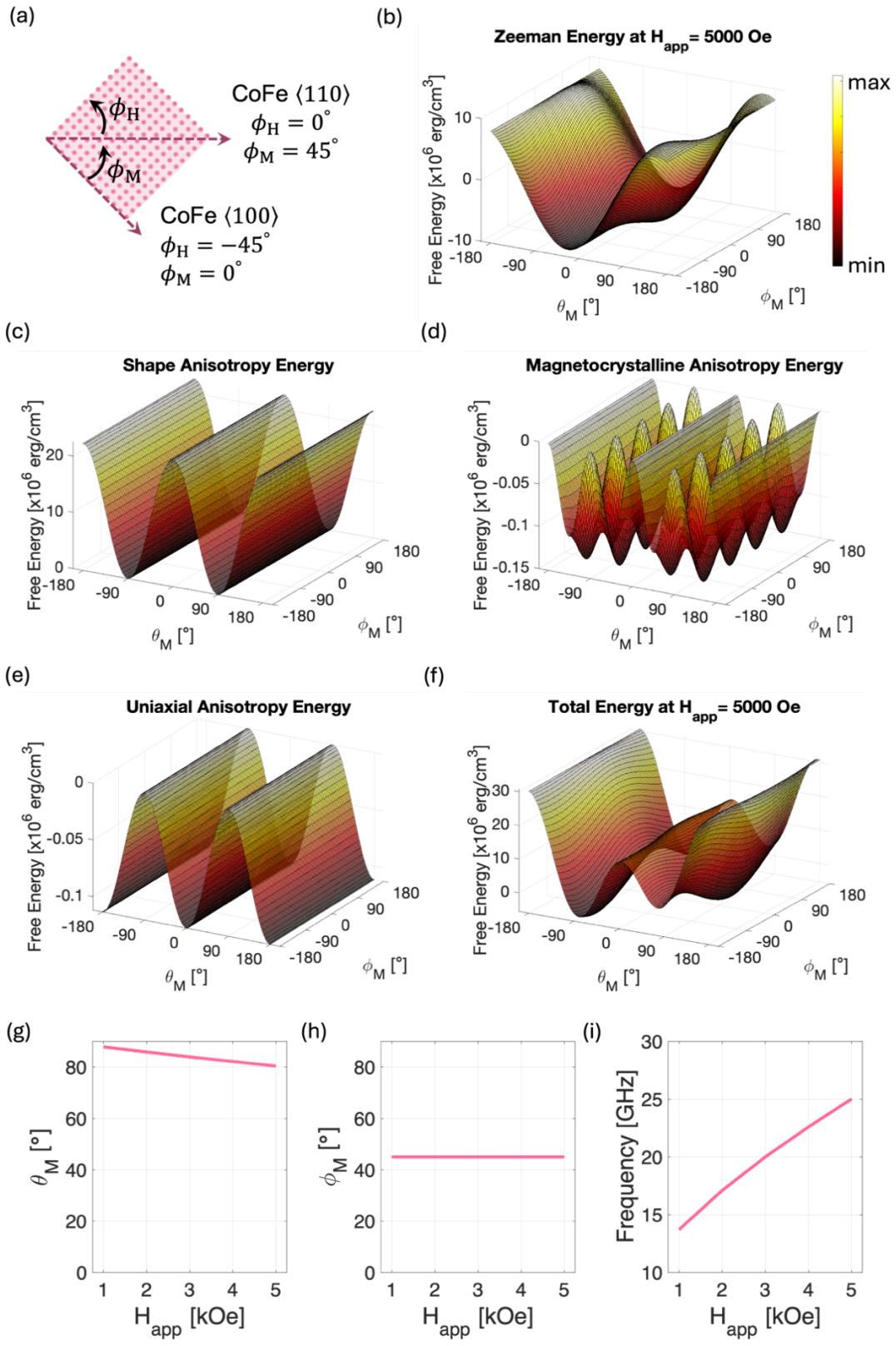
(a)
ϕ_H
ϕ_M
CoFe ⟨110⟩
$\phi_H = 0^\circ$
$\phi_M = 45^\circ$
CoFe ⟨100⟩
$\phi_H = -45^\circ$
$\phi_M = 0^\circ$
(b)
Zeeman Energy at H_app = 5000 Oe
Free Energy [x10^6 erg/cm^3]
max
min
θ_M [°]
ϕ_M [°]
(c)
Shape Anisotropy Energy
(d)
Magnetocrystalline Anisotropy Energy
(e)
Uniaxial Anisotropy Energy
(f)
Total Energy at H_app = 5000 Oe
(g)
θ_M [°]
H_app [kOe]
(h)
ϕ_M [°]
H_app [kOe]
(i)
Frequency [GHz]
H_app [kOe]

Figure 6.6. (a) Schematics of azimuthal angles of applied magnetic field and magnetization. $\phi_M = 0°$ is defined along one of the principal axes of cubic crystals ($\langle 100 \rangle$ in this work), whereas $\phi_H = 0°$ is defined diagonal to the cubic crystals ($\langle 110 \rangle$ in this work) along the $\langle 100 \rangle$ of MgO substrate. The polar angles of applied magnetic field and magnetization are defined at $\theta_{H,M} = 0°$ aligning with the z-axis. In this example in figure 6.6, the applied magnetic field is fixed at $\theta_H = 30°$ and $\phi_H = 0°$, while the amplitude of the magnetic field was swept from $1\ kOe \leq H_{app} \leq 5\ kOe$. (b-e) (b) Zeeman free energy, (c) Shape anisotropy free energy, (d) Magnetocrystalline anisotropy free energy, and (e) Uniaxial anisotropy free energy at various magnetization directions. (f) Total free energy at various magnetization directions. The local minimum free energy was found at $\theta_M = 80.43°$ and $\phi_M = 45.00°$ at $H_{app} = 5\ kOe$. Note that the free energies in (b-f) are not normalized to M_S. (g) θ_M and (h) ϕ_M at various applied magnetic fields. (i) The corresponding Kittel mode at various applied magnetic field.

In order to explain the anisotropy response of single-crystalline CoFe film, magnetocrystalline energy and uniaxial energy terms were added to the free energy of magnetic film.

$$G_{\text{total}} = G_{\text{Zeeman}} + G_{\text{Shape}} + G_{\text{MagCrys}} + G_{\text{Uni}}$$

$$= \vec{\boldsymbol{H}}_{\text{app}} \cdot \vec{\boldsymbol{m}} + \frac{1}{2} N_Z M_S m_Z^2 + \frac{K_1}{M_S}[(\alpha_1\alpha_2)^2 + (\alpha_2\alpha_3)^2 + (\alpha_3\alpha_1)^2] - \frac{K_U}{M_S}\alpha_3^2, \quad (6.1)$$

where G_{Zeeman} denotes the Zeeman energy in the first term, G_{Shape} describes the shape anisotropy energy in the second term, G_{MagCrys} describes the magnetocrystalline anisotropy energy in the third term and G_{Uni} describes the out-of-plane uniaxial anisotropy written in the last term, where G is normalized by M_{S}. Note that the in-plane uniaxial anisotropy is dropped in this equation since the in-plane uniaxial anisotropy was merely noticeable in our sample (Fig. 6.5(c)). For simplicity, the coordinate transformation from the Cartesian coordinate to magnetization coordinate of $(1, 2, 3)$ was taken as described in the chapter 2. The magnetization points along the local minimum energy at equilibrium, thus, the polar and azimuthal angle of magnetization at equilibrium are found at

$$\frac{\partial G_{\mathrm{total}}}{\partial \theta_{\mathrm{M}}} = 0, \tag{6.2}$$

$$\frac{\partial G_{\mathrm{total}}}{\partial \phi_{\mathrm{M}}} = 0.$$

To provide more intuition on energy competition between four energy terms, the free energy at various magnetization angles ($-180^{\circ} \leq \theta_{\mathrm{M}} \leq 180^{\circ}$ and $-180^{\circ} \leq \phi_{\mathrm{M}} \leq 180^{\circ}$) at $H_{\mathrm{app}} = 5$ kOe are plotted in figure 6.6(b-f). The Zeeman energy shows the local minimum energy of magnetization overlaps with the applied magnetic fields at $\theta_{\mathrm{M}} = 30^{\circ}$ and $\phi_{\mathrm{M}} = 45^{\circ}$ (Fig. 6(b)). Due to the infinitely large thin film, the shape anisotropy energy provides local minimum energy along the in-plane direction of the film at $\theta_{\mathrm{M}} = 90^{\circ}$, regardless of azimuthal angle of magnetization (Fig. 6(c)). The magnetocrystalline anisotropy energy is locally minimum along the diagonal direction of the cubic crystal at $\theta_{\mathrm{M}} = 45^{\circ}$ and $\phi_{\mathrm{M}} = 45^{\circ}$ (Fig. 6(d)). The uniaxial anisotropy

energy is locally minimum at $\theta_{\mathrm{M}} = 0°$, regardless of azimuthal angle of magnetization (Fig. 6(e)). Finally, by adding all 4 energy terms, the total energy provides the local minimum at $\theta_M = 80.43°$ and $\phi_M = 45.00°$ at $H_{app} = 5\ kO\mathrm{e}$ (Fig. 6(f-h)). It is worth noting that the θ_M tends to align in-plane direction the applied magnetic field is lower, showing that the shape anisotropy energy is dominant. However, as the applied magnetic field is increased, the θ_M tends to align closer to the θ_{H} showing that the Zeeman energy starts to play as a dominant energy term.

The corresponding Kittel frequency was then calculated using the formula given in equation (2.62). and the calculated Kittel mode at $\theta_{\mathrm{H}} = 30°$ and $\phi_{\mathrm{H}} = 0°$ was shown in figure 6.6 (i). Using the derived Kittel formula, the magnetic parameters of $M_{\mathrm{S}} = 1896\ \mathrm{emu/cm^3}$, $\gamma = 1.81 \times 10^7 \mathrm{rad/Oe \cdot s}$, $K_1 = -4.21 \times 10^5 \mathrm{erg/cm^3}$, and $K_{\mathrm{U}} = 1.12 \times 10^5 \mathrm{erg/cm^3}$ were obtained, showing good agreement with the reported values[142]

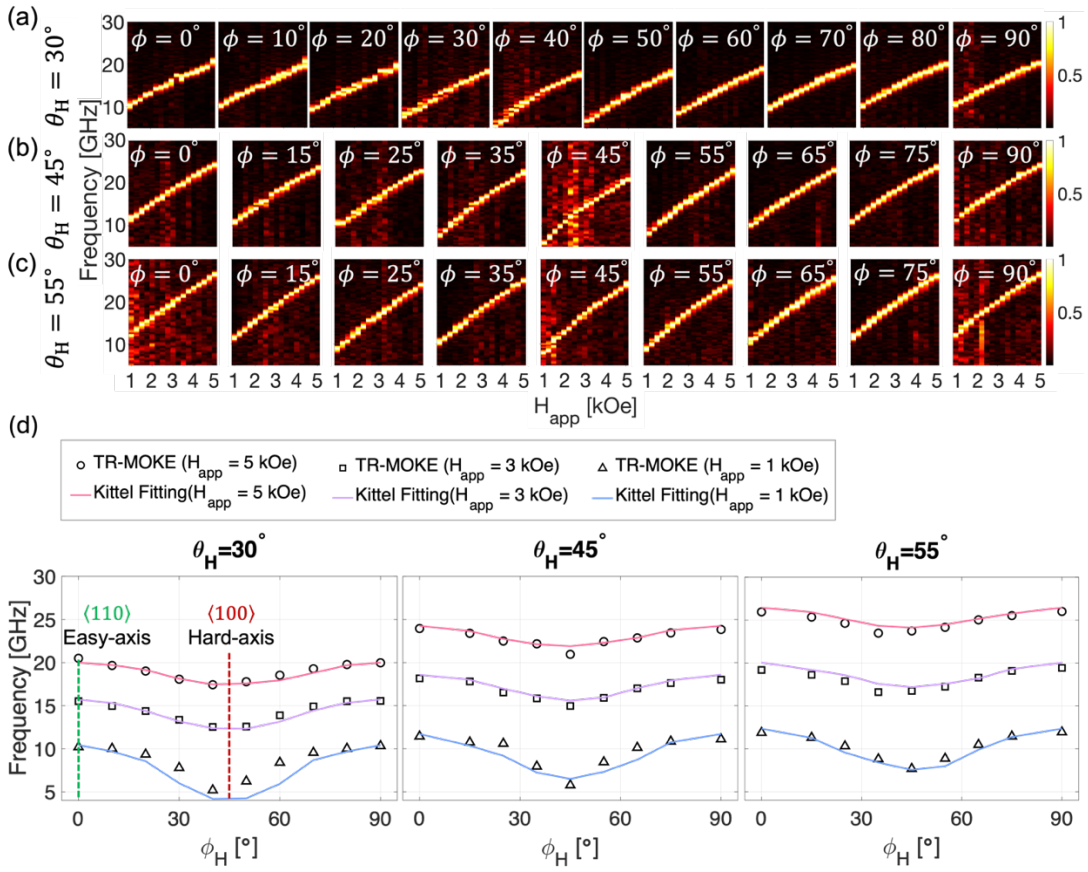

Figure 6.7. (a-c) Frequency response of CoFe/CMS magnetic bilayer at various applied magnetic fields. The magnetic field was applied at three polar angles θ_H = (a) 30°, (b) 45° and (c) 55°, and various azimuthal angles from $\phi_H = 0^\circ$ to 90°(left to right) while sweeping the intensity of applied magnetic field from 1 kOe to 5 kOe. (d) Frequency response of (a-c) taken at $H_{app} = 1\ kOe$ (triangles), 3 kOe (squares) and 5 kOe (circles). The scatter plots are taken from TR-MOKE experimental data and the line plots are taken from the Kittel fitting. The green (red) dashed lines are guides to the eye to denote where the in-plane component of applied magnetic field is along the magnetic easy (hard) axis. [138]

After having established the dynamic behavior of a single CoFe layer, we investigated the magnetization dynamics in view of the CoFe/CMS crystalline structure. Figures 6.7(a-c) show field scans of the frequency response of the CoFe/CMS bilayer for the three different polar angles. As in Fig. 6.5(b), each plot in the figure corresponds to 17 applied field values ranging from 1 kOe to 5 kOe in 0.25 kOe steps. As in the case of the single layer CoFe film, the frequency response was symmetrically centered around at $\phi_{\mathrm{H}} = 45^{\circ}$ [Fig. 6.7(d), shown for three representative applied field values], representing the magnetocrystalline anisotropy of fourfold symmetry character exhibited in cubic crystals. The azimuthal scan shows a frequency maximum when the in-plane component of the magnetic field was applied along the $\langle 110 \rangle$ direction, and a minimum along the $\langle 100 \rangle$ direction, indicating that the epitaxially grown CMS film has the $\langle 110 \rangle$ direction as a magnetic easy-axis [Fig. 6.1(c)], and the $\langle 100 \rangle$ direction corresponds to the magnetic hard-axis [Fig. 6.1(c)]. In order to see if the magnetic response of CoFe/CMS bilayer is affected by the CoFe seed layer, the frequency response was fitted to the Kittel formula. The fitted magnetic properties of CoFe/CMS bilayer was obtained by $M_{\mathrm{S}} = 1090\ \mathrm{emu/cm^3}$, $\gamma = 1.88 \times 10^7 \mathrm{rad/Oe \cdot s}$, $K_1 = -2.03 \times 10^5 \mathrm{erg/cm^3}$, and $K_{\mathrm{U}} = 1.00 \times 10^5 \mathrm{erg/cm^3}$. The fitted M_{S} value was found close to that of CMS[137], suggesting that the frequency response of CoFe/CMS bilayer is dominated by CMS layer and merely influenced by CoFe due to its small thickness.

Samples	γ [rad/Oe · s]	M_S[emu /cm^3]	K_1[emu /cm^3]	K_{Uni}[emu /cm^3]
CoFe	1.81×10^7	1896	-4.21×10^5	1.12×10^5
CoFe/CMS	1.88×10^7	1090	-2.03×10^5	1.00×10^5
CoFe Ref.[142]	1.90×10^7	1966	-4.72×10^5	1.19×10^5
CMS Ref.[137]	1.73×10^7	1000	-0.46×10^5	-

Table 6.2. The summary of fitted magnetic parameter of CoFe and CoFe/CMS bilayer from this work and the references.

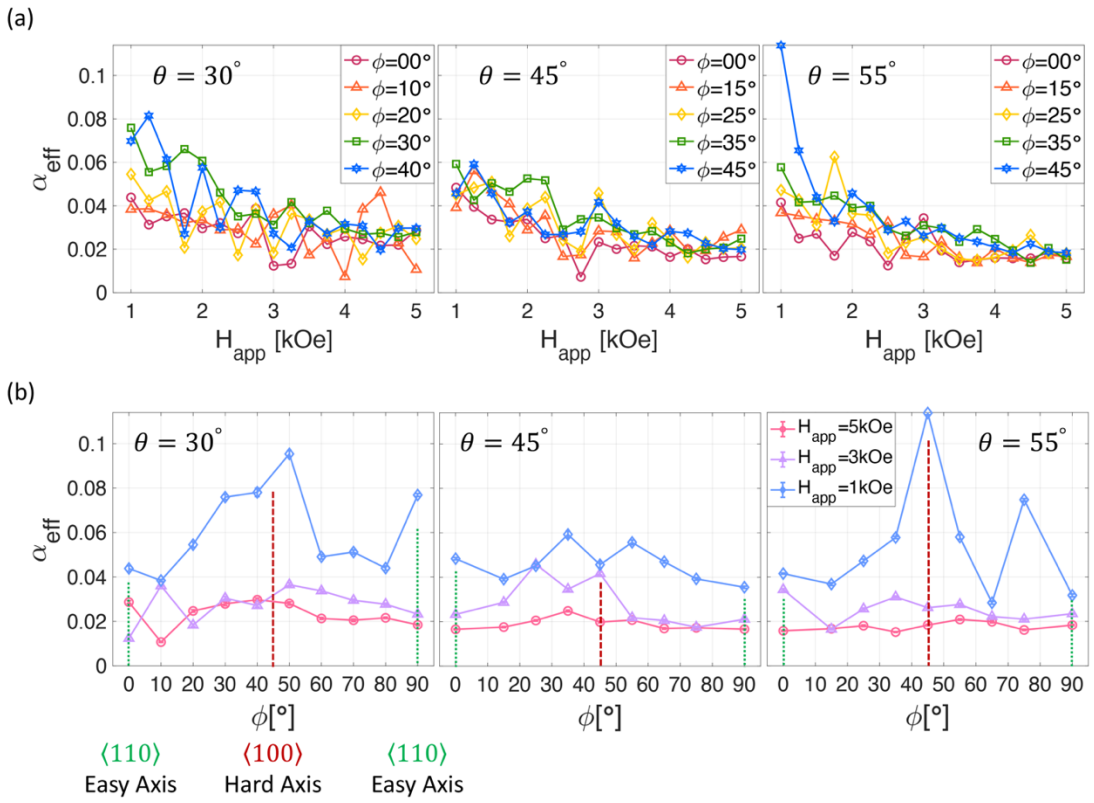

Figure 6.8. Effective magnetic damping parameter of CoFe/CMS magnetic bilayer film taken from the same data set as in figure 5. (a) The data were taken when the magnetic

field was applied from 1 kOe to 5 kOe, at three polar angles ($\theta_H = 30^{\circ}$, 45° and 55°, from left to right) and various azimuthal angles from $\phi_H = 0^{\circ}$ to 90°. Again, the green dotted (red dashed) lines are guides to the eye to denote when the in-plane component of the applied magnetic field is along the magnetic easy (hard) axis. (b) Effective damping parameter as a function of azimuthal angle at representive three applied fields for comparision, showing a strong orientational dependence at low fields and convergence to the intrinsic Gilbert damping at high fields due to the elimination of inhomegeneous broadening. [138]

Next, the field-dependent effective damping parameter was extracted by fitting the same data sets to equation (3.1), and the results are displayed for all the applied field intensity ranging from 1 kOe to 5 kOe. The field dependence of α_{eff} is plotted in Fig. 6.8(a) for various representative azimuthal angles and for all three polar angles. For all parameter sets, we observe the characteristic decrease of the effective damping as the applied field increases and inhomogeneous broadening mechanisms are eliminated[139]. Generally, the effective lifetime τ of the magnetization precession is given by

$$1/\tau = 1/\tau_{\text{Gilb}} + 1/\tau_{\text{ext}} \tag{6.3}$$

where τ_{Gilb} describes the intrinsic Gilbert damping and τ_{ext} represents extrinsic damping mechanisms that reduce τ (and thus increase α_{eff}) and typically depend on H_{app}. In our CMS film, two-magnon scattering (TMS), e.g. due to strain-induced

anisotropy inhomogeneities, is a dominant source of extrinsic damping[143]. Qualitatively identical curves to Fig. 7a have been analyzed with models that account for TMS[95,144] showing excellent agreement with the data (see Ref. [139]).

In addition, at low fields we see an apparent difference in α_{eff} as the azimuthal angle is varied while the high-field limit appears uniform for all orientations. To extract this field dependence more clearly, we show the dependence of α_{eff} on azimuthal orientation in Fig. 6.8(b) for low, intermediate, and high applied field for comparison. Indeed, at low fields we find a clear dependence of α_{eff} on ϕ_{H} with maximum damping at $\phi_{\mathrm{H}} = 45^{\circ}$, in agreement with the observations of Liu[137], where the inhomogeneous broadening explains the magnetocrystalline anisotropy. At high applied fields, however, this dependence disappears and the intrinsic Gilbert damping of ~ 0.02 is observed for all parameter combinations. We note that the relatively high α_{eff} may be due to the mechanical strains present in both the very thin CoFe and the CMS films. Such strain creates defects in the crystal when the strain is released, which cause additional spin wave scattering, leading to a larger effective damping parameter.

6.4. Conclusion

In summary, we investigated the magnetization dynamics of an epitaxial CMS thin film in a magnetic bilayer structure. Specifically, the dependence of the dynamic parameters on polar and azimuthal orientation of an applied magnetic field with respect to the MgO substrate was carefully analyzed. We found that the frequency of optically induced magnetization precessions in the CMS layer is fully determined by the

magnetocrystalline anisotropy of the CMS structure and not perturbed by the behavior of an adjacent thin CoFe film. In addition, field and angle dependent analysis of the precession damping revealed that variations reflecting the crystal symmetry and anisotropy are only observed at low applied fields (~1 kOe) while at high fields the effective damping converges to the intrinsic Gilbert damping for all experimental configurations.

These results reveal the magnetic dynamics of CMS layers embedded in a larger functional, magnetic bilayer structure, thus providing guidance for the design of future spintronic devices for which further reduction of the Gilbert damping is possible by optimizing the sample structure.

7. Hybrid Magnon-Phonon Dynamics in a Single-crystalline CoFe Nanomagnet

7.1. Introduction

In the previous chapter, we demonstrated improved Strong coupling in a single polycrystalline CoFe nanomagnet (p-CoFe NM) compared to a single Ni nanomagnet (Ni NM). However, the decay rate for the magnons in a p-CoFe NM was higher than the Ni NM due to stronger spin-orbit coupling (SOC) in CoFe materials system. Ironically, CoFe was chosen because they possess high magnetostriction coefficient originated from strong SOC. however, stronger SOC also contributes to higher magnetic damping. In order to achieve stronger magnon-phonon coupling, it is desired to use materials with high magnetostriction coefficient, and low magnetic damping parameter at the same time. Besides, potentially having lower phononic decay rate can be achieved when phonons can collectively vibrate in-phase in more ordered lattice structure. Therefore, in this chapter we investigate hybrid magnon-phonon dynamics in a single-crystalline CoFe NM.

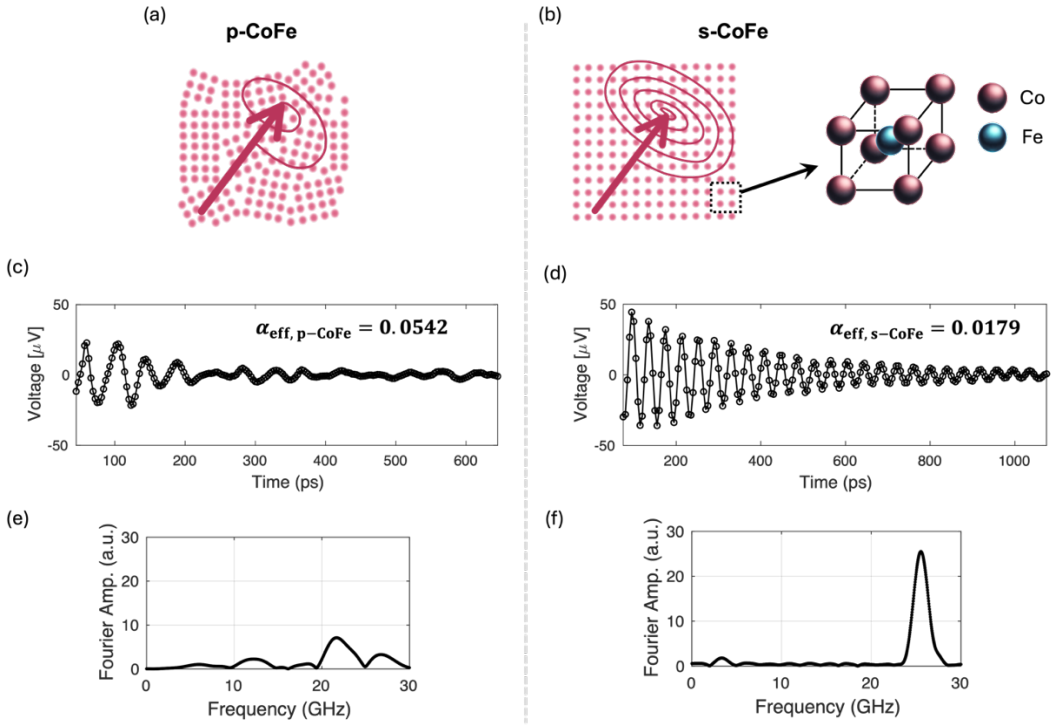

Figure 7.10. Comparison between the polycrystalline CoFe (p-CoFe) thin film and the single-crystalline CoFe (s-CoFe) thin film depicting the lower effective magnetic damping in s-CoFe thin film. (a, b) Illustration of magnetization precession out-of-phase in p-CoFe (a) and in-phase in s-CoFe (b). (c-f) TR-MOKE data collected in time domain for p-CoFe (c) and for s-CoFe (d), and their Fourier transformed data in frequency domain for p-CoFe (e) and s-CoFe (f). The data were taken at $H_{app} = 5\ kOe$, $\theta_H = 30°$, and $\phi_H \parallel < 110 >_{CoFe}$.

The p-CoFe film (thickness 20 nm) is composed of multiple crystalline grains where their crystalline orientation is randomly oriented, which results in the magnetization to precess out-of-phase (Fig. 7.1(a)). Contrary to this, the s-CoFe film is composed of

single crystalline grains that enables the magnetization to precess in-phase (Fig. 7.2(b)). Due to their distinct crystalline structure, the effective magnetic damping for p-CoFe ($\alpha_{\mathrm{eff,p-CoFe}} = 0.0542$) film was measured 3 times larger than the effective damping of s-CoFe ($\alpha_{\mathrm{eff,s-CoFe}} = 0.0179$). Therefore, in this chapter, we demonstrate engineering strategy to achieve both high magnetostriction coefficient and lower magnetic damping parameter in CoFe material system by introducing single-crystalline CoFe NM (s-CoFe NM).

7.2 Fabrication Methods

Patterning nanomagnets on the epitaxially grown CoFe films requires a different patterning process than the nanomagnet patterning process we used earlier in chapter 6 for p-CoFe NM and Ni NM studied previously. This is because the single-crystalline film must be grown epitaxially in a clean and atomically flat seed crystal layer, such as MgO [001] substrates. In this case, the single-crystalline CoFe film is grown one the substrates before beginning the nano-patterning process, requiring a top-down patterning approach. On top of this, there are multiple aspects to consider. Firstly, removal of a hard mask to free the phononic vibration is desired. Hydrogen Silsesquioxane (HSQ) has advantage of having high resolution in nanoscale patterning, however the removal of an HSQ hard mask after e-beam exposure involves strong chemicals. For this reason, an HSQ hard mask is often left on top of the nanoscale specimen since it is optically transparent. However, in this specific study, a HSQ hard mask would pin the vibration of nanomagnet when the bottom of the nanomagnet is

already pinned at the surface of the substrate. Thus, the pinning of phonons by leaving the hard mask is not desired. Secondly, nanoscale fabrication of magnetic materials has been intensively studied due to growing development on magnetic tunnel junctions (MTJs) on the industrial level. However, patterning of MTJs includes strong chemicals such as HF that can damage the magnetic properties of CoFe. In patterning MTJs, they fill up the gaps on the side of the MTJs with insulating layer such as SiO_2 or Al_2O_3 to prevent them from electrically shorting, which provides protection layer to magnetic properties of MTJs. Therefore, we introduce a HSQ mask patterning process with a metallic sacrificial layer to ensure that the hard mask is removed, partially freeing the vibration of phonons. The metallic sacrificial layer was carefully chosen to ensure that the magnetic properties of CoFe are not altered after wet etching of the metallic sacrificial layer. The patterning process was initially developed using polycrystalline Ni film, then using polycrystalline CoFe film, and finally the single-crystalline CoFe film was used to finalize the patterning process. These three steps are not necessary to find recipes for a single-crystalline nanomagnet. However, it is helpful to minimize the cost, and effort to grow and characterize multiple epitaxially-grown CoFe thin films.

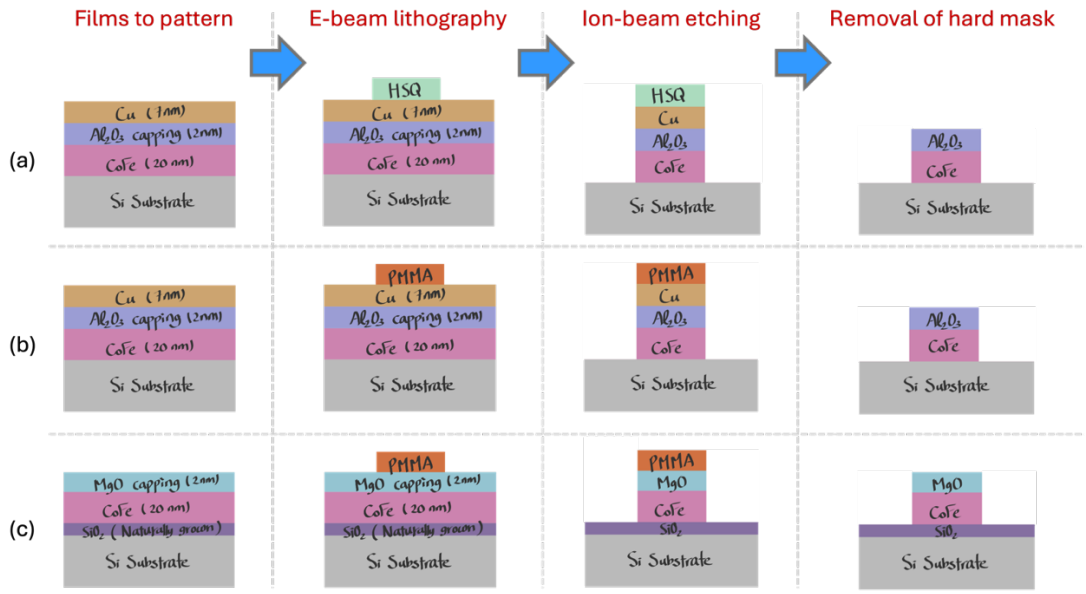

Figure 7.11. Three major patterning processes considered in this chapter for patterning a single-crystalline CoFe nanomagnet using Ar^+ IBE. (a) Metal sacrificial layer with HSQ mask.

We describe three major fabrication methods we attempted in this chapter, as illustrated in figure 7.2, all of which involve Ar^+ ion beam etching (IBE) at Stanford Nano Shared Facilities (SNSF) at Stanford University and removal of mask. First, a p-CoFe film (thickness 20 nm) was grown on a Si substrate, followed by deposition of oxide capping layer (Al_2O_3 was used when p-CoFe was grown via evaporation at the Molecular Foundry at University of California Berkely, and MgO was used when p-CoFe was grown via sputtering at the materials science and engineering initiative at University of California Santa Cruz). The first process is to use HSQ hard mask with Cu sacrificial layer as shown in figure 7.2(a). Advantages of this process are that HSQ e-beam resist

provides high resolution and negative-tone, suitable for patterning of multiple geometries of nanostructures. The second and third processes described in figure 7.2(b, c) are to use PMMA (PMMA 600K, Allresist, AR-P 669.07) as a mask with (Fig. 7.2b) or without (Fig. 7.2c) a Cu sacrificial layer. PMMA is relatively easy to remove (acetone or NMP) compared to HSQ. However, we noticed that PMMA adhered more strongly on the Al_2O_3 surface, making it harder to remove the PMMA soft mask. Typically, in our process, PMMA soft masks were removed by sonication in acetone for 30 min, and then IPA and DI water rinse, and this step was repeated one more time, followed by overnight soaking in acetone, and then rinsed in IPA and DI water, finally sonication in acetone for another 30 min and rinsed with IPA and DI water and N_2 blow dry was done. NMP can be also used to remove PMMA soft masks. To make sure that the PMMA masks are removed, a Cu sacrificial layer was also introduced in this case. A major disadvantage of using the PMMA mask to fabricate nanoscale structure is that the thickness of PMMA is in the range of hundreds of nanometers, whereas HSQ mask can be as thin as tens of nanometer thick. Consequently, such thick layer of PMMA mask becomes unstable and often falls before/during the IBE process, as the size of nanostructure of our interest lies between 150 ~ 300 nm, whereas the height of the PMMA masks were found in the range of 450 ~ 900 nm in this study.

7.2.1 Corner Shaping for Square Nanomagnets

Having sharp edges on the corners of square nanomagnets is desired in this study to confine the phononic energy. To achieve sharper corners for square nanomagnets, we

modified the shape of the square pattern as shown in figure 7.3(a). In figure 7.3, polycrystalline Ni nanomagnets were patterned PMMA mask without Cu layer. Without the corner shaping, the edge of the square nanomagnet resembles circular shape than square shape (7.3(b), corner 0nm). The size of the corner shaping was varied from 30 ~ 70 nm with respect to the 250 nm length of nanomagnet in the pattern design file. The SEM images of the resulting nanomagnets with $30, 50, 70$ nm of corner shaping are shown in the figure 7.3(b) with the length of the nanomagnet was measured $188, 200, 215$ nm. The nearly perfect square was achieved for the 70 nm in corner shaping for 200 nm-sized nanomagnets. Moving forward, the corner shaping of 50 ~ 70 nm was applied in the lithography design files.

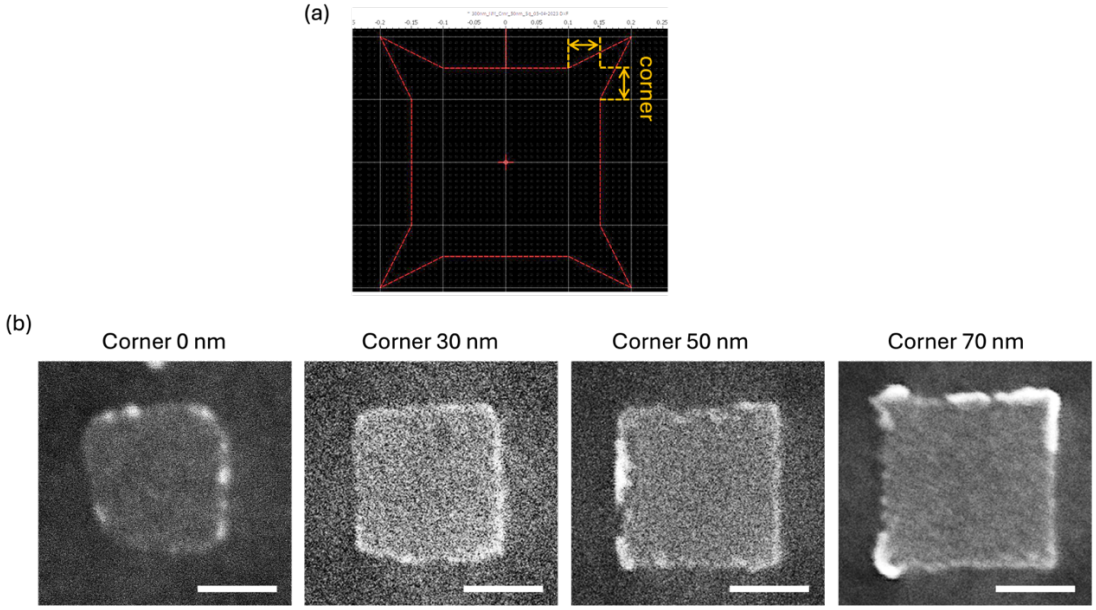

Figure 7.12. (a) Screen capture of an NPGS drawing file for a positive-tone EBL using PMMA with corner shaping. The size of the corner shape is marked with yellow arrows.

(b) SEM images of square nanomagnets with and without corner shapes. The scale bar is $100\ nm$.

7.2.2 Wet Etching Test

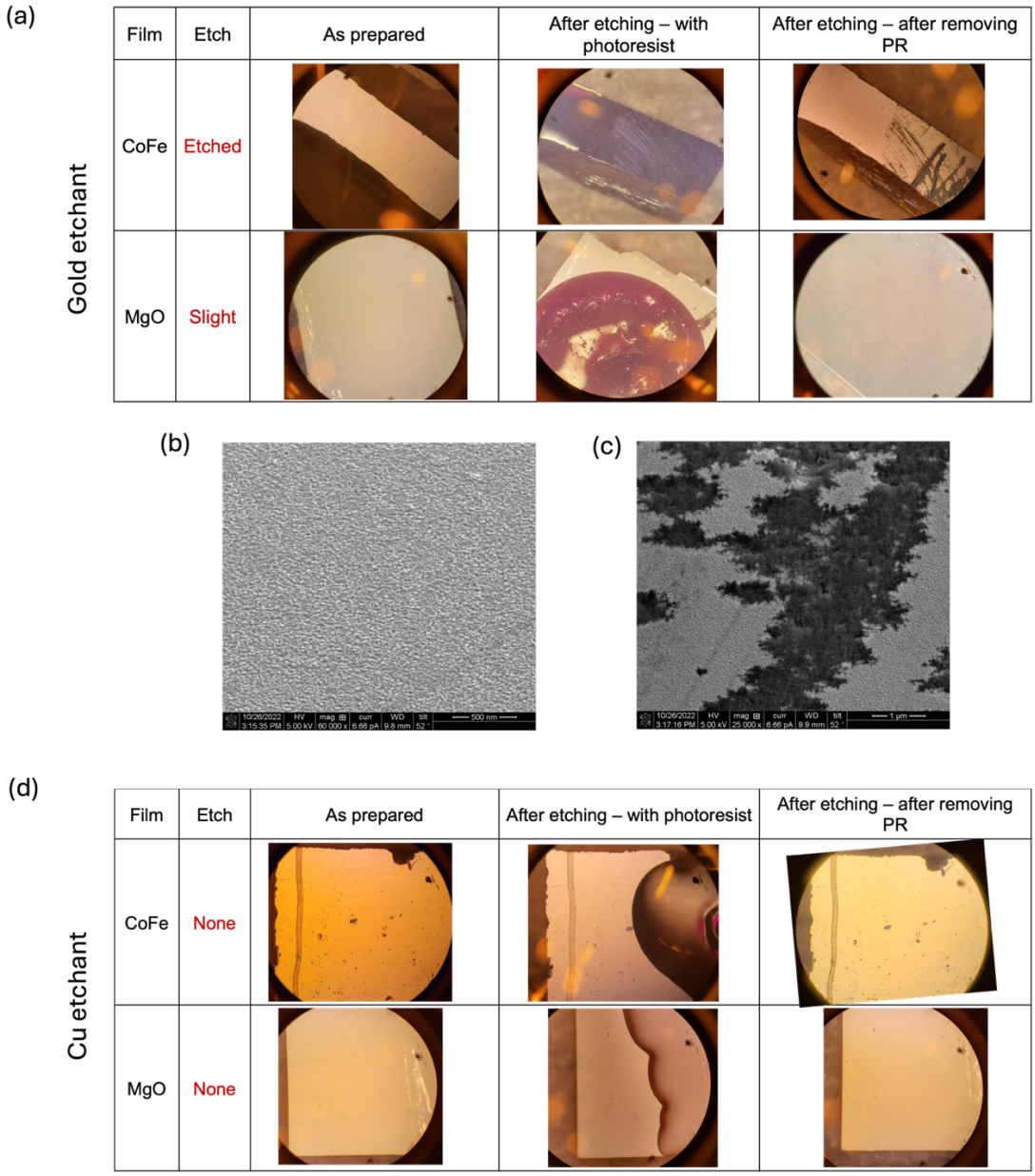

Figure 7.13. Wet etchant tolerance test on p-CoFe film and MgO film. (a, d) Optical microscope images showing before etching test (As prepared), after wet etching but before removal of photoresist, and after wet etching after removal of photoresist (PR) to compare the protected (covered by PR) and exposed area. (a) Tolerance test using

the gold etchant. The photoresist covers the left top of the p-CoFe sample and bottom of the MgO sample in the figure. The exposed area shows damages caused by etching from gold etchant. (b) SEM image of protected area covered by PR on p-CoFe sample. (c) SEM image of exposed area on p-CoFe sample. (d) Tolerance test using the copper etchant. The photoresist covers the right side of the p-CoFe and the MgO samples in the figure. The exposed area shows no damages caused by etching from copper etchant.

Cu was chosen as a sacrificial layer and citric acid-based Cu etchant (Copper etchant 49-1, Transene Company, Inc.) was used for wet etching of the Cu layer to remove the HSQ hard mask. As gold is one of the popular metals for the sacrificial layer, a tolerance test for the gold etchant was performed, and the result is shown in figure 7.4(a). After the etching test on CoFe for 5 sec and MgO for 10 sec, the gold etchant severely etched CoFe and slightly on MgO (Fig. 7.4a, c), compared to the area that was not exposed to the etchant protected by photoresist (Fig. 7.4b). The Transense Company Inc. informed us that if the gold etchant severely etches CoFe, the silver etchant will likely attack CoFe. For this reason, gold and silver were eliminated as metal sacrificial layer candidates. Additionally, the copper etchant tolerance test was performed in the same manner on CoFe and MgO for 15 sec, showing that Cu etchant did not etch both CoFe and MgO (Fig. 7.4d). This suggests that Cu is a great candidate for sacrificial layer for fabrication of single-crystalline nanomagnets grown on MgO substrates.

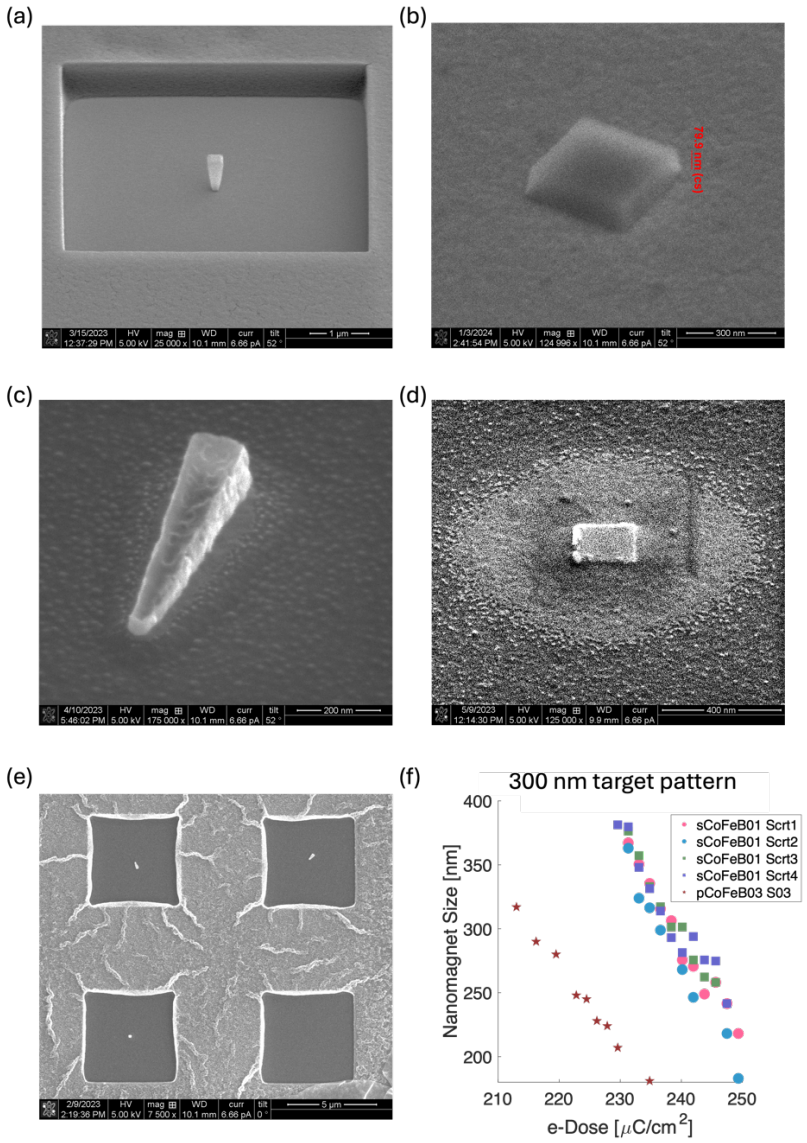

Figure 7.14. (a-e) SEM images of (a) PMMA soft mask on Ni test sample before IBE process, (b) HSQ hard mask on p-CoFe /Al_2O_3/Cu layer before IBE process, (c) PMMA soft mask on Ni test sample after ion-beam etched after fallen, (d) Ni test nanomagnet showing large area of redeposition (white circularly sputtered area around the square nanomagnet) of PMMA occurred during IBE process, and (e) PMMA protection layer (brighter area around the 4 etched squares) over the large area of the film after IBE

process with beam voltage at $800\,V$. (f) Dimensions of the nanomagnet versus electron-beam dose for EBL process.

7.2.3. Challenges and Improvements on Fabrication to Note

As mentioned earlier, the PMMA soft mask (Fig. 7.5a, 700 nm in height shown in the figure) tends to be thicker than the HSQ hard mask (Fig. 7.5b, 80 nm in height shown in the figure), resulting in more complicated fabrication process. For example, the soft mask tends to fall before or during the IBE process due to small nanomagnet size compared to the height of the soft mask (Fig. 7.5c). Another critical problem during the IBE process is the redeposition of PMMA onto the side of the nanomagnet, as shown in figure 7.5(d). The redeposited PMMA near the nanomagnet pattern hinders Ar^+ ion beam from etching the nanomagnet, creating broadening of the sidewall of nanomagnet. A sidewall is not desired in this coupled magnon-phonon study because of the broadening of phononic frequencies. In this case, introducing a two-step IBE process with etching at higher angle (angle near surface) followed by etching at lower angle (angle near surface normal) to remove the sidewall redeposition is possible. Another way is to significantly lower the height of the PMMA mask is to thin the PMMA by mixing with thinning agents such as chlorobenzene, anisole or ethyl lactate.

As mentioned earlier and shown in figure 7.5(c, d), a PMMA mask can be often hard to remove after the entire patterning process. We have seen the PMMA mask left on top of the nanomagnets (Fig. 7.5c) or partially removed leaving PMMA residue on top of the nanomagnets (white residues at the edge of nanomagnet in figure. 7.5d). To

ensure that the PMMA masks are thoroughly removed, a metal sacrificial layer can be introduced as illustrated in figure 7.2(c). There are multiple parameters to tune in IBE process. One is the beam voltage that is a tuning knob for the energy of Ar ion beams. The higher the voltage, the faster ions provide straight etching of the nanoelement, making smaller sidewalls. At the same time, the ions at higher voltage can cause the PMMA to be cured at higher temperature, as shown in figure 7.5(e), making the PMMA layer harder to remove. Despite using the identical design file for patterning the nanomagnets, the final size of the nanomagnets depends heavily on the electron beam dose upon EBL. In figure 7.5(f), the final size of the nanomagnets inversely proportional to electron beam dose at EBL. In this process, the nanomagnet size in the design file was at 300 nm in diameter for circle nanomagnets and in length for square nanomagnets. However, the final dimensions of the nanomagnets are found in the range of 180 ~ 400 nm. Please note that most of the initial challenges were investigated with Ni test samples and the optimized patterning process was applied to p-CoFe NM patterning process and developed for p-CoFe and s-CoFe NM.

7.2.4. Fabrication Process for s-CoFe NM

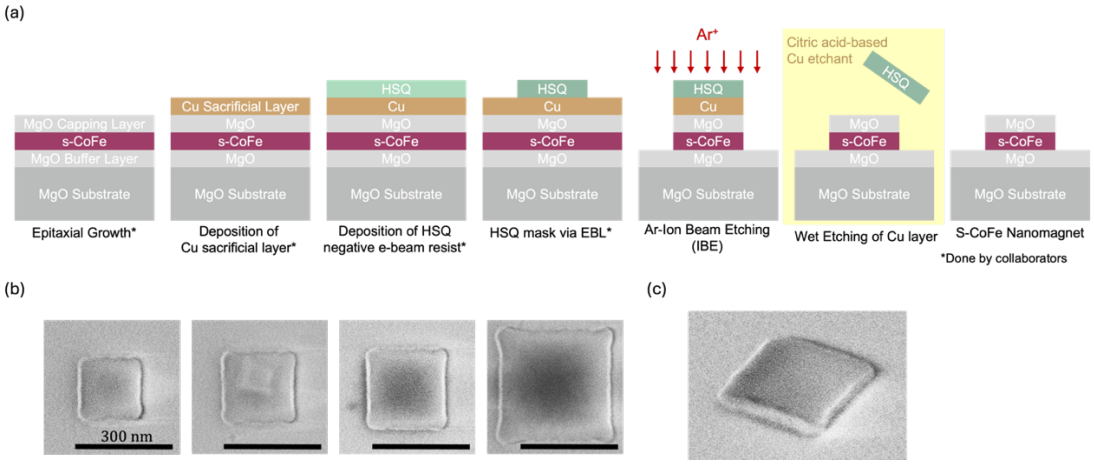

Figure 7.15. (a) Sequence of patterning process steps. (b) SEM images of the single-crystalline CoFe nanomagnets fabricated using the process described in (a). The size of square NM was fabricated between 185 ~ 337 nm in length. (c) The tilted SEM image of the right-most NM in (b). The scale bar is 300 nm.

The final patterning process developed for making s-CoFe NM is shown in figure 7.6(a). To begin with, the $Co_{50}Fe_{50}$ (CoFe) was sputtered on MgO[001] substrate at room temperature in the Lederman lab at University of California Santa Cruz. The MgO substrate was initially annealed and a thin layer of MgO was deposited using pulsed laser deposition (PLD). The substrate was then transferred to an RF-sputtering chamber without breaking vacuum, and CoFe was deposited at room temperature followed by annealing (500 ℃ for 30 min) and cooling (400 ℃ for 1 hour) steps. Finally, the sample was transferred back to the PLD chamber to deposit a thin MgO capping layer (1.4 nm). The crystalline orientation and the thickness of the film were characterized,

and they are shown in figure 6.3. The film was shipped to the Molecular Foundry at the Lawrence Berkeley National Lab for e-beam evaporation of a copper layer (thickness 30 nm), and HSQ was deposited for e-beam lithography (EBL). The HSQ was then developed to make a hard mask for the IBE process. at Stanford University. IBE was performed at a beam voltage at 400 V, beam current at 30 mA, stage angle 95° (5° off from surface normal direction), for 5 min 30 sec at 11 sccm Ar environment. The rest of the parameters was followed by the standard manual for recipe 2 provided at SNSF (as of May 2024). The etch rate of CoFe, MgO, and Cu layers was investigated by performing atomic force microscope (AFM) in the Lederman lab. The HSQ hard mask was removed by Cu wet etching using a heated magnetic stirrer at 25° at 300 rpm for 15 min for consistency. The chip was immediately soaked in DI water bath followed by rinsing it with DI water using a syringe to prevent HSQ hard mask residues from adhering back to the s-CoFe NM. The sample was rinsed in DI water again and then N_2 blow dried.

7.2.5. Validation of Compatibility of Fabrication Process for s-CoFe NM

After developing a nanopatterning process to fabricate s-CoFe NM, optical characterization was used to validate the compatibility of the fabrication process on the magnetic properties of s-CoFe. In this validation, TR-MOKE was used to extract the magnetic properties of the s-CoFe film at three different stages; freshly after growth of the s-CoFe film (June 2022), before patterning on the s-CoFe film (April 2024), and

after patterning of the s-CoFe NM (a 5 μm × 5 μm large area was also patterned on the same sample with the rest of s-CoFe NM) (June 2024). The Fourier transformed TR-MOKE data was then fitted to the Kittel mode calculated for a s-CoFe thin film introduced in chapter 6 (Fig. 7.7a-c). The magnetic parameters of γ, M_S, K_1, and K_{Uni} were extracted from the Kittel fitting and compared in the table 7.1, suggesting the magnetic properties are well conserved after the entire patterning process. This confirms that the patterning process introduced in this chapter is CoFe compatible, and can potentially be used as a standard nanomagnet patterning process using epitaxially-grown magnetic thin films grown on MgO substrates.

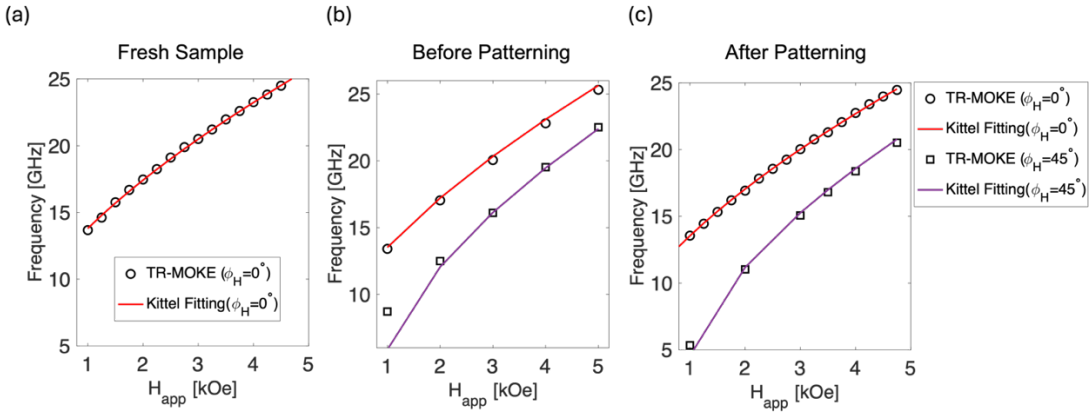

Figure 7.16. Fourier transformed TR-MOKE data in the frequency domain for the identical s-CoFe thin film measured (a) fresh after growth, (b) before patterning, and (c) after patterning process. The scatter plots show TR-MOKE data, and the solid lines are the Kittel mode. The data were taken at $1\ kOe \leq H_{app} \leq 5\ kOe$, $\theta_H = 30°$, and $\phi_H = 0°$ or $\phi_H = 45°$.

Timeline	γ [rad/Oe · s]	M_S[emu /cm^3]	K_1[emu /cm^3]	K_{Uni}[emu /cm^3]
Freshly after growth	1.83×10^7	1997	-3.84×10^5	0.63×10^5
Before patterning	1.81×10^7	2057	-3.51×10^5	0.66×10^5
After patterning	1.80×10^7	1961	-3.91×10^5	0.69×10^5

Table 7.4. Summary of magnetic parameters of γ, M_S, K_1, and K_{Uni} measured and fitted for three different times.

7.3. Coupled Dynamics in a Single Nanomagnet

The coupled magnon-phonon dynamics were studied using the same methods as described in chapter 5, on a single s-CoFe NM (214 nm × 214 nm × 10.8 nm), and was compared to the uncoupled magnon system on a s-CoFe thin film that was also patterned as a larger area (5 µm × 5 µm) for this purpose on the same sample that s-CoFe NMs were patterned.

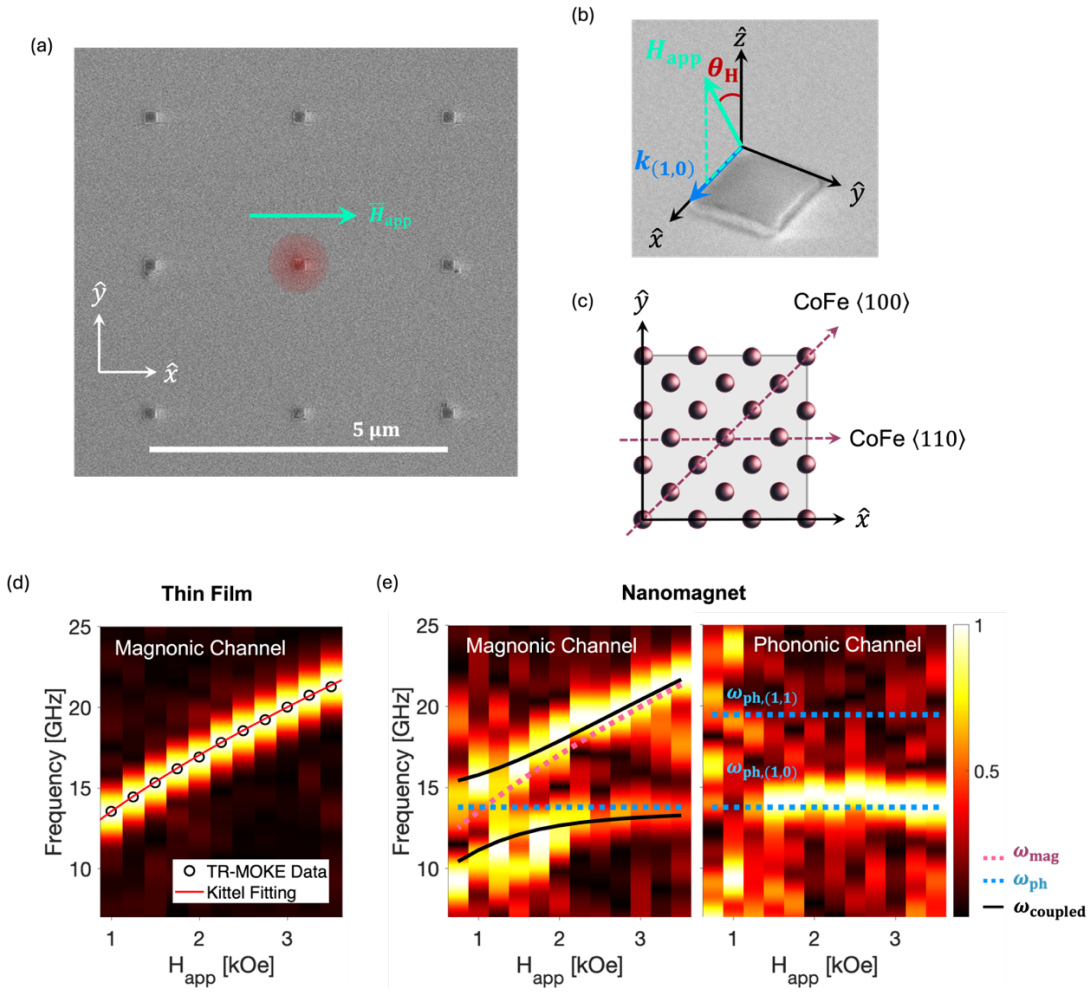

Figure 7.17. (a) SEM image of multiple isolated s-CoFe NMs. Red circled area represents the probe beam. The H_{app} is applied along the $\hat{x}$-axis parallel to the edge of the nanomagnet. (b) SEM image of an arbitrary nanomagnet and H_{app} and $k_{(1,0)}$ with respect to the geometry of the nanomagnet. (c) Crystalline orientation of s-CoFe (represented by pink spheres) with respect to the shape of the nanomagnet (outlining grey square) (d, e) Fourier transformed TR-MOKE data in frequency domain. (d) Magnonic dynamics of s-CoFe thin film and (e) Magnonic (left) and Phononic (right) dynamics of s-CoFe NM.

The magnetic field was applied between $0.75\ \text{kOe} \leq H_{\text{app}} \leq 3.5\ \text{kOe}$, $\theta_{\text{H}} = 30°$, and $\phi_{\text{H}} = 0°$ ($\phi_{\text{H}} \parallel \langle 110 \rangle_{\text{CoFe}}$) (Fig. 7.8a-c), and their optical responses in frequency domain are demonstrated in figure 7.8 (d,e). In the uncoupled magnon response, a single frequency at each applied magnetic field was observed (Fig. 7.8d, scatter plot), and it was fitted to the Kittel mode calculated using equation (2.62) by inputting the total energy described in equation (6.1) (Fig. 7.8d, black solid line). The TR-MOKE data and the Kittel mode shown for the thin film is the same data taken for validating the fabrication process in the earlier section for after patterning case (Fig. 7.7c).

The frequency response of the coupled magnonic and phononic dynamics was experimentally measured and plotted in figure 7.8 (e). The magnonic mode without considering coupling using the Kittel fitting from the thin film is plotted as a pink dotted line, assuming $\rho = 8190\ \text{kg/m}^3$ and $\nu = 0.29$, the fitting returned $\gamma = 1.80 \times 10^7 \text{rad/Oe} \cdot \text{s}$, and $M_{\text{S}} = 1961\ \text{emu/cm}^3$. Likewise, the phononic mode without considering coupling is plotted as the blue dotted line, which is fitted to equation (4.31). Similar to the coupled magnon-phonon dynamics observed in p-CoFe NM, the hallmark of strong coupling was observed which was characterized by splitting of frequency upon intersection of magnonic and phononic frequencies. The anticrossing behavior of the coupled dynamics was fitted to equation (4.35), where the total energy (G_{total}) was altered to reflect the free energy of the single-crystalline film and plotted in figure 7.8(e) in black solid lines. Additionally, anisotropy was accounted for in this

fitting by putting $b_1 \neq b_2$, and $\phi_{\mathrm{MP}} = 0°$ for (1,0) phonon crossing. The corresponding fitting provided parameters of $E = 256\ \mathrm{GPa}$, $b_1 = -2.49 \times 10^{-4}$ Oe and $b_2 = -26.56 \times 10^{-4}$ Oe.

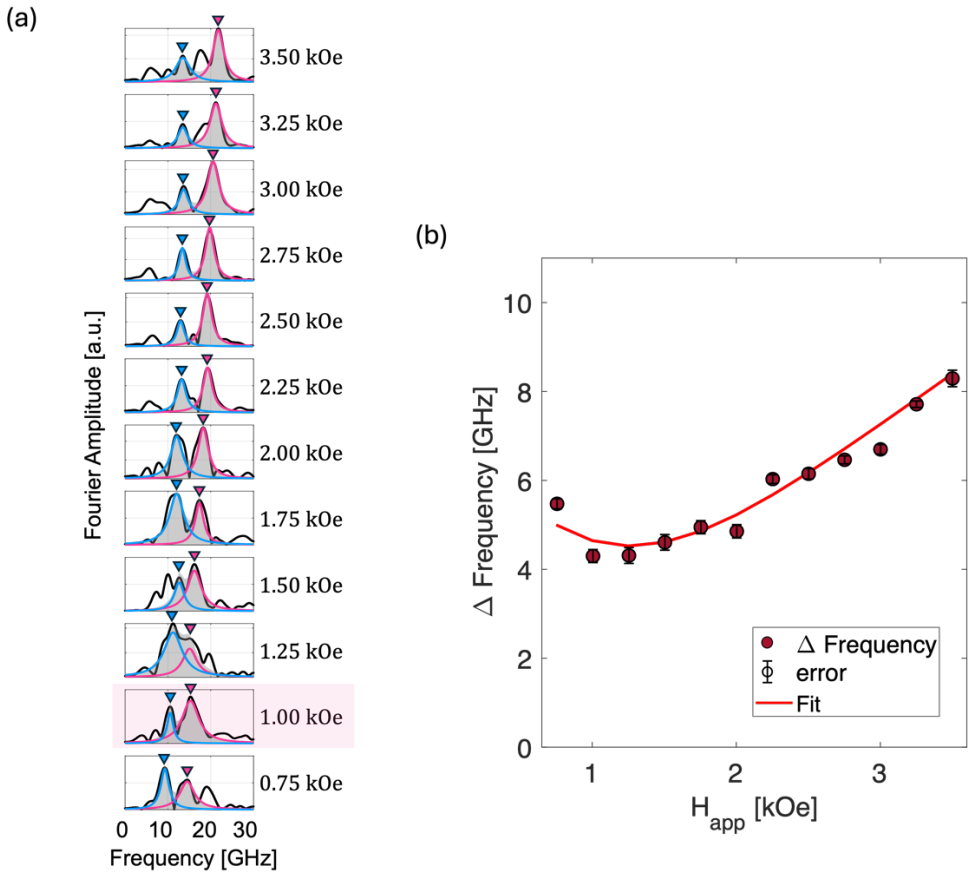

Figure 7.18. (a) Fourier transformed TR-MOKE data in frequency domain with $0.75\ kOe \leq H_{app} \leq 3.5\ kOe$. The Lorentzian distribution of two main frequencies responsible for magnon-phonon coupling are plotted with blue and pink lines. (b) The Δf of two corresponding peaks vs. H_{app}. The TR-MOKE data are plotted with scatter plot and the fitting is plotted with red solid line. Error bars represent the uncertainties calculated using covariance function.

The two frequencies at anticrossing for (1,0) phonon mode were fitted using Lorentzian distribution, as shown in figure 7.9(a) in blue and pink lines with their peak frequency locations indicated with blue and pink arrows. The difference in the two frequencies (line splitting) is plotted in figure 7.9(b) showing very good agreement with the fit. Furthermore, the $\Delta f_{\min} = 4.31$ GHz was observed at $H_{\text{app}} = 1.00$ kOe (Fig. 7.9(a), highlighted) which is 3.06 times larger than the splitting found in a single Ni NM ($\Delta f_{\min,\text{Ni}} = 1.41$ GHz, (2,0) crossing at $\phi_{\text{H}} = 45°$)[98], and 1.20 times larger than in a single p-CoFe NM ($\Delta f_{\min,\text{p-CoFe}} = 3.60$ GHz, (1,1) crossing at $\phi_{\text{H}} = 0°$).

Material	Crossing	Γ_{C} (GHz)	κ_{M} (GHz)	κ_{P} (GHz)	C
Ni	(2,0), 45°	0.71	0.65	0.47	1.65
p-CoFe	(1,1), 0°	1.80	1.23	0.29	8.93
s-CoFe	(1,0), 0°	2.15	0.41	0.29	37.94

Table 7.5. Summary of coupling strength, loss rate, cooperativity between Ni NM, p-CoFe NM, and s-CoFe NM.

Material	Γ_{C} (GHz)	N ($\times 10^7$)	C	Γ_0(Hz)	C/V(μm^{-3})
YIG*	0.136	1.2×10^{10}	13,000	0.38	0.001589
Ni	0.71	6.35	1.65	8.85×10^4	505.05
p-CoFe	1.80	22.61	8.93	11.97×10^4	6,880.24

s-CoFe	2.15	10.22	37.94	21.29×10^4	76,708.95

Table 7.6. Summary of coupling strength, volume, number of spins, cooperativity, coupling strength for a single Bohr magneton, and cooperativity per unit volume between YIG sphere, Ni NM, p-CoFe NM, and s-CoFe NM. * Note that the parameters for YIG sphere were taken from magnon-photon coupling.

In order to quantify the strength of the magnon-phonon coupling, the cooperativity was calculated following the same analysis done for p-CoFe NM. For (1,0) crossing, $\alpha_{\mathrm{eff,M}} = 0.0306$ at $f_{\mathrm{M}} = 13.55$ GHz, giving the intrinsic loss rate for magnon $\kappa_{\mathrm{M}} = 0.41$ GHz, and $\alpha_{\mathrm{eff,P}} = 0.0206$ at $f_{\mathrm{P}} = 14.29$ GHz, giving the intrinsic loss rate for phonon $\kappa_{\mathrm{P}} = 0.29$ GHz. With $\Gamma_{\mathrm{C}} = 2.15$ GHz, the cooperativity was calculated $C = 37.94$ (Table 7.2), demonstrating a Strong coupling in a single s-CoFe NM system. It is more than 4 times larger cooperativity despite the 2.62 times smaller volume compared to the p-CoFe NM presented in chapter 5, and 23 times larger cooperativity despite the 6.6 times smaller volume in the s-CoFe NM in this study compared to the previously reported Ni NM. Such a large cooperativity was achieved by introducing a single-crystalline nanomagnet that contributed lower magnon loss rate ($\kappa_{\mathrm{M,s-CoFe}} = 0.0306$) compared to p-CoFe NM ($\kappa_{\mathrm{M,p-CoFe}} = 1.23$). It is worth noting that $\kappa_{\mathrm{P,s-CoFe}}$ did not improve compared to $\kappa_{\mathrm{P,p-CoFe}}$, due to the pinning of the s-CoFe NM on the surface of substrate, similar to the p-CoFe NM.

In order to account for the smaller volume in s-CoFe NM, the coupling strength per Bohr magneton (Γ_0) and the cooperativity per unit volume (C/V in μm^{-3}) is compared in table 7.3. The Γ_0 is increased by 1.78, compared to a p-CoFe NM and 2.40 compared to a Ni NM. Moreover, C/V was achieved 11.15 times larger than found in a p-CoFe NM, and 151.88 times larger than found in Ni NM. To provide more insight on how strong the coupling is compared to other hybrid quantum systems, again, we compared the Γ_0 and C/V of the magnon-phonon system in a s-CoFe NM to the magnon-photon coupled system in a YIG sphere. The Γ_0 was found $574{,}010$ times larger and C/V was found $48{,}275{,}000$ times larger than in a YIG sphere of magnon-photon system.

This study demonstrates the importance of choice of materials and their crystallinity in realizing strong magnon-phonon coupled system. The proposed s-CoFe NM as a strongly coupled magnon-phonon hybrid system potentially further increased by introducing free-standing structure to realize unpinning of phononic vibration from substrate[145]. On this note, the single-crystalline CoFe nanomagnets can be a great candidate material for rare-earth-free hybrid magnon-phonon quantum applications.

Chapter 8. Outlook and Future Work

The interplay of magnons and phonons has long been studied since the first theoretical and experimental investigation of magnetoelastically coupled systems in the late 1950s. However, strong coupling of magnon-phonon system has been experimentally demonstrated only recently in 2019[98]. Thanks to the development of cutting-edge fabrication and patterning technologies in nanoscale magnetic materials, a much wider range of choice of materials and geometries has become available, contributing to recent progress in the study and understanding of magnetoelastically coupled dynamics. We saw that there are several building blocks to efficiently create and engineer a magnetoelastically coupled system, such as excitation methods, geometry of phonons and magnetic elements, composition of magnetostrictive materials, and fabrication methods. The calculation presented in chapter 4 readily suggests that highly magnetostrictive materials with low magnonic damping parameter can be used to achieve higher cooperativity. Indeed, large mode splitting was observed in a material system with higher magnetostriction, and a larger cooperativity was found when an epitaxial magnetostrictive material was introduced. Note that the magnetostriction can be further improved when samples are treated post-fabrication annealing process. Furthermore, the geometry of the magnon-phonon system and excitation methods significantly influence the coupled dynamics. For example, the phononic modes were

quantized in a nanoelement, whereas continuous phononic modes were found in a thin film counterpart.

Creative magnetic nanostructure designs offer an additional avenue for tailoring coupling strength. In a recent report, a free-standing monocrystalline YIG nanobridge was fabricated utilizing cutting-edge patterning methods.[33] In this 3D free-standing nanostructure, near-ideal low magnetic damping of $\alpha = 2.6 \times 10^{-4}$ for epitaxial YIG in a nanostructure was achieved.

One of the biggest challenges in investigating coupled magnon-phonon systems is ironically of fundamental nature. Recall that exploring a material system that has both high magnetostriction coefficient and low magnetic damping parameter is critical in increasing the coupling strength. However, as the magnetostriction originates from the spin-orbit coupling, it is difficult to find such materials system as damping is generally higher in materials with stronger spin-orbit coupling. Indeed, we demonstrated by introducing epitaxially-grown magnetic film, that the coupling is further improved due to lower magnetic damping parameter in an ordered crystalline structure despite the high spin-orbit coupling in a high magnetostrictive material system.

Investigating diverse mechanisms to activate magnetoelastic coupling is also of significant importance. Magneto-rotation coupling for example, is an emerging research field[37,146,147]. Recently, theoretical work on spin-rotation coupling showed that spin current can be generated in nonmagnets. This is a process that does not rely on spin current or spin-orbit interaction in the presence of SAWs[147]. The spin current can be further increased when a material with longer spin lifetime is chosen, suggesting

that utilizing Cu material can generate a much larger spin current than what can be achieved in a Pt system. Besides this theoretical work, an experimental effort to demonstrate magneto-rotation coupling was conducted in a $Co_{20}Fe_{60}B_{20}$ system that possesses perpendicular magnetic anisotropy[37]. In this study, nonreciprocal attenuation of SAWs up to 100 % rectification was showcased. Other research groups reported the use of surface roughness to manipulate the Damon-Eshbach (DE) magnons[148].

Magnetoelastic coupling holds relevance across a wide range of research domains, including the previously mentioned fields of straintronics, magnonics, and quantum technology. Recently, researchers found opportunities of applying magnetoelastic coupling in wearable devices[149] and biosensing technologies.[150–154] The magnetoelastic property in a soft fiber magnetic material can be enhanced by mixing nanomagnet particles inside the 1D soft magnet.[149] This is a crucial development in wearable electronics as biomechanical energy is converted to electrical energy, opening a pathway to various coupled system in wearable technologies. One of the examples in biosensing technology, attachment of virus particles on an antibody placed on a magnetostrictive substrate changes the magnetic resonance frequency due to the deformation induced by the increased weight on the antibody.[154]

Since the first observation of intrinsic ferromagnetic properties found in 2D van der Waals materials in 2017, there is growing interest in exploring the magnetic properties in 2D materials.[155–157] More interestingly, magnon-phonon coupling was observed in a few different 2D material systems, opening new pathway to new fundamental studies and potentially novel technologies.[158–160]

The emerging field of hybrid magnon-phonon systems in a nanostructure presents great opportunities as the experimental understanding is only in its infancy. The possibility to tailor the dynamic magnetic properties by optimizing and mixing and matching the different building blocks opens exciting avenues to explore new physics and create novel devices.

Bibliography

1. Kittel, C. Interaction of Spin Waves and Ultrasonic Waves in Ferromagnetic Crystals. *Phys. Rev.* **110**, 836–841 (1958).
2. Auld, B. A. Walker Modes in Large Ferrite Samples. *J. Appl. Phys.* **31**, 1642–1647 (1960).
3. Bömmel, H. & Dransfeld, K. Excitation of Hypersonic Waves by Ferromagnetic Resonance. *Phys. Rev. Lett.* **3**, 83–84 (1959).
4. Schlömann, E. Generation of Phonons in High-Power Ferromagnetic Resonance Experiments. *J. Appl. Phys.* **31**, 1647–1656 (1960).
5. Eshbach, J. R. Spin-Wave Propagation and the Magnetoelastic Interaction in Yttrium Iron Garnet. *J. Appl. Phys.* **34**, 1298–1304 (1963).
6. Schlömann, E. & Joseph, R. I. Generation of Spin Waves in Nonuniform Magnetic Fields. III. Magnetoelastic Interaction. *J. Appl. Phys.* **35**, 2382–2390 (1964).
7. Damon, R. W. & Van De Vaart, H. Dispersion of spin waves and magnetoelastic waves in YIG. *Proc. IEEE* **53**, 348–354 (1965).
8. Auld, B. A., Collins, J. H. & Zapp, H. R. ADIABATIC TIME DOMAIN CONVERSION OF HYBRID, MAGNETOELASTIC WAVES IN YIG. *Appl. Phys. Lett.* **10**, 186–188 (1967).
9. Comstock, R. L. & Kusnezov, N. Magnetoelastic-Elastic Wave Scattering. *J. Appl. Phys.* **38**, 3740–3744 (1967).
10. Rezende, S. M. & Morgenthaler, F. R. Magnetoelastic Waves in Time-Varying Magnetic Fields. I. Theory. *J. Appl. Phys.* **40**, 524–536 (1969).

11. D'Souza, N., Salehi Fashami, M., Bandyopadhyay, S. & Atulasimha, J. Experimental Clocking of Nanomagnets with Strain for Ultralow Power Boolean Logic. *Nano Lett.* **16**, 1069–1075 (2016).

12. Salehi Fashami, M., Roy, K., Atulasimha, J. & Bandyopadhyay, S. Magnetization dynamics, Bennett clocking and associated energy dissipation in multiferroic logic. *Nanotechnology* **22**, 309501 (2011).

13. Salehi Fashami, M., Atulasimha, J. & Bandyopadhyay, S. Magnetization dynamics, throughput and energy dissipation in a universal multiferroic nanomagnetic logic gate with fan-in and fan-out. *Nanotechnology* **23**, 105201 (2012).

14. Liang, C.-Y. *et al.* Electrical control of a single magnetoelastic domain structure on a clamped piezoelectric thin film—analysis. *J. Appl. Phys.* **116**, 123909 (2014).

15. Ahmad, H., Atulasimha, J. & Bandyopadhyay, S. Reversible strain-induced magnetization switching in FeGa nanomagnets: Pathway to a rewritable, non-volatile, non-toggle, extremely low energy straintronic memory. *Sci. Rep.* **5**, 18264 (2015).

16. Liang, C.-Y., Sepulveda, A., Keller, S. & Carman, G. P. Deterministic switching of a magnetoelastic single-domain nano-ellipse using bending. *J. Appl. Phys.* **119**, 113903 (2016).

17. Mondal, S. *et al.* Hybrid Magnetodynamical Modes in a Single Magnetostrictive Nanomagnet on a Piezoelectric Substrate Arising from Magnetoelastic Modulation of Precessional Dynamics. *ACS Appl. Mater. Interfaces* **10**, 43970–43977 (2018).

18. Winters, D., Abeed, M. A., Sahoo, S., Barman, A. & Bandyopadhyay, S. Reliability of Magnetoelastic Switching of Nonideal Nanomagnets with Defects: A Case Study for the Viability of Straintronic Logic and Memory. *Phys. Rev. Appl.* **12**, 034010 (2019).

19. Ulrichs, H., Meyer, D., Döring, F., Eberl, C. & Krebs, H.-U. Spectral control of elastic dynamics in metallic nano-cavities. *Sci. Rep.* **7**, 10600 (2017).

20. Lapine, M., Shadrivov, I. V., Powell, D. A. & Kivshar, Y. S. Magnetoelastic metamaterials. *Nat. Mater.* **11**, 30–33 (2012).

21. Liang, C.-Y., Sepulveda, A. E., Hoff, D., Keller, S. M. & Carman, Gregory. P. Strain-mediated deterministic control of 360° domain wall motion in magnetoelastic nanorings. *J. Appl. Phys.* **118**, 174101 (2015).

22. Xiao, Z. *et al.* Bi-directional coupling in strain-mediated multiferroic heterostructures with magnetic domains and domain wall motion. *Sci. Rep.* **8**, 5207 (2018).

23. Chen, C., Barra, A., Mal, A., Carman, G. & Sepulveda, A. Voltage induced mechanical/spin wave propagation over long distances. *Appl. Phys. Lett.* **110**, 072401 (2017).

24. Duflou, R. *et al.* Micromagnetic simulations of magnetoelastic spin wave excitation in scaled magnetic waveguides. *Appl. Phys. Lett.* **111**, 192411 (2017).

25. Tierno, D. *et al.* Strain coupling optimization in magnetoelectric transducers. *Microelectron. Eng.* **187–188**, 144–147 (2018).

26. Mahmoud, A. *et al.* Introduction to spin wave computing. *J. Appl. Phys.* **128**, 161101 (2020).

27. Vanderveken, F. *et al.* Excitation and propagation of spin waves in non-uniformly magnetized waveguides. *J. Phys. Appl. Phys.* **53**, 495006 (2020).

28. Chumak, A. V. *et al.* Advances in Magnetics Roadmap on Spin-Wave Computing. *IEEE Trans. Magn.* **58**, 1–72 (2022).

29. Li, Y., Zhao, C., Zhang, W., Hoffmann, A. & Novosad, V. Advances in coherent coupling between magnons and acoustic phonons. *APL Mater.* **9**, 060902 (2021).

30. Weiler, M. *et al.* Elastically Driven Ferromagnetic Resonance in Nickel Thin Films. *Phys. Rev. Lett.* **106**, 117601 (2011).

31. Dreher, L. *et al.* Surface acoustic wave driven ferromagnetic resonance in nickel thin films: Theory and experiment. *Phys. Rev. B* **86**, 134415 (2012).

32. Berk, C., Jaris, M., Yang, W., Dhuey, S. & Cabrini, S. Strongly Coupled Magnon-Phonon Dynamics in a Single Nanomagnet Supplementary.

33. Heyroth, F. *et al.* Monocrystalline Freestanding Three-Dimensional Yttrium-Iron-Garnet Magnon Nanoresonators. *Phys. Rev. Appl.* **12**, 054031 (2019).

34. Alekseev, S. G. *et al.* Magnons parametric pumping in bulk acoustic waves resonator. *Appl. Phys. Lett.* **117**, 072408 (2020).

35. An, K. *et al.* Coherent long-range transfer of angular momentum between magnon Kittel modes by phonons. *Phys. Rev. B* **101**, 060407 (2020).

36. Godejohann, F. *et al.* Magnon polaron formed by selectively coupled coherent magnon and phonon modes of a surface patterned ferromagnet. *Phys. Rev. B* **102**, 144438 (2020).

37. Xu, M. *et al.* Nonreciprocal surface acoustic wave propagation via magneto-rotation coupling. *Sci. Adv.* **6**, eabb1724 (2020).

38. Zhang, X., Bauer, G. E. W. & Yu, T. Unidirectional Pumping of Phonons by Magnetization Dynamics. *Phys. Rev. Lett.* **125**, 077203 (2020).

39. Zhang, J. *et al.* Long decay length of magnon-polarons in BiFeO3/La0.67Sr0.33MnO3 heterostructures. *Nat. Commun.* **12**, 7258 (2021).

40. Hatanaka, D. *et al.* On-Chip Coherent Transduction between Magnons and Acoustic Phonons in Cavity Magnomechanics. *Phys. Rev. Appl.* **17**, 034024 (2022).

41. Hioki, T., Hashimoto, Y. & Saitoh, E. Coherent oscillation between phonons and magnons. *Commun. Phys.* **5**, 115 (2022).

42. Schlitz, R. *et al.* Magnetization dynamics affected by phonon pumping. *Phys. Rev. B* **106**, 014407 (2022).

43. Cui, J. *et al.* Chirality selective magnon-phonon hybridization and magnon-induced chiral phonons in a layered zigzag antiferromagnet. *Nat. Commun.* **14**, 3396 (2023).

44. Barman, A., Mondal, S., Sahoo, S. & De, A. Magnetization dynamics of nanoscale magnetic materials: A perspective. *J. Appl. Phys.* **128**, 170901 (2020).

45. Li, Y. *et al.* Hybrid magnonics: Physics, circuits, and applications for coherent information processing. *J. Appl. Phys.* **128**, 130902 (2020).

46. Awschalom, D. D. *et al.* Quantum Engineering With Hybrid Magnonic Systems and Materials *(Invited Paper)*. *IEEE Trans. Quantum Eng.* **2**, 1–36 (2021).

47. Pirro, P., Vasyuchka, V. I., Serga, A. A. & Hillebrands, B. Advances in coherent magnonics. *Nat. Rev. Mater.* **6**, 1114–1135 (2021).

48. Yang, W.-G. & Schmidt, H. Acoustic control of magnetism toward energy-efficient applications. *Appl. Phys. Rev.* **8**, 021304 (2021).

49. Fallot, M. Ferromagnétisme des alliages de fer. *Ann. Phys.* **11**, 305–387 (1936).

50. Morrish, A. H. *The Physical Principles of Magnetism*. (IEEE Press, New York, 2001).

51. Landau, L. & Lifshits, E. On The theory of the dispersion of magnetic permeability in ferromagnetic bodies. *Phys Zeitsch Sow* **8**, 153 (1935).

52. Gilbert, T. L. A Lagrangian formulation of the gyromagnetic equation of the magnetic field. *Phys. Rev.* **4**, 1243 (1955).

53. Gurevich, A. G. & Melkov, G. A. *Magnetization Oscillations and Waves*. (CRC Press, 2020). doi:10.1201/9780138748487.

54. Markó, D. *et al.* Interpretation of Spin-Wave Modes in Co / Ag Nanodot Arrays Probed by Broadband Ferromagnetic Resonance. *Phys. Rev. Appl.* **20**, 024059 (2023).

55. Eason, K., Patricia Rouelli Garcia Sabino, M., Tran, M. & Fook Liew, Y. Origins of magnetic damping measurement variations using ferromagnetic resonance for nano-sized devices. *Appl. Phys. Lett.* **102**, 232405 (2013).

56. Landau, L. D. & Lifshitz, E. M. *Mechanics*. (Elsevier, Butterworth-Heinemann, Amsterdam Heidelberg, 1976).

57. Gowtham, P. G., Moriyama, T., Ralph, D. C. & Buhrman, R. A. Traveling surface spin-wave resonance spectroscopy using surface acoustic waves. *J. Appl. Phys.* **118**, 233910 (2015).

58. Bhuktare, S., Bose, A., Singh, H. & Tulapurkar, A. A. Gyrator Based on Magneto-elastic Coupling at a Ferromagnetic/Piezoelectric Interface. *Sci. Rep.* **7**, 840 (2017).

59. Camara, I. S., Duquesne, J.-Y., Lemaître, A., Gourdon, C. & Thevenard, L. Field-Free Magnetization Switching by an Acoustic Wave. *Phys. Rev. Appl.* **11**, 014045 (2019).

60. Puebla, J. *et al.* Acoustic ferromagnetic resonance and spin pumping induced by surface acoustic waves. *J. Phys. Appl. Phys.* **53**, 264002 (2020).

61. Zhao, C. *et al.* Phonon Transport Controlled by Ferromagnetic Resonance. *Phys. Rev. Appl.* **13**, 054032 (2020).

62. Küß, M. *et al.* Symmetry of the Magnetoelastic Interaction of Rayleigh and Shear Horizontal Magnetoacoustic Waves in Nickel Thin Films on Li Ta O 3. *Phys. Rev. Appl.* **15**, 034046 (2021).

63. Deger, C. *et al.* Sound velocity of AlxGa1−xN thin films obtained by surface acoustic-wave measurements. *Appl. Phys. Lett.* **72**, 2400–2402 (1998).

64. Weiss, P. L'hypothèse du champ moléculaire et la propriété ferromagnétique. *J. Phys. Théorique Appliquée* **6**, 661–690 (1907).

65. You, C.-Y. & Shin, S.-C. Derivation of simplified analytic formulae for magneto-optical Kerr effects. *Appl. Phys. Lett.* **69**, 1315–1317 (1996).

66. Koopmans, B. Laser-Induced Magnetization Dynamics. in *Spin Dynamics in Confined Magnetic Structures II* (eds. Hillebrands, B. & Ounadjela, K.) vol. 87 256–323 (Springer Berlin Heidelberg, Berlin, Heidelberg, 2003).

67. Hillebrands, B. & Ounadjela, K. *Spin Dynamics in Confined Magnetic Structures II*. (Springer, Berlin ; New York, 2003).

68. Malinowski, G., Kuiper, K. C., Lavrijsen, R., Swagten, H. J. M. & Koopmans, B. Magnetization dynamics and Gilbert damping in ultrathin Co48Fe32B20 films with out-of-plane anisotropy. *Appl. Phys. Lett.* **94**, 102501 (2009).

69. Kim, S. Ultrafast magneto-optical measurements for probing magnon–phonon interactions in nanomagnets. *Nat. Rev. Phys.* **4**, 288–288 (2022).

70. Lee, E. W. Magnetostriction. *Sci. Prog.* **41**, 161 (1953).

71. Néel, L. Anisotropie magnétique superficielle et surstructures d'orientation. *J. Phys. Radium* **15**, 225–239 (1954).

72. Lee, E. W. Magnetostriction and Magnetomechanical Effects. *Rep. Prog. Phys.* **18**, 184–229 (1955).

73. Bonin, R., Schneider, M. L., Silva, T. J. & Nibarger, J. P. Dependence of magnetization dynamics on magnetostriction in NiFe alloys. *J. Appl. Phys.* **98**, 123904 (2005).

74. Bozorth, R. M., Tilden, E. F. & Williams, A. J. Anisotropy and Magnetostriction of Some Ferrites. *Phys. Rev.* **99**, 1788–1798 (1955).

75. Hunter, D. *et al.* Giant magnetostriction in annealed Co1−xFex thin-films. *Nat. Commun.* **2**, 518 (2011).

76. Clark, A. E. *et al.* Extraordinary magnetoelasticity and lattice softening in bcc Fe-Ga alloys. *J. Appl. Phys.* **93**, 8621–8623 (2003).

77. Clark, A. E., Restorff, J. B., Wun-Fogle, M., Lograsso, T. A. & Schlagel, D. L. Magnetostrictive properties of body-centered cubic Fe-Ga and Fe-Ga-Al alloys. *IEEE Trans. Magn.* **36**, 3238–3240 (2000).

78. Clark, A. & Crowder, D. High temperature magnetostriction of TbFe2 and Tb27Dy73Fe2. *IEEE Trans. Magn.* **21**, 1945–1947 (1985).

79. Snodgrass, J. D. & McMasters, O. D. Optimized TERFENOL-D manufacturing processes. *J. Alloys Compd.* (1997).

80. Franco, V. The 15th Joint Magnetism and Magnetic Materials–Intermag Conference. *AIP Adv.* **12**, 060401 (2022).

81. Tiwari, S. *et al.* Coupling of Lamb Waves and Spin Waves in Multiferroic Heterostructures. *J. Microelectromechanical Syst.* **29**, 1121–1123 (2020).

82. Babu, N. K. P. *et al.* The Interaction between Surface Acoustic Waves and Spin Waves: The Role of Anisotropy and Spatial Profiles of the Modes. *Nano Lett.* **21**, 946–951 (2021).

83. Chang, C. L. *et al.* Driving Magnetization Dynamics in an On-Demand Magnonic Crystal via the Magnetoelastic Interactions. *Phys. Rev. Appl.* **10**, 064051 (2018).

84. Shelukhin, L. A. *et al.* Laser-Induced Magnetization Precession in Individual Magnetoelastic Domains of a Multiferroic Co 40 Fe 40 B 20 / Ba Ti O 3 Composite. *Phys. Rev. Appl.* **14**, 034061 (2020).

85. Yahagi, Y., Harteneck, B., Cabrini, S. & Schmidt, H. Controlling nanomagnet magnetization dynamics via magnetoelastic coupling. *Phys. Rev. B* **90**, 140405 (2014).

86. Yahagi, Y. Nanomagnet Dynamics with Magnetostatic and Magnetoelastic Interelement Coupling. *Univ. Calif. St. Cruz* (2015).

87. Xu, B., Shen, Z., Ni, X. & Lu, J. Numerical simulation of laser-generated ultrasound by the finite element method. *J. Appl. Phys.* **95**, 2116–2122 (2004).

88. Janušonis, J. *et al.* Ultrafast magnetoelastic probing of surface acoustic transients. *Phys. Rev. B* **94**, 024415 (2016).

89. Jaris, M. *et al.* Intrinsic spin dynamics in optically excited nanoscale magnetic tunnel junction arrays restored by dielectric coating. *Appl. Phys. Lett.* **109**, 202403 (2016).

90. Rana, B. & Otani, Y. Anisotropy of magnetic damping in Ta/CoFeB/MgO heterostructures. *Sci. Rep.* **13**, 8532 (2023).

91. Berk, C., Yahagi, Y., Dhuey, S., Cabrini, S. & Schmidt, H. Controlling the influence of elastic eigenmodes on nanomagnet dynamics through pattern geometry. *J. Magn. Magn. Mater.* **426**, 239–244 (2017).

92. Yang, W. G., Jaris, M., Hibbard-Lubow, D. L., Berk, C. & Schmidt, H. Magnetoelastic excitation of single nanomagnets for optical measurement of intrinsic Gilbert damping. *Phys. Rev. B* **97**, 224410 (2018).

93. Arias, R. & Mills, D. L. Extrinsic contributions to the ferromagnetic resonance response of ultrathin films. *Phys. Rev. B* **60**, 7395 (1999).

94. Beaujour, J.-M., Ravelosona, D., Tudosa, I., Fullerton, E. E. & Kent, A. D. Ferromagnetic resonance linewidth in ultrathin films with perpendicular magnetic anisotropy. *Phys. Rev. B* **80**, 180415 (2009).

95. Iihama, S. *et al.* Influence of L 1 0 order parameter on Gilbert damping constants for FePd thin films investigated by means of time-resolved magneto-optical Kerr effect. *Phys. Rev. B* **94**, 174425 (2016).

96. Lindner, J. *et al.* Two-magnon damping in thin films in case of canted magnetization: Theory versus experiment. *Phys. Rev. B* **80**, 224421 (2009).

97. Clerk, A. A., Lehnert, K. W., Bertet, P., Petta, J. R. & Nakamura, Y. Hybrid quantum systems with circuit quantum electrodynamics. *Nat. Phys.* **16**, 257–267 (2020).

98. Berk, C. *et al.* Strongly coupled magnon–phonon dynamics in a single nanomagnet. *Nat. Commun.* **10**, 2652 (2019).

99. Imamoğlu, A. Cavity QED Based on Collective Magnetic Dipole Coupling: Spin Ensembles as Hybrid Two-Level Systems. *Phys. Rev. Lett.* **102**, 083602 (2009).

100. Tabuchi, Y. *et al.* Hybridizing Ferromagnetic Magnons and Microwave Photons in the Quantum Limit. *Phys. Rev. Lett.* **113**, 083603 (2014).

101. Li, Y. *et al.* Coherent Coupling of Two Remote Magnonic Resonators Mediated by Superconducting Circuits. *Phys. Rev. Lett.* **128**, 047701 (2022).

102. Parkin, S. S. P. *et al.* Giant tunnelling magnetoresistance at room temperature with MgO (100) tunnel barriers. *Nat. Mater.* **3**, 862–867 (2004).

103. Yamamoto, M. *et al.* Fabrication of fully epitaxial magnetic tunnel junctions using cobalt-based full-Heusler alloy thin film and their tunnel magnetoresistance characteristics. *J. Phys. Appl. Phys.* **39**, 824–833 (2006).

104. Liu, Y. *et al.* Effect of annealing and applied bias on barrier shape in CoFe/MgO/CoFe tunnel junctions. *Phys. Rev. B* **83**, 165413 (2011).

105. Djayaprawira, D. D. *et al.* 230% room-temperature magnetoresistance in CoFeB⁄MgO⁄CoFeB magnetic tunnel junctions. *Appl. Phys. Lett.* **86**, 092502 (2005).

106. Nagamine, Y. *et al.* Ultralow resistance-area product of 0.4Ω(μm)2 and high magnetoresistance above 50% in CoFeB⁄MgO⁄CoFeB magnetic tunnel junctions. *Appl. Phys. Lett.* **89**, 162507 (2006).

107. Huang, J. C. A. *et al.* Effects of submonolayer Mg on CoFe–MgO–CoFe magnetic tunnel junctions. *J. Appl. Phys.* **104**, 073909 (2008).

108. Wang, W., Sukegawa, H., Shan, R., Mitani, S. & Inomata, K. Giant tunneling magnetoresistance up to 330% at room temperature in sputter deposited Co2FeAl/MgO/CoFe magnetic tunnel junctions. *Appl. Phys. Lett.* **95**, 182502 (2009).

109. Wang, W. *et al.* Coherent tunneling and giant tunneling magnetoresistance in Co 2 FeAl / MgO / CoFe magnetic tunneling junctions. *Phys. Rev. B* **81**, 140402 (2010).

110. Ikeda, S. *et al.* A perpendicular-anisotropy CoFeB–MgO magnetic tunnel junction. *Nat. Mater.* **9**, 721–724 (2010).

111. Zhang, J., Franz, C., Czerner, M. & Heiliger, C. Perpendicular magnetic anisotropy in CoFe/MgO/CoFe magnetic tunnel junctions by first-principles calculations. *Phys. Rev. B* **90**, 184409 (2014).

112. Wen, Z. *et al.* A 4-Fold-Symmetry Hexagonal Ruthenium for Magnetic Heterostructures Exhibiting Enhanced Perpendicular Magnetic Anisotropy and Tunnel Magnetoresistance. *Adv. Mater.* **26**, 6483–6490 (2014).

113. Chen, A. P., Burton, J. D., Tsymbal, E. Y., Feng, Y. P. & Chen, J. Effects of B and C doping on tunneling magnetoresistance in CoFe/MgO magnetic tunnel junctions. *Phys. Rev. B* **98**, 045129 (2018).

114. Galanakis, I. Surface properties of the half-and full-Heusler alloys. *J. Phys. Condens. Matter* **14**, 6329–6340 (2002).

115. Picozzi, S., Continenza, A. & Freeman, A. J. Co 2 Mn X (X = Si , Ge, Sn) Heusler compounds: An *ab initio* study of their structural, electronic, and magnetic properties at zero and elevated pressure. *Phys. Rev. B* **66**, 094421 (2002).

116. Wurmehl, S. *et al.* Electronic structure and spectroscopy of the quaternary Heusler alloy $Co_2 Cr_{1-x} Fe_x Al$. *J. Phys. Appl. Phys.* **39**, 803–815 (2006).

117. Galanakis, I. & Mavropoulos, P. Spin-polarization and electronic properties of half-metallic Heusler alloys calculated from first principles. *J. Phys. Condens. Matter* **19**, 315213 (2007).

118. Jourdan, M. *et al.* Direct observation of half-metallicity in the Heusler compound Co2MnSi. *Nat. Commun.* **5**, 3974 (2014).

119. Andrieu, S. *et al.* Direct evidence for minority spin gap in the C o 2 MnSi Heusler compound. *Phys. Rev. B* **93**, 094417 (2016).

120. Webster, P. J. MAGNETIC AND CHEMICAL ORDER IN HEUSLER ALLOYS CONTAINING COBALT AND MANGANESE.

121. Kübler, J., William, A. R. & Sommers, C. B. Formation and coupling of magnetic moments in Heusler alloys. *Phys. Rev. B* **28**, 1745–1755 (1983).

122. Şaşıoğlu, E., Sandratskii, L. M., Bruno, P. & Galanakis, I. Exchange interactions and temperature dependence of magnetization in half-metallic Heusler alloys. *Phys. Rev. B* **72**, 184415 (2005).

123. Tsunegi, S., Sakuraba, Y., Oogane, M., Takanashi, K. & Ando, Y. Large tunnel magnetoresistance in magnetic tunnel junctions using a Co2MnSi Heusler alloy electrode and a MgO barrier. *Appl. Phys. Lett.* **93**, 112506 (2008).

124. Tsunegi, S. *et al.* Enhancement in tunnel magnetoresistance effect by inserting CoFeB to the tunneling barrier interface in Co2MnSi/MgO/CoFe magnetic tunnel junctions. *Appl. Phys. Lett.* **94**, 252503 (2009).

125. Galanakis, I., Dederichs, P. H. & Papanikolaou, N. Slater-Pauling behavior and origin of the half-metallicity of the full-Heusler alloys. *Phys. Rev. B* **66**, 174429 (2002).

126. Sakuraba, Y. *et al.* Huge Spin-Polarization of L2 $_1$ -Ordered Co $_2$ MnSi Epitaxial Heusler Alloy Film. *Jpn. J. Appl. Phys.* **44**, L1100 (2005).

127. Kota, Y. & Sakuma, A. First-principles study for electronic structure and physical property of Co-based Heusler alloys. *J. Phys. Conf. Ser.* **266**, 012094 (2011).

128. Sakuraba, Y. *et al.* Giant tunneling magnetoresistance in Co2MnSi/Al–O/Co2MnSi magnetic tunnel junctions. *Appl. Phys. Lett.* **88**, 192508 (2006).

129. Bierhance, G. *et al.* Spin-voltage-driven efficient terahertz spin currents from the magnetic Weyl semimetals Co2MnGa and Co2MnAl. *Appl. Phys. Lett.* **120**, 082401 (2022).

130. Gupta, R. *et al.* Co $_2$ FeAl Full Heusler Compound Based Spintronic Terahertz Emitter. *Adv. Opt. Mater.* **9**, 2001987 (2021).

131. Tankhilevich, B. G. & Korenblit, Y. Novel spintronic device: terahertz magnon-photon laser. *J. Phys. Conf. Ser.* **263**, 012004 (2011).

132. Mizukami, S. *et al.* Low damping constant for Co2FeAl Heusler alloy films and its correlation with density of states. *J. Appl. Phys.* **105**, 07D306 (2009).

133. Bainsla, L. *et al.* Low magnetic damping for equiatomic CoFeMnSi Heusler alloy. *J. Phys. Appl. Phys.* **51**, 495001 (2018).

134. Guillemard, C. *et al.* Polycrystalline Co2Mn-based Heusler thin films with high spin polarization and low magnetic damping. *Appl. Phys. Lett.* **115**, 172401 (2019).

135. Peria, W. K. *et al.* Interplay of large two-magnon ferromagnetic resonance linewidths and low Gilbert damping in Heusler thin films. *Phys. Rev. B* **101**, 134430 (2020).

136. De Melo, C. *et al.* Unveiling transport properties of Co2MnSi Heusler epitaxial thin films with ultra-low magnetic damping. *Appl. Mater. Today* **25**, 101174 (2021).

137. Liu, Y. *et al.* Optically induced magnetization dynamics and variation of damping parameter in epitaxial Co 2 MnSi Heusler alloy films. *Phys. Rev. B* **81**, 094402 (2010).

138. Kim, S. *et al.* Magnetization dynamics of a CoFe/Co2MnSi magnetic bilayer structure. *J. Appl. Phys.* **133**, 093902 (2023).

139. Yang, W. G., Jaris, M., Hibbard-Lubow, D. L., Berk, C. & Schmidt, H. Magnetoelastic excitation of single nanomagnets for optical measurement of intrinsic Gilbert damping. *Phys. Rev. B* **97**, 224410 (2018).

140. Bayliss, P. Revised unit-cell dimensions, space group, and chemical formula of some metallic minerals. *Can. Mineral.* **28**, 751–755 (1990).

141. Rasing, T., Van Den Berg, H., Gerrits, T. & Hohlfeld, J. Ultrafast Magnetization and Switching Dynamics. in *Spin Dynamics in Confined Magnetic Structures II* (eds. Hillebrands, B. & Ounadjela, K.) vol. 87 216–255 (Springer Berlin Heidelberg, Berlin, Heidelberg, 2003).

142. Li, Y. *et al.* Giant Anisotropy of Gilbert Damping in Epitaxial CoFe Films. *Phys. Rev. Lett.* **122**, 117203 (2019).

143. Dubowik, J., Załęski, K., Głowiński, H. & Gościańska, I. Angular dependence of ferromagnetic resonance linewidth in thin films. *Phys. Rev. B* **84**, 184438 (2011).

144. Capua, A., Yang, S., Phung, T. & Parkin, S. S. P. Determination of intrinsic damping of perpendicularly magnetized ultrathin films from time-resolved precessional magnetization measurements. *Phys. Rev. B* **92**, 224402 (2015).

145. Zhuang, S. *et al.* Hybrid magnon-phonon cavity for large-amplitude terahertz spin-wave excitation. *Phys. Rev. Appl.* **21**, 044009 (2024).

146. Matsuo, M., Ieda, J. & Maekawa, S. Mechanical generation of spin current. *Front. Phys.* **3**, (2015).

147. Matsuo, M., Ieda, J., Harii, K., Saitoh, E. & Maekawa, S. Mechanical generation of spin current by spin-rotation coupling. *Phys. Rev. B* **87**, 180402 (2013).

148. Yu, T., Sharma, S., Blanter, Y. M. & Bauer, G. E. W. Surface dynamics of rough magnetic films. *Phys. Rev. B* **99**, 174402 (2019).

149. Zhao, X. *et al.* Soft fibers with magnetoelasticity for wearable electronics. *Nat. Commun.* **12**, 6755 (2021).

150. Schmidt, S. & Grimes, C. A. Characterization of nano-dimensional thin-®lm elastic moduli using magnetoelastic sensors. (2001).

151. Li, S., Orona, L., Li, Z. & Cheng, Z.-Y. Biosensor based on magnetostrictive microcantilever. *Appl. Phys. Lett.* **88**, 073507 (2006).

152. Grimes, C. A., Roy, S. C., Rani, S. & Cai, Q. Theory, Instrumentation and Applications of Magnetoelastic Resonance Sensors: A Review. *Sensors* **11**, 2809–2844 (2011).

153. Wang, J. *et al.* Detection of carcinoembryonic antigen using a magnetoelastic nano-biosensor amplified with DNA-templated silver nanoclusters. *Nanotechnology* **31**, 015501 (2020).

154. Narita, F. *et al.* A Review of Piezoelectric and Magnetostrictive Biosensor Materials for Detection of COVID-19 and Other Viruses. *Adv. Mater.* **33**, 2005448 (2021).

155. Gong, C. *et al.* Discovery of intrinsic ferromagnetism in two-dimensional van der Waals crystals. *Nature* **546**, 265–269 (2017).

156. Huang, B. *et al.* Layer-dependent ferromagnetism in a van der Waals crystal down to the monolayer limit. *Nature* **546**, 270–273 (2017).

157. Fei, Z. *et al.* Two-dimensional itinerant ferromagnetism in atomically thin Fe3GeTe2. *Nat. Mater.* **17**, 778–782 (2018).

158. Bae, Y. J. *et al.* Exciton-coupled coherent magnons in a 2D semiconductor. *Nature* **609**, 282–286 (2022).

159. Liu, S. *et al.* Direct Observation of Magnon-Phonon Strong Coupling in Two-Dimensional Antiferromagnet at High Magnetic Fields. *Phys. Rev. Lett.* **127**, 097401 (2021).

160. Luo, J. *et al.* Evidence for Topological Magnon–Phonon Hybridization in a 2D Antiferromagnet down to the Monolayer Limit. *Nano Lett.* **23**, 2023–2030 (2023).